Hierarchical Self-Assembly of Elongated Patchy Colloids into Photonic Crystals

Andreas Neophytou

Department of Chemistry

University of Birmingham

This dissertation is submitted for the degree of

Master of Science by Research

February 2019

Abstract

Photonic crystals, dubbed semiconductors for light, provide a platform to control the flow of light, increasingly finding applications in optical communications, lasers and sensors, just to name a few. This thesis presents a body of computational studies undertaken to design novel photonic crystals and devise a bottom-up route to realise them, exploiting a hierarchical self-assembly scheme for elongated triblock colloids. The designer colloidal particles under consideration have a soft repulsive spherocylindrical core, with an attractive patch on each of the hemispherical caps. Using basin-hopping global optimisation, we first predict the low-lying structures for these designer colloidal particles on the crystal energy landscape. We find four isoenergetic structures as the global minima: cubic tetrastack, hexagonal tetrastack, double cubic tetrastack and triple cubic tetrastack. Our photonic band structure calculations then reveal that the cubic and hexagonal tetrastack structures both possess photonic band gaps, which are wider than their spherical counterparts. Additionally, we argue that the local tetrahedral ordering of the particles is vital for the band gaps found for both of these crystal structures. Finally, we explore a hierarchical self-assembly strategy for the colloidal particles to realise these colloidal crystals via a bottom-up route. To this end, we introduce a hierarchy of interaction strengths for the patch-patch interactions so that a two-stage assembly process is followed via the formation of self-limiting tetrahedral clusters. Although such a staged assembly pathway successfully leads to a crystal, a mixed phase of cubic and hexagonal tetrastack structures is observed.

Acknowledgements

I should first offer a thanks to my parents, mainly for making me I guess, but also for never dissuading me from pursuing science (despite their complete lack of interest in it). Without them this thesis would not have been possible.

I read somewhere that a thesis is not a place to resolve grudges. Thankfully, my experiences from the past year have been nothing but pleasant and so I have none to speak of. This truth is mainly due to the contemporary residents of Office 204d in the Haworth Building: James Shaw, John Hey and Chris Avins. Also, it is impossible not to extend some form of thanks to Dr Daniel Morphew, whose legacy will live on forever in the Chakrabarti group I believe.

This section would be incomplete if I were not to thank Dr Dwaipayan Chakrabarti for his immense help (and patience) over this past year. After getting to know me I would like to think Dwaipayan would describe me as tenacious (although it's more likely he would describe me as obstinate). Additionally, I would like to thank Professor Roy Johnston for his insight and many helpful discussions. Over the course of this journey I ought to have benefited from interactions with very many learned people from time to time, but I would struggle to acknowledge every individual. So I extend my thanks to all of them collectively.

Finally, the intoductory chapter of this thesis greatly benefited from a first draft of a manuscript, of which I am a co-authour, to be published as a book chapter: Z. Ou, B. Luo, A. Neophytou, D. Chakrabarti and Q. Chen, "Synthesis and Self-Assembly of Janus and Triblock Patchy Particles", in *Self-Assembly of Nano- and Micro-Structured Materials Using Colloidal Engineering*, ed. D. Chakrabarti and S. Sacanna, Elsevier, 2019 (in press).

Contents

Introduction

In the winter of 1947 Walter H. Brattain and John A. Bardeen, under the guidance by William B. Shockley, all of whom at the time worked at Bell laboratories, discovered the transistor effect. Fast forward 70 years, and it is difficult to overstate the importance of this discovery to our everyday lives. It birthed a new wave of technologies, least of which being the integrated circuit and modern day computer. Thanks to these semiconductor devices, billion dollar companies like Apple, Microsoft, Samsung (and others of course) have emerged. Consumer demand has driven the semiconductor industry to miniaturise these electronic devices, whilst simultaneously improving their performance. However, semiconductor devices are now being pushed to their limits and we must turn to new technologies.

Enter photonic devices. There is a new demand for devices that use photons, rather than electrons, as information carriers, driving scientists and engineers to find new ways in which to control the optical properties of materials. Fibre-optic cables, which *simply* guide light, are one such material to emerge from this new endeavour and they have already completely revolutionised the telecommunications industry. In this thesis we concern ourselves with the fabrication of a new class of optical materials, called photonic crystals, that have a variety of potential applications.

1.1 Photonic Crystals

Photonic crystals are periodic structures, just like atomic or molecular crystals; however, we substitute the atoms or molecules for macroscopic media of different dielectric constants, ε. We will only consider photonic crystals composed of two different dielectric media, which form a one-, two- or three-dimensional (1D, 2D or 3D) periodic arrangement.

Maxwell's equations can be solved in order to extract the band structure of these materials, which gives all of the allowed frequencies, $\omega(\boldsymbol{k})$, for a photon with a given wave vector, $\boldsymbol{k}$. The interfaces between the different dielectric media act as scattering centres, and so, in certain instances, a photonic crystal may prevent the propagation of light in certain directions. The frequency range in which a photon is prohibited to propagate through the crystal is said to form a "photonic band gap" (PBG), and so, photonic crystals are also referred to as PBG materials.[1–3] The band structure for the multilayer film (a 1D photonic crystal) is shown in **Figure** 1.2, where we see that it has a band gap for light of normal incidence. **Figure** 1.2 also shows that the size of the band gap depends on the dielectric contrast of the constituent materials, with a larger contrast leading to a larger band gap. The calculation of the band structure, and the origin of the band structure, are elaborated on in SECTION 2.3. The multilayer film was studied by Lord Rayleigh in 1887, 100 years before the term "photonic crystal" had even been coined. He observed that, for normally incident light, the multilayer film acted as a perfect mirror for light with frequencies that, we now know, lie within its PBG.[4] It was not then for another 100 years before it was suggested that that this phenomenon could be extended for light propagating in all directions; with the modern ideas driving research into photonic crystals being attributed to the works of Yablonovich and John in 1987.[5,6] A photonic crystal which is periodic in 3D (or 2D) may be able to reflect light in any direction (or from any angle in a plane).

The size and location of the PBG is governed principally by the symmetry, volume fraction, topology of the crystal, as well as, the shape of the individual scatterers that form the crystal and their dielectric constant. The first photonic crystal with a complete 3D PBG was fabricated in 1991 by Yablonovich, a variant of the diamond structure was made by drilling holes in a block of dielectric material (the structure is now referred to as yablonovite).[7] The story behind the fabrication of this structure is almost poetic, as at the time Yablonovich was based at Bell laboratories, just as Brattain and Bardeen were. The fabrication of photonic crystals at optical length scales have several potential applications, for instance as waveguides in optical circuits[8], optical switches for telecommunications[9–11], chemical sensors,[12,13] and biosensors[14,15] to name a few. An attractive, and low cost, means of fabricating such photonic crystals is via the self-assembly of colloidal particles. However, so far only close-packed structures with narrow PBGs, that are not robust against defects, have been fabricated.

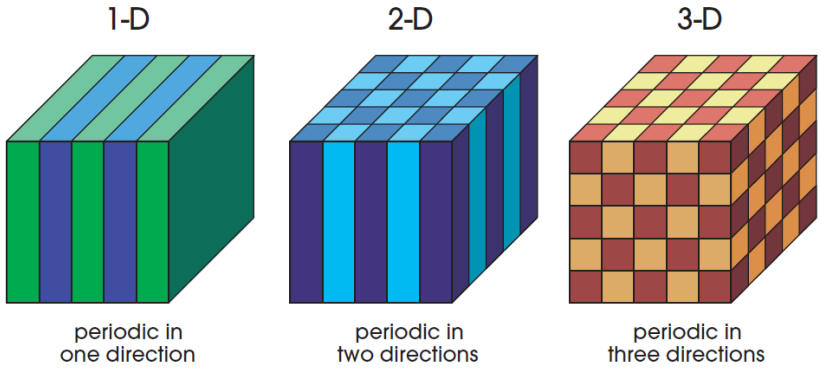

Figure 1.1: Representative images of 1D, 2D and 3D photonic crystals. Adapted from Ref. [16]

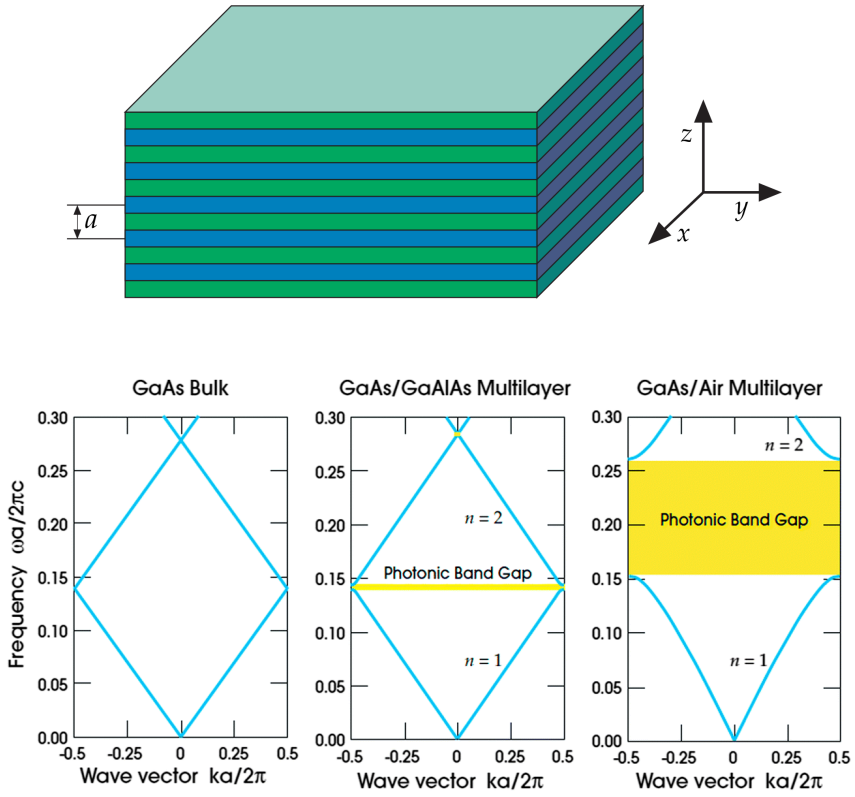

Figure 1.2: (**top**) The multilayer film, the different coloured layers represent different dielectric materials. Therefore, this structure has periodicity along the z-axis only. Each layer has a depth of $a/2$, where a is the spatial period of the structure. (**bottom**) The photonic band structures for three different multilayer film, where the incident wave is propagating along the z-axis. (**a**) The structure considered here is bulk GaAs ($\varepsilon = 13$), and so has no discrete translational symmetry. This is reflected by it having no band gap. (**b**) This multilayer film is composed of GaAs ($\varepsilon_1 = 13$) and GaAlAs ($\varepsilon_2 = 12$). The small difference in the dielectric constants of the different layers results in a narrow band gap. (**c**) This multilayer film is composed of GaAs ($\varepsilon_1 = 13$) and air ($\varepsilon_2 = 1$). The large difference in the dielectric constants of the different layers results in a wide band gap. The values $n = 1$ and $n = 2$ refer to the first and second bands of the band structure. Adapted from Ref. [16]

1.1.1 Diamond Family of Photonic Crystals

The fcc structure was initially considered to be the best candidate for a structure with a complete PBG.[1] However, it was later shown by Ho, Chan and Soukoulis to only have a partial PBG.[17] The first structure confirmed to possess a complete PBG was in fact diamond.[17] The structure was composed of dielectric spheres, with a refractive index of $n = 3.6$, positioned on diamond lattice points, and embedded in air. This structure was reported to have a band gap–midgap ratio (the ratio of the width of the band gap and the midgap frequency of the band gap) of 15%, although this value was later disputed and shown to actually only be 3.5%.[18] However, the inverse structure (i.e., diamond lattice of air spheres embedded in a high dielectric medium) was reported to have a band gap–midgap ratio of 29%, which still stands as one of widest band gaps reported.[17] The only structure to have a wider band gap is the so-called "rod-connected diamond" structure, which has a band gap–midgap ratio of 30%. This is a structure composed of dielectric spheres that lie on diamond lattice points, and are connected to their nearest neighbours by dielectric cylinders. A recent computational study looked to identify what structures provide optimal complete PBGs via topology optimisation, where each voxel of the unit cell was a degree of freedom. The rod-connected diamond structure was found to be the optimal structure with a band gap–midgap ratio of 30.2%.[19] Despite this, rod-connected diamond has proven difficult to fabricate. This has lead to a family of alternative photonic crystals, based on diamond, that are more easily fabricated. A thorough review of the diamond family of photonic crystals is provided in Ref. [20].

Complete PBGs are not limited to perfect crystals with long-ranged order. This is best demonstrated by the so-called "photonic amorphous diamond" (PAD) structure. PAD is an amorphous structure formed from tetrahedrally coordinated dielectric rods that was shown to possess a complete PBG of 18%. Despite having no long-range order, the structure still has a band gap.[21,22] However, PAD and rod-connected diamond have the same local tetrahedral ordering of dielectric cylinders. This has lead to the hypothesis that it is the local tetrahedral order which is the key to the opening of the band gap, rather than the long-ranged order which plays a secondary role.[22,23] A similar observation was made by Maldovan *et. al.* where they studied the existence of PBGs for structures in the 11 fcc spacegroups. They suggested that it is

the basic connectivity of the structure which determines the existence of a PBG, with additional structural complexity simply modifying the band gap.[24] Interestingly, a structure similar to PAD is observed in the feather barbs of the scarlet macaw.[25]

1.2 Colloidal Self-Assembly

The emergence of order from disorder is a common theme in nature – the formation of cell membranes from phospholipids, the crystallisation of water molecules into snowflakes and the intertwining of DNA strands into helices are just a few examples. The term "self-assembly" refers to the spontaneous formation of an ordered structure or pattern from its initially disordered components without any human intervention.[26] In particular, self-assembly provides a promising bottom-up route to 3D structures. However, understanding the physical principles, which govern the self-assembly of these building blocks, holds the key to "programming" particles to form target structures. Using molecular systems for such an end is not easily done, given they are not easily visualised and their interactions are often complex.

Colloids have emerged as a model system for atomic and molecular systems, where we define a colloidal dispersion as a system of small solid particles that are suspended in a solvent. Particles are considered to be colloidal if they have at least one dimension which is of the order 0.01 - 10 μm. This size range is not arbitrary, and the lower and upper limits have two key consequences. Compared to the particle size, the solvent molecules must be so small that the time scales of the solvent molecules and the colloidal particles are far enough apart that we can "integrate out" the degrees of freedom for the solvent molecules from our description of the system. Instead, we describe the solvent as a continuum. Therefore, the lower limit for the size of the colloidal particles is set by the size of the solvent molecules. The upper size limit is determined by the size at which external fields, such as gravity, overshadow the effects of Brownian motion. If one was to observe a dilute suspension of spherical colloidal particles, they would see that each particle moves with an irregular, but continuous, random motion. This motion is known as Brownian motion.[27,28] The phenomenon is named after Robert Brown, a botanist who first observed this motion while looking at plant pollen in 1827.[29] Albert Einstein, offered an explanation for this observation in 1905. He attributed the random motion to a constantly fluctuating net force on

the particles due to constant collisions with the solvent molecules.[30] In fact, it is because of this observation (and later experimental verification by Jean Baptiste Perrin[31]) that many were convinced of the existence of molecules. Due to this Brownian motion, colloidal systems have a "phase space" trajectory governed by the principles of statistical mechanics. As a result, a colloidal system will attempt to reach a thermodynamic equilibrium structure which minimises its free energy, hence why they are particularly useful as a model system for atomic and molecular systems.[27]

1.2.1 Colloidal Crystals

Due to their ability to reach thermal equilibrium, colloidal systems exhibit phase behaviour that is similar to that of atoms and molecules. If we consider a colloidal system composed of spherical particles that have purely isotropic and repulsive interactions, then as we increase the concentration of the particles we observe a transition, driven by entropy, from a liquid phase to a crystalline phase. In this crystalline phase the system attempts to maximise its packing fraction, and so the particles form a close-packed structure. There are two different close-packed structures with maximum packing fraction of 74%, the face-centred cubic (fcc, also known as the cubic close-packed structure) and hexagonal close-packed (hcp) structures. Both structures can be thought of as being built up from layers of spheres forming a triangular lattice, where the two structures arise due to differences in the stacking of these layers (this is discussed in more detail in SECTION 2.1.1). Experimentally it is observed that these close-packed colloidal crystals have randomly stacked layers, and are referred to as random hcp (rhcp) crystals.[32,33] This random phase arises as the difference in free-energy between the two structures is very small (fcc is reported to have the lower free-energy, although, this has been a topic of much controversy due to the difference being so small).[34,35]

The iridescence of the gemstone opal is actually due to the diffraction of light from a 3D grating composed of close-packed silica microspheres (i.e., it is a colloidal crystal). Close-packed colloidal crystals assembled in the laboratory are sometimes referred to as synthetic opals. An fcc lattice of close-packed colloidal spheres does not have a complete PBG; however, it does still have interesting optical properties that are also responsible for the iridescence of natural opals. The photonic band structure of these crystals have a narrow partial PBG (i.e., light

of a particular wavelength, or colour, is prohibited to propagate through the crystal when it is incident in a particular direction). The narrowness and directionality of these partial gaps leads to the iridescence of opal, and is an example of structural colour (i.e., colour that arises due to the scattering of light, rather than the absorption of light). Following the fabrication of a synthetic opal, it is possible to "invert" the structure by infiltrating the space between the spheres with a high dielectric material, for instance silicon. The colloidal spheres are then dissolved away, leaving behind an inverse opal. Whereas the "direct" fcc structure does not have a complete band gap, its inverse structure does. Similarly, the inverse hcp structure also has a complete PBG.[1,16,33] Other examples of structural colour found in nature include peacock feathers, jellyfish and butterfly wings. The blue iridescence of the *Morpho didus* butterfly is due to the diffraction of light from a 3D grating that forms a dielectric network.[36]

1.2.2 Patchy Particles and Molecular Colloids

Colloidal particles are not limited to assembling close-packed structures. In recent years, the availability of a rich arsenal of colloidal building blocks, thanks to advances in synthetic methods, has paved the way for an exotic variety of self-assembled structures. This makes colloidal particles especially attractive building blocks for 3D structures because of the scope for tuning the inter-particle interactions, in terms of the strength and range, as well as their shape largely also being tunable.[37–39] Given this, colloidal particles can be rationally designed so that they will self-assemble into a range of different structures. If we wish to move away from close-packed structures, and towards open structures, such as cubic diamond, the spherical symmetry of the particles must first be broken. In other words, we require particles with anisotropic interactions or geometry. It is possible to fabricate particles with anisotropic interactions that have a number of attractive or repulsive patches on their surface, that are often referred to as "patchy" particles.[40] The patches introduce directionality to the inter-particle interactions, meaning that altering the number, size, shape and relative geometry of the patches will also alter the potential structures that the particles can form. Additionally, we must also consider the strength of the inter-particle interactions, if they are too strong the particles will become kinetically trapped in disordered structures, whilst if they are too weak assembly will not occur.[41] The strength of the interactions must be correctly tuned so as to allow for bond reversibility, this ensures that

incorrectly positioned particles can be re-positioned. Colloidal particles with patches of DNA sticky ends on their surface have been fabricated. These particles display specific directional bonding, so that when they assemble into clusters they form "molecular colloids". The valency of the colloidal atoms, and hence what colloidal molecules they can form, is controlled by the number of patches on their surface and the size of the patches, **Figure** 1.3 shows a range of colloidal molecules that can form from a set of colloidal atoms. DNA hybridisation ensures that the interactions between the colloidal atoms are specific, and so adds another layer of control over the formation of these colloidal molecules.[42]

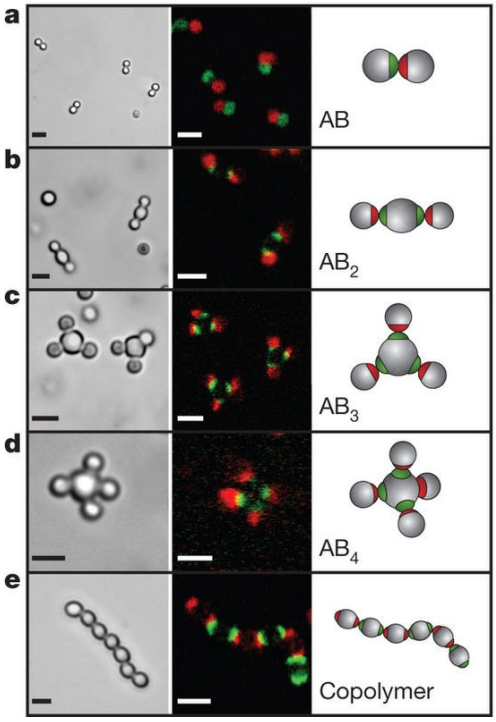

Figure 1.3: DNA coated colloids of various valancies that form "colloidal molecules", where the green and red patches are complementary to one another **left** Bright-field microscopy images **center** confocal fluorescent microscopy images **right** cartoon representations of the particles. (**a**) Monovalent particles form AB-type molecules. (**b**) Divalent particles form AB_2-type molecules. (**c**) Trivalent particles form AB_3-type molecules (**d**) Tetravalent particles form AB_4-type molecules (**e**) If complementary divalent particles are mixed, linear polymer chains form. Adapted form Ref. [42]

Particular effort has been spent on investigating the assembly of colloidal particles with four identical patches arranged with a tetrahedral geometry.[43–47] These particles are an obvious choice for potential precursors to cubic diamond, and so hold the promise of a self-assembling system with a large complete PBG. Glotzer *et. al.* studied the assembly of patchy particle with a hard core, and patches with a tetrahedral arrangement using Monte Carlo simulations. They observed that, for fast cooling rates, the diamond structure is not observed, instead only kinetically arrested, disordered structures are obtained. However, for slow cooling rates, cubic

diamond is formed in 55% of the runs. This was clear evidence for the potential of these particles as precursors for cubic diamond; however, only a single parameter set was investigated.[43] Despite their promise, these particles have not been routinely available to experimentalists until very recently. Sacanna *et. al.* recently proposed a new method of fabricating patchy colloids, they call colloidal fusion.[48]

1.2.3 Self-Assembly of Triblock Patchy Particles

Unlike tetrahedral patchy colloids, triblock patchy particles have routinely been fabricated in bulk by the glancing angle deposition (GLAD) method.[49] As a result, we choose to focus on this system in this thesis. In a notable experimental study, Chen et. al. demonstrated a remarkable example of self-assembly in a system of triblock colloidal particles with hydrophobic patches on their poles, separated by a charged middle band, into an open Kagome lattice.[50] In this study, the gradual addition of salt to the system increasingly screened the repulsive electrostatic interactions between the charged surfaces. This allows the short-ranged hydrophobic interactions to come into play and maximise the number of attractive contacts between the patches, while simultaneously minimising the repulsive contacts between their charged middle bands. The size of the patches determined the number of attractive contacts each particle can form, and hence governed the geometric arrangements of the particles. The particles were constrained in a quasi-two-dimensional system and the patches had an opening angle of 65°, meaning that only two contacts could be made per patch. Each hydrophobic contact was of the magnitude $10k_{\mathrm{B}}T$ (where k_{B} is the Boltzmann constant and T is temperature), ensuring that incorrectly aligned bonds could be corrected so that the system would not become kinetically trapped in a disordered configuration.[50] After this example of self-assembly was reported, the self-assembly of triblock particles was, and still is, studied extensively with computational methods, usually using the, so-called, extended patch models. These models make use of a group of potential energy functions and combine a repulsive interaction, which is often a hard-core repulsion, with a short-ranged attractive term having an orientation dependence. In these models, the patchy particles are treated as rigid bodies with M circular patches on their surface, the orientation of particle i is denoted by $\hat{\mathbf{u}}_i$, and the orientation of patch a on particle i is denoted by $\hat{\mathbf{u}}_a$. The distance between the centre of mass of particles i and j is given by $r_{ij} = \|\mathbf{r}_{ij}\| = \|\mathbf{r}_i - \mathbf{r}_j\|$.

Kern and Frenkel considered a simple model for spherical patchy particles to study the effect of the size and number of attractive patches on the fluid–fluid coexistence,[51] the Kern-Frenkel model, as it is now known, has been widely used in computational studies of patchy particles. The Kern-Frenkel model has a hard core, decorated with patches, and describes the directional patch-patch interactions in terms of a square-well potential with an angular modulation. A bond is considered to form between two particles i and j if their center-to-center separation r_{ij} is less than a certain distance and if two patches, each with a half angle of θ, on the interacting particles face each other.[51] The Kern-Frenkel potential takes the form:

$$U_{ij}^{\mathrm{kf}}(\mathbf{r}_{ij}, \hat{\mathbf{u}}_i, \hat{\mathbf{u}}_j) = \sum_{a=1}^{M} \sum_{b=1}^{M} U_{ab}^{\mathrm{sw}}(r_{ij}) \cdot f_{ab}(\hat{\mathbf{r}}_{ij}, \hat{\mathbf{u}}_a, \hat{\mathbf{u}}_b) \tag{1.1}$$

where M is the number of patches on each particle. The square-well potential is given by

$$U_{ij}^{\mathrm{sw}}(r_{ij}) = \begin{cases} \infty & \text{if } r_{ij} < \sigma \\ -\epsilon & \text{if } \sigma \leq r_{ij} < \sigma + \delta \\ 0 & \text{otherwise} \end{cases} \tag{1.2}$$

where σ is the hard-sphere diameter and δ is the range of the attractive interaction with the well depth ϵ. The angular dependence of the potential is given by

$$f_{ab}(\hat{\mathbf{r}}_{ij}, \hat{\mathbf{u}}_a, \hat{\mathbf{u}}_b) = \begin{cases} 1 \quad \text{if} \begin{cases} (\hat{\mathbf{r}}_{ij} \cdot \hat{\mathbf{u}}_a) > \cos\theta \text{ for some patch } a \text{ on i} \\ \text{and } (\hat{\mathbf{r}}_{ji} \cdot \hat{\mathbf{u}}_b) > \cos\theta \text{ for some patch } b \text{ on j} \end{cases} \\ 0 \quad \text{otherwise} \end{cases} \tag{1.3}$$

Most of the computational studies of triblock particles to date have employed the Kern-Frenkel model with two equal-size attractive patches on the poles.

1.2.3.1 Two-Dimensional Crystal Phases

The initial experimental work on the Kagome lattice led Romano and Sciortino to study the phase diagram of the two-patch Kern-Frenkel model in two-dimensions for two different values

of the patch width, both of which allow for a maximum of two bonds per patch with a maximum interaction range of 1.05σ.[52] The open Kagome lattice was shown to be stable at low pressures; as the pressure was increased, a close-packed hexagonal structure was observed instead, and at high temperatures a fluid phase was found to be stable. Each particle in the Kagome and hexagonal lattices have four bonding contacts, the particles in the hexagonal lattice also have an additional two non-bonding contacts.

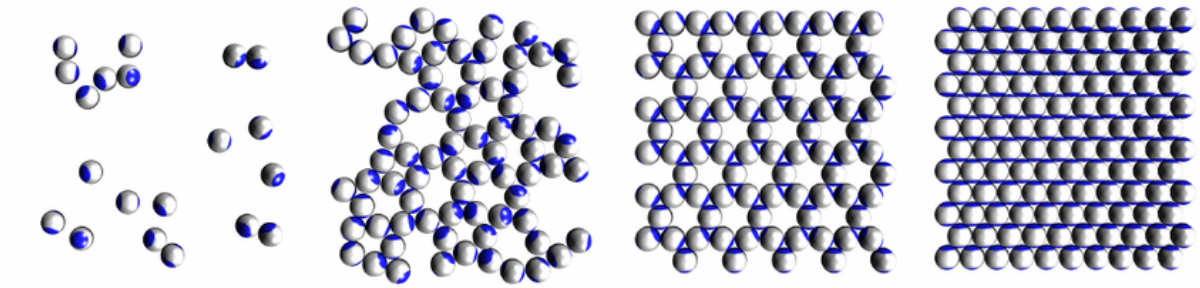

Figure 1.4: Snapshots of the gas, liquid, Kagome and hexagonal phases of the triblock particles. The particles are constrained to translate in two-dimensions, but are free to rotate in three-dimensions. Adapted from Ref. [53]

If particles are only able to interact with their nearest neighbors, as the triblock particles do, then for each interaction there will be a single constraint on the system. The average number of constraints in the Kagome and hexagonal structures is the coordination number of each particle (i.e. four and six respectively). According to Maxwell's counting rules, for a system to be considered mechanically stable it must have more than $2d$ constraints, where d is the dimensionality of the system. A system that has $2d$ constraints is called an isostatic system, such as the Kagome lattice.[54] This begs the question – *despite being mechanically unstable, why is the Kagome lattice observed as a stable structure in both experiment and simulation*?

Mao *et. al.* explained this stability using an analytical theory based on lattice dynamics.[55] In particular, the stability of the Kagome lattice was attributed to rotational and vibrational entropy. For the triblock particles there is a finite range of bond-angles between neighboring particles which are isoenergetic, with the number of orientational microstates being limited by patch size. This facilitates the existence of zero-energy distortions (*floppy modes*) within the Kagome lattice that corresponds to rotations of trianglular units along straight lines in the lattice. For isotropic spheres these floppy modes would result in the collapse of the Kagome

lattice into a close-packed hexagonal structure. However, due to the finite range of isoenergetic bond angles for triblock particles, the Kagome lattice gains additional constraints, leading to its mechanical stability. However, this does not explain why the Kagome lattice is observed rather than the hexagonal lattice, given that the structures are isoenergetic (if the particles exhibit hard-core repulsion) and possess the same rotational entropy per particle. The Kagome lattice is favored over its close-packed counterpart due to particles in the open structure having more room to vibrate, leading to its entropic selection. As stated earlier, particles in the hexagonal lattice have two additional non-bonding contacts compared to the Kagome lattice, as a result the particles are more confined in the close-packed lattice and so have less vibrational entropy. If the density is not too high, the rotational and vibrational entropy are the dominant factors in determining which structure is favoured. However, the close-packed structure, *of the same density* as the open structure, has greater translational entropy. If the pressure is increased, or the temperature decreased, translational entropy becomes more dominant resulting in the close-packed structure being entropically favoured.[56] Mao *et al.* also predicted that as the width of the patches increased (up to the maximum patch width for the two bond limit) the Kagome lattice becomes more stable, agreeing with the observations made by Romano and Sciortino.

Mao notes that the potential models considered so far do not completely capture the true nature of triblock particles.[57] However, in the experimental system where the Kagome lattice is observed[50] the salt concentration is high enough to screen the electrostatic repulsion down to the scale of surface roughness, justifying the use of the hard-core repulsion in these models. Nevertheless, if the potential was not flat with respect to particle orientations, and if the range of the repulsive interactions was to increase, the Kagome lattice would lie lower on the potential energy surface with respect to the hexagonal lattice. Given this, it likely that the Kagome lattice can be further stabilised over the hexagonal lattice if the range or strength of the repulsive interactions were to also be fine tuned. However, vibrational entropy is still likely to be the main driving force for the assembly of the Kagome lattice over the hexagonal lattice.[52,55–57]

1.2.3.2 Three-Dimensional Crystal Phases

In addition to the two-dimensional Kagome lattice, triblock particles with the "X" bonding geometry are also predicted to form three-dimensional open lattices[55,58,59], which are shown in

Figure 1.5. If the width of the patches is such that they are only able to form three bonds the triblock particles are predicted to form cubic and hexagonal tetrastack, where these open structures are made up of tetrahedra rather than triangular units. The two tetrastack structures are very closely related, with the only difference being how adjacent Kagome planes are stacked. The cubic tetrastack crystal is also well-known to have a complete PBG.[60–63] The tetrastack structures are also isostatic, and are stabilised by the same entropic effects discussed for the Kagome lattice.[58] If the patches are able to form four bonds then the triblock particles are able to form the open perovskite (P) structure, where the particles form a crystal composed of corner sharing octahedra.

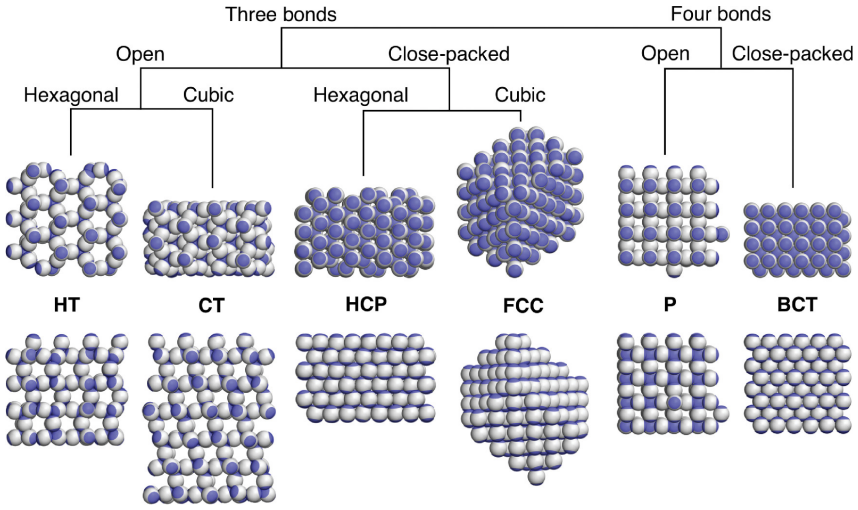

Figure 1.5: Equilibrium crystal phases of triblock particles that are considered in [59]. Top and bottom rows are different views of the same structures, rotated by 90° to show the three-dimensional arrangement of the particles. Adapted with permission from Ref. [59]. Copyright 2016 American Chemical Society.

In a computational study, Reinhart and Panagiotopoulos investigated the equilibrium crystal phases of the triblock particles with symmetric patches for various patch sizes and interaction ranges (δ), using the Kern-Frenkel model in three dimensions.[59] The authors combined Monte Carlo simulations with free energy calculations. The particles considered had a patch surface coverage, χ, between $\chi = 0.28$ and $\chi = 0.36$, where $\chi = 1 - \cos\theta$ (these correspond to opening angles in the range 44°-50°). These patch angle were chosen to ensure the particles could accommodate three or four bonds per patch. The interaction ranges were in the range $\delta \in [1.02, 1.10]$, comparable to the experimental conditions. The study focused on the six crystal

phases shown in **Figure** 1.5 and investigated their relative thermodynamic stabilities. The free energy difference between the two tetrastack lattices is negligible,[59,64] as is the case for the FCC and HCP lattices.[34,35] The CT lattice was found to be marginally favored over the HT lattice,[59] presumably due to the staggered configuration of the Kagome planes providing a slight increase in rotational entropy.[55] This difference, however, is dependent on the patch width. For a patch angle of 44° (and δ of 1.03) the difference is of the order $0.06k_{\mathrm{B}}T$, whereas it is $0.20k_{\mathrm{B}}T$ for a patch angle of 50° (and δ of 1.02).[59] This difference is still small, resulting unavoidably in stacking hybrids of the two tetrastack structures in the self-assembled crystals.[59,64] This suggests that the difference in free energy between the CT and HT lattices cannot be exploited to preferentially form either lattice.

Romano and Sciortino laid out one route to selectively assemble one of the tetrastack structures with their 'patterning symmetry' concept, which imposed geometric constraints on the patches in order to control the relative arrangements of the nearest neighbors of the two patches.[64] The CT lattice is comprised of corner-shared tetrahedra in such a way that each particle has six neighbors in a staggered configuration, whereas the HT lattice involves some eclipsed configurations in addtion to staggered configurations. Instead of circular patches, Romano and Sciortino considered two triangular patches on the poles oriented in a staggered configuration to destabilize the HT lattice, thus facilitating the self-assembly of the CT lattice.[64] If the two triangular patches were eclipsed, neither of the tetrastack crystals was observed as both require some staggered motifs, instead clathrate-like structures were observed. The geometric constraint arising from the lower symmetry of the particles with triangular patches gave rise to an entropic cost. As a result, the temperature at which nucleation occurred for the CT lattice was decreased.[64] Alternatively, the difference in interstitial void patterns between the two polymorphs can be exploited using 'structure-directing' agents (SDA).[65] The CT lattice has octahedral voids completely surrounded by tetrahedral voids, whereas the octahedral voids in the HT lattice share faces and stack in columns. Polymers can be used as SDAs to drive the formation of one polymorph over the other as the entropic cost of polymer confinement depends on how complementary the polymer's shape is relative to the voids in the crystal. A Monte Carlo and molecular dynamics study, where the particles have a soft-repulsive core, showed that by using star shaped polymers it is possible to bias the formation of HT over CT. This provides

another layer of control as the SDAs can be designed, along with the particles, to favour a single polymorph of the triblock particles, and can also be applied to favour either the FCC or HCP lattice. As the polymer density is increased depletion effects stabilize the close-packed structures. Given this, care must be taken so as not to destabilize the open crystals, causing them to collapse into a close-packed structure.[65]

1.2.3.3 Staged Assembly Strategies

In a very recent study that used a variety of computational techniques, Morphew *et. al.* realized a hierarchy of interactions strengths with triblock patchy particles to encode hierarchical self-assembly into colloidal crystals via colloidal clusters of uniform size and shape under temperature control.[66] The hierarchical self-assembly of these particles into cubic diamond and body-centered cubic crystals was demonstrated via distinct clusters, namely, tetrahedra and octahedra, respectively, as shown in **Figure** 1.6. The triblock particles these authors considered have asymmetric patch sizes such as those synthesised by Chen *et. al.*, who observed a distribution of cluster sizes following the first stage of assembly when they triggered stage-wise assembly by varying the ionic strength of the medium in steps.[67] The computational study by Morphew *et. al.* used designer triblock patchy particles, with wider patches forming stronger bonds than the narrower ones, and fine tuned the patch sizes to ensure that the first stage of assembly yields uniform clusters.[66]The potential used in this study has some similarity with the Kern-Frenkel model in its description of the patch-patch interaction. However, the isotropic part of the potential is given by a Yukawa potential without a hard core, describing screened electrostatic interactions and the anisotropic patch-patch interaction dies out smoothly instead of a square-well potential with angular modulation. In this study, the size of the wider patch and the range of the patch-patch interactions proved to be critical in determining which clusters are formed in the first stage of assembly, and thus the morphology of the clusters formed. The size of the narrower patch B was so chosen that it formed only one bond per patch. The formation of self-limiting clusters in the first stage of assembly was crucial for the secondary building blocks for the next stage of assembly to be monodisperse, and thus for hierarchical self-assembly into crystals. The second stage of assembly was driven by patch B-patch B interactions, which were strong enough to drive the assembly but weak enough for negotiating the kinetic traps.[66]

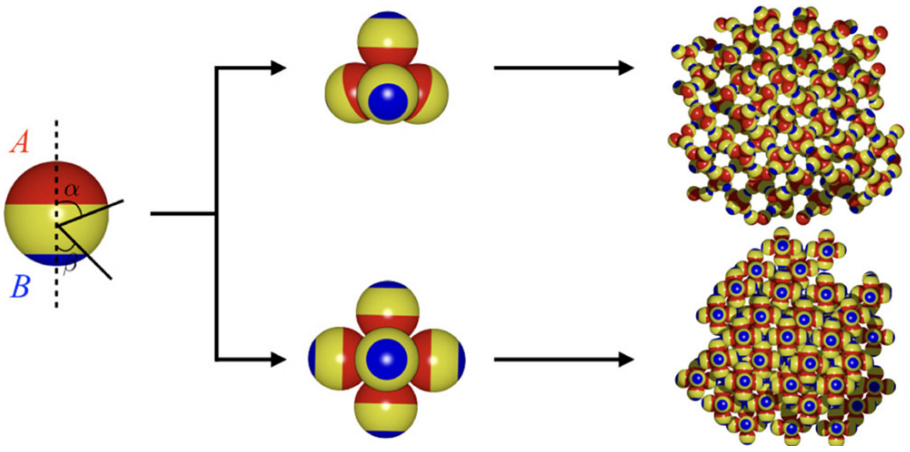

Figure 1.6: Overview of the staged assembly process for triblock patchy colloids with a hierarchy of interaction strengths, leading to distinct colloidal crystals. The patch A-patch A interactions are stronger than those of patch B-patch B interactions. Depending upon the size of patch A, and the range over which the particles interact, a cubic diamond diamond crystal or body-centered cubic crystal can be formed via tetrahedra or octahedra, respectively. Adapted from Ref. [66]

1.2.4 Patchy Particles with Anisotropic Shape

So far we have limited our discussion to that of spherical triblock particles, where the formation of open structures is controlled solely by the anisotropic interactions. However, geometric anisotropy can also be exploited to provide another layer of control over the structures formed. The Kagome lattice is only formed with spherical triblock particles if they are constrained to act as a quasi-two-dimensional system. Wales and Fejer performed a numerical study on clusters of triblock particles that aimed to form a structure made up of Kagome motifs, without imposing geometric constraints on the system. The building block they considered was constructed using two rigidly linked concentric ellipsoids, **Figure** 1.7(a), that (as the authors say) resembles a 'flying saucer'. The yellow oblate ellipsoid (A) is purely repulsive and has an aspect ratio such that only part of its surface is exposed, ellipsoid B is actually an attractive isotropic sphere. The particles interact via the Paramonov-Yaliraki (PY) potential, with each ellipsoid interacting with both ellipsoids of other particles.

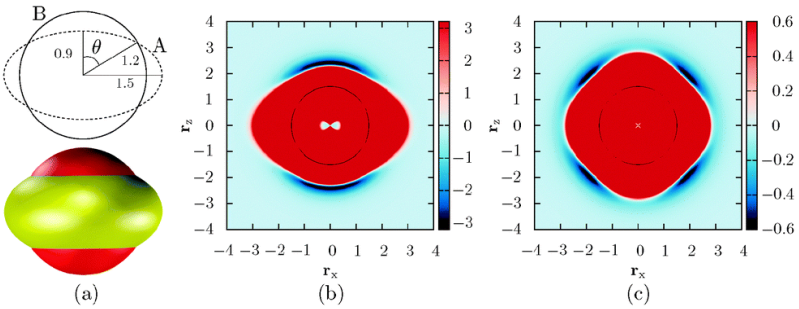

Figure 1.7: **a**. Schematic and space-filling representation of the 'flying saucer'triblock particles. The dashed circle represents the repulsive yellow ellipsoid, and the solid line represents the isotropic sphere. **b**. Equipotential surface of two parallel particles in the xz plane. **c**. Equipotential surface of two perpendicular particles in the xz plane. Adapted from Ref. [68]

Due to the repulsive nature of ellipsoid A, the strongest interaction between two particles occurs when they point along their poles. The attractive well around the poles is wide however enough to accommodate rotational moves that correspond to floppy modes. Global minima for cluster sizes of $N \in [2, 31]$ were characterised, as were two larger clusters of 72 and 100. The geometry of the particles was designed such that the particles are able to form at most three bonds per patch. However, due to the geometric anisotropy of the particles there was competition between tetrahedra and the planar triangular configuration, with two bonds per patch. This results in global minima with tetrahedra for certain cluster sizes and the Kagome motif for others.

The Kagome motif was observed at 'magic number' minima of $N = 12$, 19, 24 and 29, and at $N = 72$. However at $N = 100$ the global minimum becomes a hollow structure. If gravity effects are considered, accounting for sedimentation forces, the hollow structure is disfavoured and the Kagome lattice becomes the global minimum. This study highlights how introducing geometric anisotropy to the triblock particles can be used to further control their assembly, whilst also showing how important sedimentation effects are to forming the Kagome lattice.[68]

Chaudhary *et al.* synthesized colloidal silica rods with gold coated tips, thus combining shape anisotropy with chemical heterogeneity in what they called "Janus matchsticks".[69] These Janus matchsticks, when suspended in water, formed multipod clusters of different sizes depending on the patch angle (α). Here, the patch angle, which was estimated to assume the geometry of a spherical cap, was again the critical factor in determining the coordination number for each particle. The structures observed resulted from a competition between sedimentation

effects (which favors planar geometries, as observed by Wales and Fejer) and free energy. A distribution of clusters was observed, with the dominant structures being the planar bipods and tripods. However, despite the sedimentation effects driving the formation of planar structures, tetrahedral structures were observed for tetrapods, conjectured by the authors to be due to rotational entropy.[69]

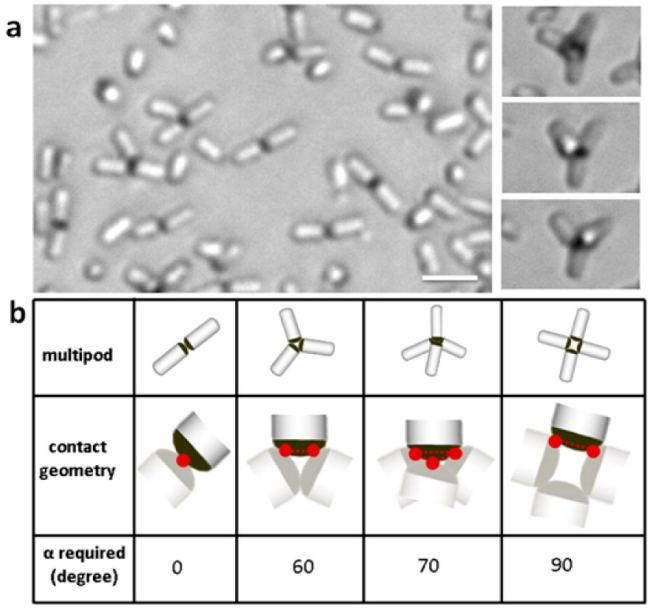

Figure 1.8: Janus matchstick self-assembly in aqueous solution (4.4 mM NaCl). **a**. Optical images of bipods and tripods coexisting with tetrapods. The right panel shows a time-resolved series of optical images of a tetrahedral cluster as it rotates by Brownian motion. **b**. Schematic table showing the minimum patch angle required for each multipod configuration. Adapted with permission from Ref. [69]. Copyright 2012 American Chemical Society.

The structures formed by Janus matchsticks were modeled by one-patch spherocylinders with the patch angle $\alpha \in \{60°, 120°\}$, were investigated in a computational study, using the Monte Carlo method.[70] While the spherocylinders were treated to have hard cores, the Kern-Frenkel model was adapted to describe the patch-patch interactions. For strong patch-patch interactions, bipods were predominately observed with some tripods for the smaller patch angle; as would be expected both tripods and tetrapods were dominant for the larger patch angle.[70]

1.3 Thesis Outline

It is apparent from the literature survey that colloidal open crystals are attractive for photonic crystals at optical frequencies.[17,20,33,60,71] The diamond and tetrastack crystals composed of dielectric spheres are well known to have a complete PBG.[17,60] The so-called rod-connected diamond structure is currently the champion structure for photonic crystals having the largest complete PBG, though it has been proved elusive to fabricate at the optical scale.[71] Patchy colloidal particles are promising building blocks to realise colloidal open crystals via self-assembly, thus providing a bottom-up fabrication route. The aim of the present body of work was to explore a bottom-up route to certain colloidal open crystals, which are elongated analogues of tetrastack crystals, and investigate their photonic properties. To this end, we employed a variety of computational techniques to predict crystal structures for designer elongated triblock patchy colloidal particles, calculated the photonic properties of those crystals and finally explored a hierarchical self-assembly strategy to realise those periodic structures that we identified to have applications as photonic crystals. The rest of this thesis is organised as follows. Chapter 2 outlines the necessary theoretical background for this thesis, namely the techniques associated with crystal structure prediction and photonic band structure calculations. The model for the elongated triblock patchy particles considered here and the results obtained are presented in Chapter 3, along with discussions. Chapter 4 concludes with a summary and outlook.

Theoretical Background

2.1 Formal Description of Crystal Structures

The characteristic feature of crystals is the periodic arrangement of their constituent particles, with the underlying periodicity being defined by a lattice. A lattice is an infinite array of points in a regular, periodic pattern that appears exactly the same regardless of where the array is viewed. We can define a three-dimensional (3D) lattice formally using a set of linearly independent vectors $\{\hat{\mathbf{a}}_i\}$, with $i \in \{1, 2, 3\}$, which define a unit cell. The unit cell is a finite region of space that when translated by all lattice vectors can fill all of space without gaps or overlaps (i.e., it tiles the space). Any point, $\mathbf{R}$, in the lattice can be written as:

$$\mathbf{R} \;=\; \hat{\mathbf{A}} \cdot \mathbf{n} \;=\; \sum_{i=1}^{3} n_i \hat{\mathbf{a}}_i, \qquad n_i \in \mathbb{Z} \tag{2.1}$$

where $\hat{\mathbf{A}}$ is known as the *cell matrix*, whose columns are the set of vectors $\{\hat{\mathbf{a}}_i\}$ called the *primitive lattice vectors*, (the "hat" notation is used to denote the primitive lattice). The three primitive lattice vectors are also defined in such a way that they share a common origin, and the complete lattice is then formed by taking every possible linear combination of the primitive lattice vectors. The smallest possible unit cell is known as the *primitive unit cell*, and contains *exactly one* lattice point. The volume, Ω, of the unit cell is given by the triple product:

$$\Omega \;=\; \hat{\mathbf{a}}_1 \cdot (\hat{\mathbf{a}}_2 \times \hat{\mathbf{a}}_3) \;=\; \hat{\mathbf{a}}_2 \cdot (\hat{\mathbf{a}}_3 \times \hat{\mathbf{a}}_1) \;=\; \hat{\mathbf{a}}_3 \cdot (\hat{\mathbf{a}}_1 \times \hat{\mathbf{a}}_2) \tag{2.2}$$

We can define a special primitive unit cell, the *Wigner-Seitz cell*, that has a lattice point at its center and possesses the same symmetry as the lattice (it can be thought of as a Voronoi cell).[72,73]

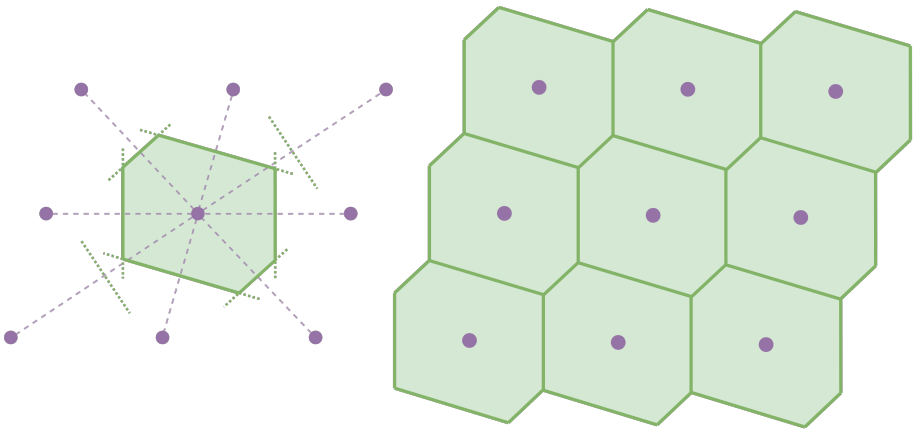

Figure 2.1: Construction of the Wigner-Seitz cell for a two dimensional lattice, and a segment of the infinite lattice that is produced by tessellating it.

Wigner-Seitz cells often have complicated shapes and so, usually, it is more convenient to work with a parallelepiped that has the same symmetry as the lattice but is not restricted to contain a single lattice point, known as the *conventional unit cell*. The non-primitive lattice vectors (or crystal axes) of the conventional unit cell are denoted by $\{\mathbf{a}_i\}$, and the angles between these vectors are $\{\alpha,\ \beta,\ \gamma\}$, together they are known as the lattice parameters. It is useful to formulate a general description of the unit cell in terms of the lattice parameters, $\mathbf{p}$, for when the cell vectors are non-orthogonal and have different lengths. In order to arrive at such a general description we must first outline a general set of conventions to adhere to:[74]

1. We align $\mathbf{a}_1$ with the x-axis so that: $\mathbf{a}_1 = (\mathrm{a}_1,\ 0,\ 0)$.
2. $\mathbf{a}_2$ is set to lie in the x-y plane, having a positive y-axis component, from basic trigonometry we then extract: $\mathbf{a}_2 = (\mathrm{a}_2\cos(\gamma),\ \mathrm{a}_2\sin(\gamma),\ 0)$.
3. Finally $\mathbf{a}_3$ is chosen to simply have a positive z-axis component.

We can then define a general cell matrix, $\mathbf{A}$, for any unit cell:

$$\mathbf{A} = \begin{bmatrix} \mathrm{a}_1 & \mathrm{a}_2\cos(\gamma) & \mathrm{a}_3\cos(\beta) \\ 0 & \mathrm{a}_2\sin(\gamma) & \mathrm{a}_3\left(\frac{\cos(\alpha)-\cos(\beta)\cos(\gamma)}{\sin(\gamma)}\right) \\ 0 & 0 & \frac{\mathrm{a}_3\sqrt{W}}{\sin(\gamma)} \end{bmatrix} \tag{2.3}$$

where, $W = 1 - \sum\cos^2(j) + 2\prod\cos(j), \qquad j = \{\alpha, \beta, \gamma\}$

A crystal structure is constructed through a combination of a crystal lattice, $\mathbf{R}$ and a *motif*. The motif is a set of i points, $\{\mathbf{z}_i\}$, that define the relative positions of the particles within each unit cell. We can then define the crystal structure as the set of particles with positions, $\{\mathbf{z}_i^{[\mathbf{n}]}\}$, given by: $\mathbf{z}_i^{[\mathbf{n}]} = \mathbf{z}_i + \mathbf{R}$. It is usually more convenient to express the positions of particles in the unit cell as fractions of the unit cell parameters, these are known as *fractional coordinates*. The conversion from Cartesian coordinates to fractional coordinates, $\mathbf{f}=(u,\ v,\ w)$, is done using the inverse of the cell matrix, $\mathbf{A}^{-1}$:

$$\begin{bmatrix} u \\ v \\ w \end{bmatrix} = \begin{bmatrix} \frac{1}{\mathrm{a}_1} & -\frac{\cos(\gamma)}{\mathrm{a}_1 \sin(\gamma)} & \mathrm{a}_1\left(\frac{\cos(\alpha)\cos(\gamma)-\cos(\beta)}{\sqrt{W}\sin(\gamma)}\right) \\ 0 & \frac{1}{\mathrm{a}_2 \sin(\gamma)} & \mathrm{a}_2\left(\frac{\cos(\beta)\cos(\gamma)-\cos(\alpha)}{\sqrt{W}\sin(\gamma)}\right) \\ 0 & 0 & \frac{\sin(\gamma)}{\mathrm{a}_3\sqrt{W}} \end{bmatrix} \begin{bmatrix} x \\ y \\ z \end{bmatrix} \tag{2.4}$$

The positions of the particles in the central unit cell can then be defined as:

$$\mathbf{z}_i = u_i\mathbf{a}_1 + v_i\mathbf{a}_2 + w_i\mathbf{a}_3 \tag{2.5}$$

And then convert back and forth between fractional and Cartesian coordinates using:

$$\mathbf{z}_i = \mathbf{A} \cdot \mathbf{f}_i \tag{2.6}$$

2.1.1 Cubic and Hexagonal Crystal Structures

Much of the focus of this thesis revolves around the differences between cubic and hexagonal polymorphs of open colloidal crystals. Here we briefly introduce the relevant cubic and hexagonal crystal structures.

2.1.1.1 Close-Packed Structures

There are two structures synonymous with the packing of identical spheres, such that the packing fraction (the total volume occupied by the spheres) is maximised: the *cubic close-packed* (ccp) and the *hexagonal close-packed* (hcp) structures. Both structures can be thought of as being

built up from layers of spheres forming a triangular lattice. One layer, B, can be placed on top of another layer, A, such that each sphere of B is in contact with three spheres of A. Finally a third layer, C, can be added so that the spheres cover the holes of the first layer that are unoccupied by the B, giving the ccp structure; or so that the spheres are directly above the spheres in A, giving the hcp structure.

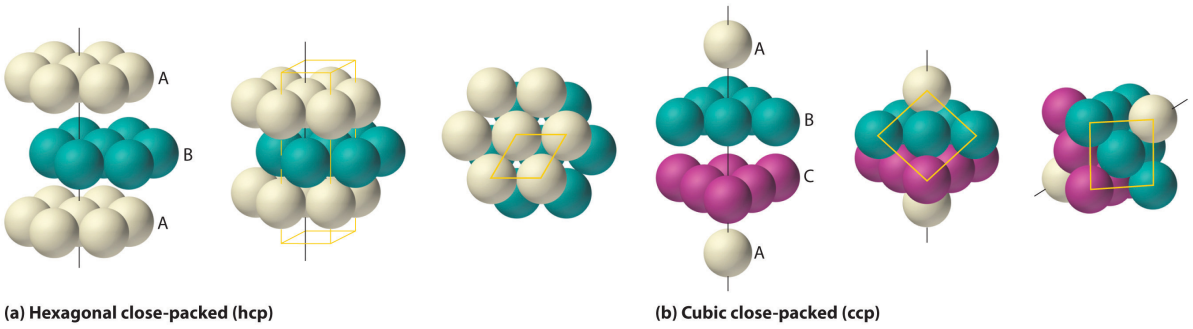

Figure 2.2: **(a)** The ABAB stacking of the hexagonal layers in the hcp structure are shown in an exploded view. The hexagonal unit cell is shown by the yellow lines, and the black line shows the C_6 symmetry axis of the structure. **(b)** The ABCABC stacking of the hexagonal layers in the ccp structure are shown in an exploded view. The cubic unit cell is shown by the yellow lines, and the black line shows one of the four C_3 axes. Adapted from Ref. [75]

Particles in the ccp structure all lie on an fcc lattice point (hence this structure is also known as the fcc structure). Therefore, the ccp structure can be described using an fcc primitive unit cell and a one particle motif:[72]

$$\hat{\mathbf{a}}_1 = \frac{a_1}{2}\left(\hat{\mathbf{y}} + \hat{\mathbf{z}}\right), \qquad \hat{\mathbf{a}}_2 = \frac{a_1}{2}\left(\hat{\mathbf{x}} + \hat{\mathbf{z}}\right), \qquad \hat{\mathbf{a}}_3 = \frac{a_1}{2}\left(\hat{\mathbf{x}} + \hat{\mathbf{y}}\right) \tag{2.7}$$

where, a is the length of the edge of the cube. The motif is then given by: $\mathbf{z}_0 = \mathbf{0}$.
The hcp structure, however, has a hexagonal unit cell:

$$\mathbf{a}_1 = a_1\hat{\mathbf{x}}, \qquad \mathbf{a}_2 = -\frac{a_1}{2}\hat{\mathbf{x}} + \frac{\sqrt{3}a_1}{2}\hat{\mathbf{y}}, \qquad \mathbf{a}_3 = a_1\hat{\mathbf{z}} \tag{2.8}$$

where, a and c are the hcp lattice constants. The two particle motif is given by:[72]

$$\mathbf{z}_0 = \mathbf{0}, \qquad \mathbf{z}_1 = \frac{2\mathbf{a}_1}{3} + \frac{\mathbf{a}_2}{3} + \frac{\mathbf{a}_3}{2} \tag{2.9}$$

2.1.1.2 Diamond Structures

Given its functional, and superficial, applications diamond is perhaps the most famous crystal structure. The structure usually referred to simply as 'diamond' is actually the cubic polymorph of diamond, that can be constructed from an fcc lattice, Eqn. (2.7), and a two particle motif:

$$\mathbf{z}_0 = \mathbf{0}, \qquad \mathbf{z}_1 = \frac{1}{4}(\hat{\mathbf{a}}_1 + \hat{\mathbf{a}}_2 + \hat{\mathbf{a}}_3) \tag{2.10}$$

An important variation of the cubic diamond structure is the *zincblende* structure adopted by semi-conductor alloys such as GaAs. The zincblende structure is exactly the same as the cubic diamond structure, however, the particles at the $\mathbf{z}_0$ and $\mathbf{z}_1$ sites are no longer identical. The point group of zincblende is T_d, whereas the point group of the cubic diamond structure is O_h. The T_d point group can be considered as a sub-group of O_h, and it can be shown that: $O_h \equiv T_d \times \{E, i\}$. If we take the midpoint between the $\mathbf{z}_0$ and $\mathbf{z}_1$ sites as an origin, we find that the cubic diamond structure is invariant under inversion with respect to this origin, however the zincblende structure is not. Therefore, the point group of cubic diamond contains the same point symmetry operations as the point group of zincblende, plus those of T_d followed by i. If we also consider translational symmetry operations we get the space group of the cubic diamond and zincblende structures to be $Fd\text{-}3m$ and $F\bar{4}3m$ respectively.

In addition to the cubic diamond structure there is also a hexagonal diamond polymorph (also known as Lonsdaleite) that can be constructed from a hexagonal unit cell, Eqn. (2.8), and a four particle motif:[76]

$$\begin{aligned} \mathbf{z}_0 &= \frac{\mathbf{a}_1}{3} + \frac{2\mathbf{a}_2}{3}, & \mathbf{z}_1 &= \frac{2\mathbf{a}_1}{3} + \frac{\mathbf{a}_2}{3} + \frac{\mathbf{a}_3}{2}, \\ \mathbf{z}_2 &= \frac{\mathbf{a}_1}{3} + \frac{2\mathbf{a}_2}{3} + \frac{3\mathbf{a}_3}{8}, & \mathbf{z}_3 &= \frac{2\mathbf{a}_1}{3} + \frac{\mathbf{a}_2}{3} + \frac{7\mathbf{a}_3}{8} \end{aligned} \tag{2.11}$$

The zincblende analogue for Lonsdaleite is known as *wurtzite*, where the particles located at the $\mathbf{z}_0$ and $\mathbf{z}_1$ sites are different to those at $\mathbf{z}_2$ and $\mathbf{z}_3$. The point group of wurtzite is $C_{6\mathrm{v}}$ and its spacegroup is $P6_3mc$. Lonsdaleite, however, has the $P6_3/mmc$ spacegroup and point group $D_{6\mathrm{h}}$, which can be written as $D_{6\mathrm{h}} \equiv C_{6\mathrm{v}} \times \{E, i\}$.[77]

2.1.1.3 Tetrastack Structures

The final set of structures we are interested in are the *tetrastack* structures. Each particle in these structures is connected to six others, and can be thought of as being built up from corner sharing tetrahedra, see **Figure** 2.3. The centres of these tetrahedra form the corresponding diamond structure. In the cubic polymorph all of tetrahedra are staggered relative to one another, as is the case in hexagonal tetrastack, except for the tetrahedra aligned with the c-axis of the hexagonal unit cell.

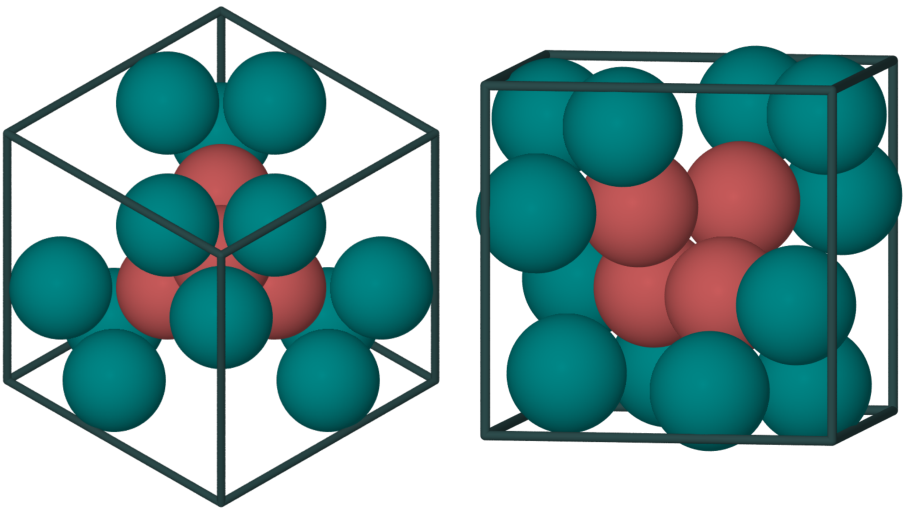

Figure 2.3: The conventional unit cell of the cubic tetrastack structure containing 16 particles that are all tetrahedrally coordinated. The central spheres are coloured pink in order to highlight the corner shared tetrahedron that emerges from the association of the four tetrahedra.

Like cubic diamond, cubic tetrastack can be constructed from a primitive fcc lattice, but with a four particle motif:

$$\begin{aligned} \mathbf{z}_0 &= \frac{5\hat{\mathbf{a}}_1}{8} + \frac{\hat{\mathbf{a}}_2}{8} + \frac{\hat{\mathbf{a}}_3}{8}, & \mathbf{z}_1 &= \frac{\hat{\mathbf{a}}_1}{8} + \frac{\hat{\mathbf{a}}_2}{8} + \frac{5\hat{\mathbf{a}}_3}{8}, \\ \mathbf{z}_2 &= \frac{\hat{\mathbf{a}}_1}{8} + \frac{\hat{\mathbf{a}}_2}{8} + \frac{\hat{\mathbf{a}}_3}{8}, & \mathbf{z}_3 &= \frac{\hat{\mathbf{a}}_1}{8} + \frac{5\hat{\mathbf{a}}_2}{8} + \frac{\hat{\mathbf{a}}_3}{8} \end{aligned} \tag{2.12}$$

It may not be immediately obvious looking at the conventional unit cell of cubic tetrastack, however, the structure can be considered as three-dimensional analogues of the 2D Kagome structure. This is much clearer when considering the conventional unit cell of hexagonal tetrastack, **Figure**

2.4, where a ring from the Kagome lattice is clearly visible along the [001] direction. For each hexagonal ring of the Kagome planes in the tetrastack structures, there are three particles that act as spacers between the planes. If all of the planes eclipse one another, then we arrive at the hexagonal polymorph. However, if the planes are all staggered relative to one another then we get cubic tetrastack.

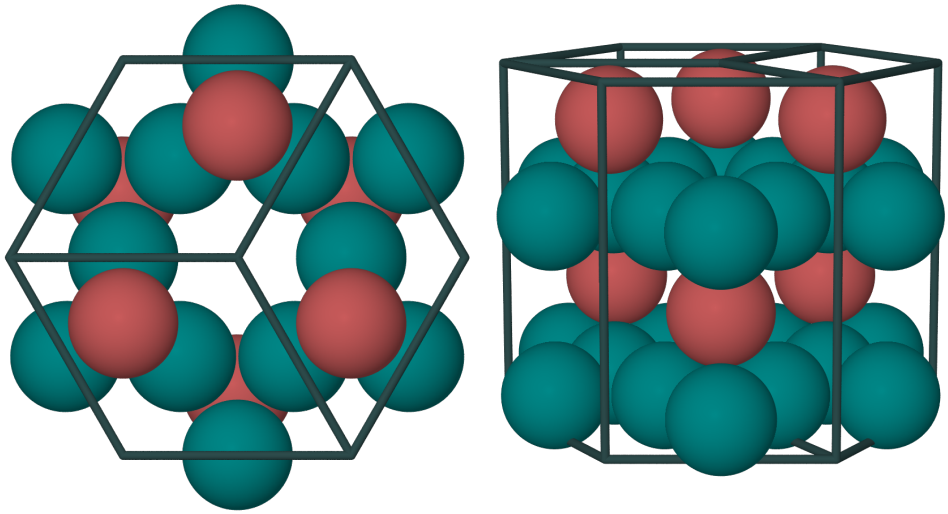

Figure 2.4: The conventional unit cell of the hexagonal tetrastack structure. Here the pink particles are used to highlight the shared corners of the tetrahedra that are eclipsed relative to one another. The blue particles form Kagome planes that are all eclipsed. The same Kagome planes emerge in the cubic polymorph, however, they are all staggered relative to one another.

Again, we can construct hexagonal tetrastack from a hexagonal unit cell, but with an eight particle motif:

$$\begin{aligned} \mathbf{z}_0 &= \frac{\mathbf{a}_1}{3} + \frac{2\mathbf{a}_2}{3} + \frac{3\mathbf{a}_3}{4}, & \mathbf{z}_1 &= \frac{2\mathbf{a}_1}{3} + \frac{\mathbf{a}_2}{3} + \frac{\mathbf{a}_3}{4}, \\ \mathbf{z}_2 &= \frac{\mathbf{a}_1}{2} + \frac{\mathbf{a}_2}{2}, & \mathbf{z}_3 &= \frac{\mathbf{a}_2}{2}, \\ \mathbf{z}_4 &= \frac{\mathbf{a}_1}{2} + \frac{\mathbf{a}_2}{2} + \frac{\mathbf{a}_3}{2}, & \mathbf{z}_5 &= \frac{\mathbf{a}_1}{2}, \\ \mathbf{z}_6 &= \frac{\mathbf{a}_2}{2} + \frac{\mathbf{a}_3}{2}, & \mathbf{z}_7 &= \frac{\mathbf{a}_1}{2} + \frac{\mathbf{a}_3}{2} \end{aligned} \tag{2.13}$$

The cubic and hexagonal tetrastack structures have the same space group as their diamond counterparts.

2.2 Crystal Structure Prediction

Crystal structure prediction (CSP) is the process of predicting the different ways an infinite number of particles or molecules organise themselves to form a crystal (i.e., the different polymorphs of the system). The physical properties of a material strongly depends on the arrangement of its constituent particles. An obvious example of this is provided by the different crystal phases of carbon, the properties of graphite are very different to that of diamond. Given this, reliably predicting the crystal structures of a molecular system has been a long-standing goal for many theoretical and computational chemists. CSP usually involves searching for the crystal structure that corresponds to the *global minimum* of a *potential energy surface*.[74,78]

2.2.1 Lattice Energy

The potential energy function defines a surface called the potential energy surface (PES). If we make the assumption that thermodynamics directs crystallisation, and temperature effects can be neglected, then we can also assume that the structure and dynamics of particles is guided by their underlying PES. Therefore, minima on the PES correspond to stable configurations of the system, and the global minimum is the thermodynamically most favourable conformation of the system at 0 K.[79] Due to the size of colloidal particles, we can make the assumption that the potential energy is dependent solely on their coordinates. The potential energy function for a system of colloidal particles can then be divided up into terms that account for individual particles, pairs, triplets, etc.:

$$U = \sum_i U(\mathbf{z}_i) + \sum_i \sum_{j>i} U(\mathbf{z}_i, \mathbf{z}_j) + \sum_i \sum_{j>i} \sum_{k>j} U(\mathbf{z}_i, \mathbf{z}_j, \mathbf{z}_k) + \cdots \tag{2.14}$$

If we assume there is no external field, it is possible to define the potential energy simply as a function of inter-particle distances (i.e., we can neglect the first term in Eqn. (2.14)). In addition to this we usually neglect three-body, and higher order terms, due to computational efficiency. This leaves us with a *pair potential*, and so the potential energy function depends solely on the

distance between pairs of particles, $\mathrm{z}_{ij} = \|\mathbf{z}_{ij}\| = \|\mathbf{z}_i - \mathbf{z}_j\|$:

$$U = \sum_{i=1}^{N-1} \sum_{j=i+1}^{N} U(\mathrm{z}_{ij}) \tag{2.15}$$

Therefore, for a system of N spherical and isotropic particles, the underlying PES is a function of $3N$ variables, as each particle has three translational coordinates describing its position in space. However, if the particles possess anisotropic interactions (e.g., spherical patchy particles) or are rigid bodies it is necessary to account for the orientation of the particles as well. So an additional three variables are then usually required to represent the orientation ($\hat{\mathbf{u}}$) of the particles, making the PES a function of $6N$ variables.

$$U = \sum_{i=1}^{N-1} \sum_{j=i+1}^{N} U(\mathrm{z}_{ij}, \hat{\mathbf{u}}_i, \hat{\mathbf{u}}_j) \tag{2.16}$$

For rigid bodies there is an added complication as the particle is built up from multiple rigidly connected sites. Therefore, it is necessary to define a center of mass and a reference geometry that describes the relative positions of each of the sites. Consider a system with N identical particles, where each particle is considered to be a rigid body that has N_s sites. Now consider the interaction between particles i and j, with sites a and b respectively. The distance between sites a and b is given by:

$$\mathrm{z}_{ab} = \|\mathbf{z}_i + \boldsymbol{R}_i \cdot \mathbf{z}_a^0 - \mathbf{z}_j - \boldsymbol{R}_j \cdot \mathbf{z}_b^0\| \tag{2.17}$$

where: $\mathbf{z}_i$ is the center of mass of particle i, $\mathbf{z}_a^0$ is the reference position of site a and $\boldsymbol{R}_i$ is the rotation matrix describing the orientation of particle i. The potential energy function is then:

$$U = \sum_{i}^{N} \sum_{j}^{N} \sum_{a}^{N_s} \sum_{b}^{N_s} U\Big(\mathrm{z}_{ab}, \hat{\mathbf{u}}_i, \hat{\mathbf{u}}_j\Big) \tag{2.18}$$

For crystal structures the particles are contained within a unit cell and so the potential energy function must also account for the lattice parameters: $\mathbf{p} = \{\mathrm{a}_1,\ \mathrm{a}_2,\ \mathrm{a}_3,\ \alpha,\ \beta,\ \gamma\}$. In addition to this we choose to focus on the energy associated with particles in a single unit cell, this is known as the *lattice energy*. The lattice energy is computed by focusing on a single unit cell and

computing the potential energy due to the interactions between particles in that cell, as well as the interactions of those particles with particles in surrounding cells. The distance between site a in the primary cell and b in the image cell is given by:

$$\mathrm{z}_{ab}^{[\mathbf{n}]} = \|\mathbf{z}_{ab} + \mathbf{A}\cdot\mathbf{n}\| = \|\mathbf{z}_{ab} + \mathbf{R}\| \tag{2.19}$$

The energy of the unit cell can be given by the equation:

$$U = \frac{1}{2}\sum_{\mathbf{n}}^{*}\sum_{i}^{N}\sum_{j}^{N}\sum_{a}^{N_s}\sum_{b}^{N_s} U\left(\mathrm{z}_{ab}^{[\mathbf{n}]}, \hat{\mathbf{u}}_i, \hat{\mathbf{u}}_j\right) \tag{2.20}$$

When $\mathbf{n}$ is equal to $\mathbf{0}$ (i.e., the primary cell) the interactions where $i = j$ are ignored, this is shown by the $(*)$ asterisk in the above summation. As we are only interested in the energy of the central unit cell a factor of $1/2$ is introduced as only half of the energy from the interaction can be attributed to the primary cell. Clearly Eqn. (2.20) is an infinite summation, which cannot be practically evaluated. In practice only the terms that have a significant contribution to the lattice energy are retained, this is usually done by truncating the sum at a given cutoff distance, r_c. The cutoff distance is chosen so that, for the pair potential being used, the energy associated with the interaction between two particles separated by this distance is approximately zero, this is shown graphically in **Figure** 2.5.

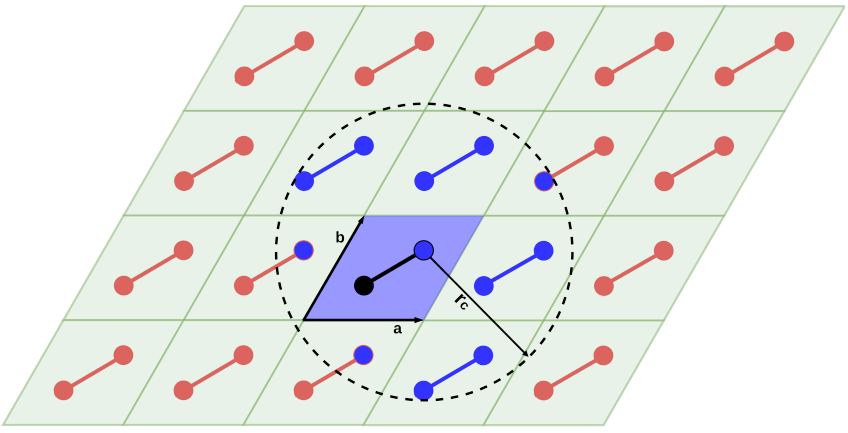

Figure 2.5: The central unit cell is shaded blue and contains a rigid dumbbell particle. Site 1 of the particle is also shaded in blue and interacts with the sites of other dumbbells in adjacent unit cells for which $\mathrm{z}_{ij}^{[\mathbf{n}]} \leq r_c$. The same would be done site 2 of the dumbbell, and the lattice energy of this crystal structure would be half the sum of those interactions.

Depending on the form of the potential energy function we can determine an appropriate cutoff for the lattice sum. If the interaction between the particles is short ranged, this cutoff only introduces negligible errors in the lattice energy. However, for long range interactions these errors become too large and require a more sophisticated approach. Using this cutoff, and the method of constructing image-lists in Ref. [80], we can determine the set of image cells that need to be considered in Eqn. (2.20). First we define a cube with vertices: $\mathbf{v}_i = r_c(\hat{\mathbf{x}}, \hat{\mathbf{y}}, \hat{\mathbf{z}})$, where $i \in [1-8]$. It is clear that this cube inscribes a sphere containing all particle sites that lie within the cutoff radius. We can then define the eight vertices of this cube as a fraction of cell vectors using the inverse cell matrix: $\mathbf{p}_i = \mathbf{A}^{-1} \cdot \mathbf{v}_i$.
The maximum number of images that need to be checked in each direction is then:

$$\mathrm{n}_1^m = \lceil \max_{\mathbf{p}_i} \{\mathbf{p}_i \cdot \hat{\mathbf{x}}\} \rceil \qquad \mathrm{n}_2^m = \lceil \max_{\mathbf{p}_i} \{\mathbf{p}_i \cdot \hat{\mathbf{y}}\} \rceil \qquad \mathrm{n}_3^m = \lceil \max_{\mathbf{p}_i} \{\mathbf{p}_i \cdot \hat{\mathbf{z}}\} \rceil \tag{2.21}$$

where: $\lceil x \rceil$ indicates the $ceiling(x)$ function (i.e., the smallest integer that is greater than or equal to x). If we define $\mathbf{n}^m = (\mathrm{n}_1^m, \mathrm{n}_2^m, \mathrm{n}_3^m)$, we can then re-write Eqn. (2.20) as:

$$U = \frac{1}{2} \sum_{\mathbf{n}=-\mathbf{n}^m}^{*\mathbf{n}=\mathbf{n}^m} \sum_{i,j}^{N} \sum_{a,b}^{N_s} U\Big(\mathrm{z}_{ab}^{[\mathbf{n}]}, \hat{\mathbf{u}}_i, \hat{\mathbf{u}}_j\Big), \qquad \text{where} \quad \mathrm{z}_{ab}^{[\mathbf{n}]} \leq r_c \tag{2.22}$$

2.2.2 Rotational Coordinates and Quaternions

Rotational coordinates encode the orientation of the particles, which can be expressed as a rotation with respect to some fixed frame of reference. There are multiple ways of performing rigid body rotation, in this work we use the angle-axis parameterisation of quaternions.

2.2.2.1 Rotation Matrices and Angle-Axis Coordinates

The simplest way to perform a 3D rotation is as a combination of three 2D rotations about the x- y- and z-axes. The following 3×3 matrices can be constructed to represent these rotations:

$$\boldsymbol{R}_x(\theta) = \begin{bmatrix} 1 & 0 & 0 \\ 0 & \cos\theta & \sin\theta \\ 0 & -\sin\theta & \cos\theta \end{bmatrix} \quad \boldsymbol{R}_y(\theta) = \begin{bmatrix} -\sin\theta & 0 & \cos\theta \\ 0 & 1 & 0 \\ \cos\theta & 0 & \sin\theta \end{bmatrix} \quad \boldsymbol{R}_z(\theta) = \begin{bmatrix} \cos\theta & \sin\theta & 0 \\ -\sin\theta & \cos\theta & 0 \\ 0 & 0 & 1 \end{bmatrix}$$

These matrices can then be combined to give a single 3×3 rotation matrix that describes all three rotations and can be used to transform the coordinates of a rigid body. The order in which the rotations are performed is important as matrix multiplication is not commutative (i.e. $\boldsymbol{R}_x\boldsymbol{R}_y\boldsymbol{R}_z \neq \boldsymbol{R}_y\boldsymbol{R}_z\boldsymbol{R}_x$). Instead of rotating the reference frame three times it is possible to achieve any orientation with a single rotation about some arbitrary axis, this is the angle-axis representation of rotations. A rotation vector can be defined: $\boldsymbol{u} = \theta\hat{\boldsymbol{u}}$, where, θ is the angle of rotation, $\hat{\boldsymbol{u}}$ is the axis about which the rotation occurs and $\boldsymbol{u}$ is the rotation vector. The rotation vector itself is not an operator, it instead encodes the information required to perform rotations.[81] Rodrigues' rotation formula computes a rotation matrix for a given rotation vector:

$$\boldsymbol{R}_{\hat{\boldsymbol{u}}}(\theta) = \mathbf{I} + \tilde{\boldsymbol{u}}\sin\theta + \tilde{\boldsymbol{u}}^2(1 - \cos\theta) \tag{2.23}$$

where, $\mathbf{I}$ is the identity matrix and $\tilde{\boldsymbol{u}}$ is the skew symmetric matrix of $\hat{\boldsymbol{u}}$. The derivatives of the rotation matrix with respect to the components of the rotation vector can then be found using Rodrigues' rotation formula:

$$\frac{\partial \boldsymbol{R}}{\partial u_k} = \frac{u_k \cos\theta}{\theta}\tilde{\boldsymbol{u}}^2 + (1 - \cos\theta)(\tilde{\boldsymbol{u}}_k\tilde{\boldsymbol{u}} + \tilde{\boldsymbol{u}}\tilde{\boldsymbol{u}}_k) + \frac{u_k \cos\theta}{\theta}\tilde{\mathbf{u}} + \sin\theta\tilde{\boldsymbol{u}}_k \tag{2.24}$$

2.2.2.2 Quaternions

Quaternions can be considered as four dimensional complex numbers (or hypercomplex numbers) consisting of one real component (a) and three imaginary components ($\boldsymbol{v}$), where i, j and k are the imaginary axes.[82,83] Quaternions are commonly written as:

$$\mathbf{q} = (a, \boldsymbol{v}), \qquad \boldsymbol{v} = (b, c, d) = bi + cj + dk, \qquad a, b, c, d \in \mathbb{R} \tag{2.25}$$

The axioms governing quaternion algebra are outlined in Sir William Rowan Hamilton's (their discoverer) *Elements of Quaternions* (Ref. [84]). Here we outline just the fundamental algebra of quaternions. The imaginary axes obey the fundamental equation:

$$i^2 = j^2 = k^2 = ijk = -1 \tag{2.26}$$

and have the following cyclic relationships:

$$ij = -ji = k, \qquad jk = -kj = i, \qquad ki = -ik = j \tag{2.27}$$

Quaternionic multiplication is related to the dot and cross products from standard vector analysis by the equality:[83]

$$\boldsymbol{v}_1\boldsymbol{v}_2 = -\boldsymbol{v}_1 \cdot \boldsymbol{v}_2 + \boldsymbol{v}_1 \times \boldsymbol{v}_2 \tag{2.28}$$

We define the dot product of quaternions as:

$$\mathbf{q}_1 \cdot \mathbf{q}_2 = a_1 a_2 + \boldsymbol{v}_1 \cdot \boldsymbol{v}_2 \tag{2.29}$$

The conjugate of a quaternion is defined as: $\overline{\mathbf{q}} = a - \boldsymbol{v}$, and the magnitude of a quaternion is defined as the dot product between the quaternion and its corresponding conjugate:

$$|\mathbf{q}|^2 = a^2 + \boldsymbol{v} \cdot \boldsymbol{v} = a^2 + {v_x}^2 + {v_y}^2 + {v_z}^2 \tag{2.30}$$

Given the conjugate and magnitude of a quaternion its inverse can also be defined as:

$$\mathbf{q}^{-1} = \frac{\overline{\mathbf{q}}}{|\mathbf{q}|^2} \tag{2.31}$$

Quaternions with a norm equal to one ($\|\mathbf{q}\| = 1$) are defined as *unit quaternions* and those with a zero real part ($a = 0$) are known as a *pure quaternion*. Rotations with quaternions are performed using unit quaternions. Any point to be rotated by a quaternion can be represented as a pure quaternion: $\mathbf{P} = (0, \mathbf{p})$, where $\mathbf{p} = (x, y, z)$ and represents the coordinates of point $\mathbf{P}$. Point $\mathbf{P}$ can then be rotated by a unit quaternion using the equation:

$$\mathbf{P}' = \mathbf{q}\mathbf{P}\mathbf{q}^{-1} = (0, \mathbf{p}') \tag{2.32}$$

The position of the new rotated point, $\mathbf{p}'$, is given by the equation:

$$\mathbf{p}' = a^2\mathbf{p} - \mathbf{p}(\boldsymbol{v} \cdot \boldsymbol{v}) + 2a(\boldsymbol{v} \times \mathbf{p}) + 2\boldsymbol{v}(\boldsymbol{v} \cdot \mathbf{p}) \tag{2.33}$$

This equation can subsequently be shown to be equivalent to Rodrigue's Rotation Formula. The polar form of unit quaternions allows us to write down quaternions in terms of angle-axis parameters:

$$\mathbf{q} = \cos\frac{\theta}{2} + \hat{\boldsymbol{u}}\sin\frac{\theta}{2} \tag{2.34}$$

where, $\hat{\boldsymbol{u}}$ is a unit vector along the selected rotation axis and θ is the angle of rotation. Additionally, we can use Eqn. (2.33) to construct a rotation matrix with quaternions:

$$\boldsymbol{R}(\mathbf{q}) = \begin{bmatrix} 2(a^2+b^2)-1 & 2(ad+bc) & 2(bd-ac) \\ 2(bc-ad) & 2(a^2+c^2)-1 & 2(ab+cd) \\ 2(ac+bd) & 2(cd-ab) & 2(a^2+d^2)-1 \end{bmatrix} \tag{2.35}$$

This allows us to represent the orientation of each particle using just three numbers, and extract the rotation matrix as needed. In practice we use the rotation matrix to rotate our particles during the simulation and store their orientations in terms of angle-axis parameters.

2.2.3 Derivatives of the Lattice Energy

During global optimisation simulations we require the derivatives of the lattice energy. Here we outline these derivatives for a system of particles considered to be rigid bodies.

$$\frac{\partial U(\mathrm{z}_{ab}^{[\mathbf{n}]})}{\partial \mathbf{z}_i} = \sum_{\mathbf{n}}^{*} \sum_{j\neq i} \sum_{a\in i} \sum_{b\in j} \frac{\partial U(\mathrm{z}_{ab}^{[\mathbf{n}]})}{\partial \mathrm{z}_{ab}^{[\mathbf{n}]}} \cdot \hat{\mathbf{z}}_{ab}^{[\mathbf{n}]} \tag{2.36}$$

We can parameterise a rotation matrix using angle-axis vectors, $\mathbf{u}$, allowing us to take the derivative with respect to a 3-vector, rather than a 3×3 matrix. The derivative of the potential energy with respect to component $k \in \{1,2,3\}$ of the rotation vector of particle i can then be defined as:

$$\frac{\partial U(\mathrm{z}_{ab}^{[\mathbf{n}]})}{\partial \mathrm{u}_k^i} = \sum_{\mathbf{n}}^{*} \sum_{j\neq i} \sum_{a\in i} \sum_{b\in j} \frac{\partial U(\mathrm{z}_{ab}^{[\mathbf{n}]})}{\partial \mathrm{z}_{ab}^{[\mathbf{n}]}} \cdot \hat{\mathbf{z}}_{ab}^{[\mathbf{n}]} \cdot \left(\frac{\partial \boldsymbol{R}_i}{\partial \mathrm{u}_k^i} \cdot \mathbf{r}_a^0 \right) \tag{2.37}$$

We can use the chain rule to take the derivative of the rotation matrix with respect to the angle-axis parameters via quaternions:

$$\frac{\partial \boldsymbol{R}(\mathbf{q})}{\partial \mathrm{u}_1} = \sum_{i=0}^{3} \frac{\partial \boldsymbol{R}}{\partial q_i} \frac{\partial q_i}{\partial \mathrm{u}_1}, \qquad \frac{\partial \boldsymbol{R}(\mathbf{q})}{\partial \mathrm{u}_2} = \sum_{i=0}^{3} \frac{\partial \boldsymbol{R}}{\partial q_i} \frac{\partial q_i}{\partial \mathrm{u}_2}, \qquad \frac{\partial \boldsymbol{R}(\mathbf{q})}{\partial \mathrm{u}_3} = \sum_{i=0}^{3} \frac{\partial \boldsymbol{R}}{\partial q_i} \frac{\partial q_i}{\partial \mathrm{u}_3} \tag{2.38}$$

where $\mathbf{q} = (a, b, c, d) = (q_0, q_1, q_2, q_3)$, and

$$\begin{aligned} \frac{\partial \boldsymbol{R}(\mathbf{q})}{\partial a} &= 2 \begin{bmatrix} a & -d & c \\ d & a & -b \\ -c & b & a \end{bmatrix} & \frac{\partial \boldsymbol{R}(\mathbf{q})}{\partial b} &= 2 \begin{bmatrix} b & c & d \\ c & -b & -a \\ d & a & -b \end{bmatrix} \\ \frac{\partial \boldsymbol{R}(\mathbf{q})}{\partial c} &= 2 \begin{bmatrix} -c & b & a \\ b & c & d \\ -a & d & -c \end{bmatrix} & \frac{\partial \boldsymbol{R}(\mathbf{q})}{\partial d} &= 2 \begin{bmatrix} -d & -a & b \\ a & -d & c \\ b & c & d \end{bmatrix} \end{aligned} \tag{2.39}$$

$$\frac{\partial \mathbf{q}}{\partial \mathrm{u}_1} = \begin{bmatrix} -a\mathrm{u}_1 \\ 2a + b{\mathrm{u}_1}^2 \\ b(\mathrm{u}_1\mathrm{u}_2) \\ b(\mathrm{u}_1\mathrm{u}_3) \end{bmatrix} \qquad \frac{\partial \mathbf{q}}{\partial \mathrm{u}_2} = \begin{bmatrix} -a\mathrm{u}_2 \\ b(\mathrm{u}_1\mathrm{u}_2) \\ 2a + b{\mathrm{u}_2}^2 \\ b(\mathrm{u}_2\mathrm{u}_3) \end{bmatrix} \qquad \frac{\partial \mathbf{q}}{\partial \mathrm{u}_3} = \begin{bmatrix} -a\mathrm{u}_3 \\ b(\mathrm{u}_1\mathrm{u}_3) \\ b(\mathrm{u}_2\mathrm{u}_3) \\ 2a + b{\mathrm{u}_3}^2 \end{bmatrix} \tag{2.40}$$

The derivative of the lattice energy with respect to the cell parameters, again, involves just applying the chain rule:

$$\frac{\partial U}{\partial \mathbf{p}} = \sum_{\mathbf{n}}^{*} \sum_{i} \frac{\partial U(\mathrm{z}_{ab}^{[\mathbf{n}]})}{\partial \mathbf{z}_i} \cdot \left(\frac{\partial \mathbf{A}}{\partial \mathbf{p}} \cdot \mathbf{n} \right) \tag{2.41}$$

we find that the derivative contains the derivative of the lattice energy with respect to the translational coordinates and involves a sum over the number of images and the number of particles, as does Eqn. (2.37). Therefore, computational overhead can be greatly reduced if the derivatives are all calculated in the same loop during the simulation.

It is also necessary to evaluate the derivative of the cell matrix with respect to the cell parameters, which are provided below:

$$\frac{\partial \mathbf{A}}{\partial \mathrm{a}_1} = \begin{bmatrix} 1 & 0 & 0 \\ 0 & 0 & 0 \\ 0 & 0 & 0 \end{bmatrix}$$

$$\frac{\partial \mathbf{A}}{\partial \mathrm{a}_2} = \begin{bmatrix} 0 & 0 & 0 \\ \cos\gamma & \sin\gamma & 0 \\ 0 & 0 & 0 \end{bmatrix}$$

$$\frac{\partial \mathbf{A}}{\partial \mathrm{a}_3} = \begin{bmatrix} 0 & 0 & 0 \\ 0 & 0 & 0 \\ \cos\beta & \left(\frac{\cos\alpha - \cos\beta\cos\gamma}{\sin\gamma}\right) & \frac{\sqrt{W}}{\sin\gamma} \end{bmatrix}$$

$$\frac{\partial \mathbf{A}}{\partial \alpha} = \begin{bmatrix} 0 & 0 & 0 \\ 0 & 0 & 0 \\ 0 & -\frac{\mathrm{a}_3 \sin\alpha}{\sin\gamma} & \frac{\mathrm{a}_3 \sin\alpha(\cos\alpha - \cos\beta\cos\gamma)}{\sqrt{W}\sin\gamma} \end{bmatrix}$$

$$\frac{\partial \mathbf{A}}{\partial \beta} = \begin{bmatrix} 0 & 0 & 0 \\ 0 & 0 & 0 \\ -\mathrm{a}_3 \sin\beta & \frac{\mathrm{a}_3 \sin\beta\cos\gamma}{\sin\gamma} & \frac{\mathrm{a}_3 \sin\alpha(\cos\alpha - \cos\beta\cos\gamma)}{\sqrt{W}\sin\gamma} \end{bmatrix}$$

$$\frac{\partial \mathbf{A}}{\partial \gamma} = \begin{bmatrix} 0 & 0 & 0 \\ -\mathrm{a}_2 \sin\gamma & \mathrm{a}_2 \cos\gamma & 0 \\ 0 & \mathrm{a}_3\left(\frac{\cos\beta - \cos\alpha\cos\gamma}{\sin^2\gamma}\right) & \mathrm{a}_3\left[\frac{\cos\gamma(\cos^2\alpha + \cos^2\beta) - \cos\alpha\cos\beta(1+\cos^2\gamma)}{\sqrt{W}\sin^2\gamma}\right] \end{bmatrix}$$

Table 2.1: Derivatives of cell matrix with respect to cell lengths, {a,b,c}, and the cell angles $\{\alpha, \beta, \gamma\}$

2.2.4 Energy Minimisation

Energy (or geometry) optimisation can be thought of as the process by which stationary points on the PES are found and characterised. Specifically, we are mainly interested in stationary points that are minima, as these correspond to stable configurations of the system, where the lowest-lying minima are candidates for the experimentally observed structures. At these minima the gradient of potential energy function is zero:

$$\nabla U(\mathbf{x}) = \begin{bmatrix} \dfrac{\partial U}{\partial \mathrm{z}_{1,x}} \\ \vdots \\ \dfrac{\partial U}{\partial \mathrm{z}_{N,z}} \\ \\ \dfrac{\partial U}{\partial \mathrm{u}_{1,1}} \\ \vdots \\ \dfrac{\partial U}{\partial \mathrm{u}_{N,3}} \\ \\ \dfrac{\partial U}{\partial \mathrm{a}_1} \\ \vdots \\ \dfrac{\partial U}{\partial \gamma} \end{bmatrix} = \mathbf{0} \tag{2.42}$$

where $\mathbf{x}$ corresponds to the coordinates of the system and the gradient of the lattice energy is a $6N + 6$ vector. Therefore, finding these stable configurations can be considered a numerical optimisation problem of the form:

$$\min_{\mathbf{x}} \{U(\mathbf{x}) : \mathbf{x} \in \mathbb{R}^{\mathrm{n}}\} \tag{2.43}$$

where, $\mathrm{n} = 6N + 6$. Here we focus on gradient based methods applied to the above problem, and so $U(\mathbf{x}) : \mathbb{R}^{\mathrm{n}} \to \mathbb{R}$ must be a continuously differentiable function. The most commonly used gradient based optimisation algorithms compute a search direction, $\boldsymbol{d}$, that points towards a local minimum and then determine how far in that direction to move.

These algorithms have the general update scheme:

$$\boldsymbol{x}_{k+1} = \boldsymbol{x}_k + \alpha_k \boldsymbol{d}_k \tag{2.44}$$

where k denotes the step iteration and α_k is the step-length and each step should satisfy the condition: $\mathrm{U}(\boldsymbol{x}_{k+1}) < \mathrm{U}(\boldsymbol{x}_k)$. We therefore require $\boldsymbol{d}_k$ to be a *descent direction*, meaning that $\boldsymbol{d}_k \cdot \mathbf{g}_k < 0$ (where $\mathbf{g}_k = \nabla U_k$), as this guarantees that U_k can be reduced along this direction. We can break down line search methods into three steps: (i) *compute the step-length*. (ii) *compute the step direction*. (iii) *update the coordinates of the system*. This process is repeated until a termination condition is satisfied. The step length, α_k is a positive scalar that is usually computed in such a way so as to give a considerable decrease in U_k, but not require too much computational time. This gives rise to what are known as *inexact line search* methods, where an α_k that satisfies certain sufficient descent conditions is identified. These conditions used to find α_k are discussed in more detail in *Appendix* A. Different gradient based optimisation algorithms are characterised according to the nature of the search direction used. Here we outline the two algorithms that are most commonly used in practice.

2.2.4.1 Nonlinear Conjugate Gradient Method

Minimisation algorithms that have much better convergence properties are the conjugate gradient methods. The search directions for these methods is generated by the update rule:

$$\boldsymbol{d}_{k+1} = -\mathbf{g}_{k+1} + \beta_k \boldsymbol{d}_k, \qquad \boldsymbol{d}_0 = -\mathbf{g}_0 \tag{2.45}$$

where β_k is a scalar known as the conjugate gradient update parameter, and different conjugate gradient methods correspond to different choices of β_k. The general idea for the conjugate gradient method is to select a new search direction that takes into account the previous direction, ensuring each step does not move too far away from the minimum found at the previous iteration. This is quite an attractive algorithm for multi-dimensional problems due to its computational efficiency: only the energy and the gradient need to be evaluated. A survey of the convergence properties for different conjugate gradient methods is given in Ref. [85].

2.2.4.2 Quasi-Newton Methods

The first and the second derivatives of the potential energy function can be used to define a local approximation to the PES using Taylor theorem:

$$U_{k+1}(\boldsymbol{d}_k) \equiv U(\mathbf{x}_k + \boldsymbol{d}_k) \approx U(\mathbf{x}_k) + \boldsymbol{d}_k^{\mathrm{T}}\mathbf{g}_k + \tfrac{1}{2}\boldsymbol{d}_k^{\mathrm{T}}\mathbf{H}_k\boldsymbol{d}_k \tag{2.46}$$

where, $\mathbf{H}_k$ is the Hessian matrix, a square matrix of second derivatives:

$$\mathbf{H} = \begin{bmatrix} \dfrac{\partial^2 U}{\partial \mathrm{x}_1^2} & \dfrac{\partial^2 U}{\partial \mathrm{x}_1 \partial \mathrm{x}_2} & \cdots & \dfrac{\partial^2 U}{\partial \mathrm{x}_1 \partial \mathrm{x}_\mathrm{n}} \\ \vdots & \vdots & \ddots & \vdots \\ \dfrac{\partial^2 U}{\partial \mathrm{x}_\mathrm{n} \partial \mathrm{x}_1} & \dfrac{\partial^2 U}{\partial \mathrm{x}_\mathrm{n} \partial \mathrm{x}_2} & \cdots & \dfrac{\partial^2 U}{\partial \mathrm{x}_\mathrm{n}^2} \end{bmatrix} \tag{2.47}$$

Differentiating Eqn. (2.46) with respect to the step direction we get:

$$\nabla U_{k+1}(\boldsymbol{d}_k) = \mathbf{g}_k + \mathbf{H}_k\mathbf{d}_k \tag{2.48}$$

When $\nabla U(\mathbf{x}_k + \boldsymbol{d}_k) = 0$ we have a stationary point, and so solving Eqn. (2.48) gives:

$$\mathbf{d}_k = -\mathbf{H}_k^{-1}\mathbf{g}_k \tag{2.49}$$

Thus is the Newton-Raphson step. If the PES is quadratic, only a single update is required to find the minimum. However, the PES is rarely quadratic and so multiple steps are often required to reach a minimum. Computing the Hessian at each iteration will be computationally expensive. Instead, methods that use an approximate Hessian are employed, quasi-Newton methods. The search direction for quasi-Newton methods can be generally defined as:

$$\boldsymbol{d}_k = -\boldsymbol{B}_k^{-1}\mathbf{g}_k \tag{2.50}$$

where $\boldsymbol{B}_k$ is a symmetric and positive definite matrix.

For each set of new coordinates, $\mathbf{x}_{k+1}$, we generate a new quadratic model of the PES that takes the form:

$$E_{k+1}(\boldsymbol{d}_k) = U(\mathbf{x}_k) + \boldsymbol{d}_k^{\mathrm{T}}\mathbf{g}_{k+1} + \tfrac{1}{2}\boldsymbol{d}_k^{\mathrm{T}}\boldsymbol{B}_k\boldsymbol{d}_k \tag{2.51}$$

To ensure that this new model is valid we require that the gradient of E_{k+1} is the same as that of the true PES for the latest two iterates $\mathbf{x}_k$ and $\mathbf{x}_{k+1}$. The second condition can be written as: $\nabla E_{k+1}(\mathbf{0}) = \mathbf{g}_{k+1}$, and so is automatically satisfied, and the first condition is the same as setting $\boldsymbol{d}_k$ to be the negative of the displacement from the previous iteration:

$$\nabla E_{k+1}(-\alpha_k\boldsymbol{d}_k) = \mathbf{g}_{k+1} - \alpha_k\boldsymbol{B}_{k+1}\boldsymbol{d}_k = \mathbf{g}_k \tag{2.52}$$

By rearranging, we get:

$$\boldsymbol{C}_{k+1}\mathbf{y}_k = \mathbf{s}_k \tag{2.53}$$

where, $\boldsymbol{B}_k^{-1} = \boldsymbol{C}_k$, $\mathbf{s}_k = \alpha_k\boldsymbol{d}_k = \mathbf{x}_{k+1} - \mathbf{x}_k$ and $\mathbf{y}_k = \mathbf{g}_{k+1} - \mathbf{g}_k$. These are the *secant conditions*, and they ensure that $\boldsymbol{C}_{k+1}$ behaves, at least, like the Hessian at $\mathbf{x}_k$ and $\mathbf{x}_{k+1}$. We want any potential approximation to the Hessian to satisfy the secant conditions, additionally we impose the constraint that $\boldsymbol{C}_{k+1}$ must be a symmetric and positive definite matrix. Then to determine $\boldsymbol{C}_{k+1}$ uniquely, we impose one final condition: $\min_{\boldsymbol{C}} \|\boldsymbol{C} - \boldsymbol{C}_k\|$ where, $\|\cdot\|$ is the weighted Frobenius norm. This condition simply states that out of all possible symmetric matrices that satisfy the secant condition, $\boldsymbol{C}_{k+1}$ is the one which is closest to the current matrix $\boldsymbol{C}_k$. The unique solution to all of these conditions is then:

$$\boldsymbol{C}_{k+1} = (\boldsymbol{I} - \rho_k \cdot \mathbf{s}_k \otimes \mathbf{y}_k) \cdot \boldsymbol{C}_k \cdot (\boldsymbol{I} - \rho_k \cdot \mathbf{y}_k \otimes \mathbf{s}_k) + \rho_k \mathbf{s}_k \otimes \mathbf{s}_k \tag{2.54}$$

where $\rho_k = 1/\mathbf{y}_k \cdot \mathbf{s}_k$. This is known as the BFGS step, named after its discoverers Broyden, Fletcher, Goldfarb and Shanno. A complete discussion regarding the derivation and the convergence properties of the BFGS method can be found in Ref. [86]. There is no special definition for $\boldsymbol{C}_0$ which works in all cases, and it is often easiest to simply set it to be the identity matrix.

Rather than storing the full n × n Hessian, we can implicitly represent the matrix by saving a certain number, m, of the vectors $\mathbf{s}_i$ and $\mathbf{y}_i$, from which the product $\boldsymbol{C}_k \cdot \mathbf{g}_k$ can be calculated.

After each iteration of the algorithm the oldest set of vectors $\{\mathbf{s}_i, \mathbf{y}_i\}$ is replaced by those calculated from the current step, $\{\mathbf{s}_k, \mathbf{y}_k\}$. This way the approximation to the Hessian contains the curvature information from the m most recent steps. This is known as the limited-memory BFGS (L-BFGS) method.[86]

2.2.5 Basin-Hopping Global Optimisation

We have just covered how to perform energy minimisation, however, the PES is vast and noisy, with the number of potential structures increasing exponentially with the number of particles in the unit cell. This means that a single energy minimisation step is unlikely to provide us with the global minimum. In order to find the global minimum we must couple the energy minimisation algorithms outlined above with some way of searching the PES, we call this a *global optimisation algorithm*. Here we outline the *basin-hopping* global optimisation method, as it is easy to implement and has become the standard method for the global optimisation of energy landscapes.[87] We define a basin as a region of the PES associated with a local minimum such that optimisation from any point in the basin gives the same local minimum.

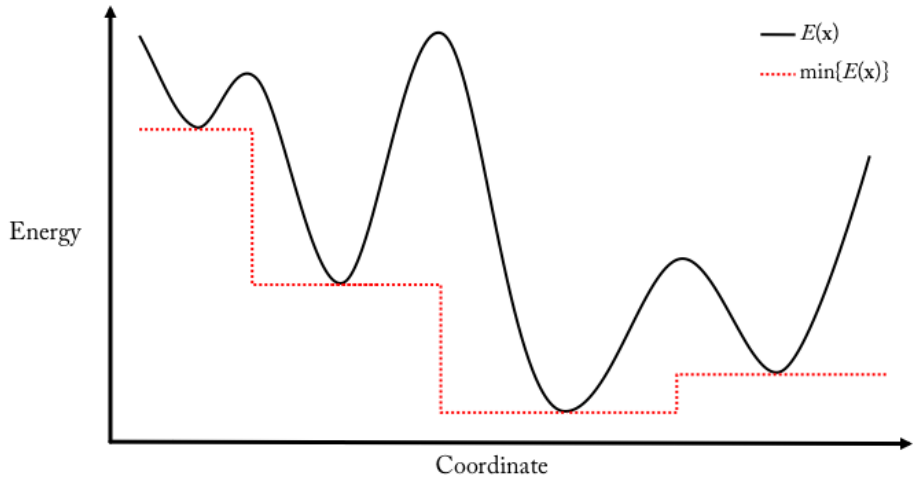

Figure 2.6: Basin Transformation of a 2D Potential Energy Surface

The PES can be deformed into a function of its basins so as to produce a new potential energy function, $\widetilde{U}(\mathbf{x})$, that resembles a step function (**Figure** 2.6). The energy of the global minimum is unchanged and the relative energies of the local minima are also unchanged.

This transformed PES is given by the complete set of local minima on the original PES:

$$\widetilde{U}(\mathbf{x}) = \left\{ \min_{\mathbf{x}} U(\mathbf{x}) \right\} \tag{2.55}$$

Combining this transformation with a search strategy is known as basin-hopping global optimisation.[88] The simplest search strategy employed is canonical Monte-Carlo sampling with the acceptance probability of each random step given by the Metropolis criterion, $\exp\left(-\frac{\Delta U}{k_B T}\right)$, where T is a fictitious temperature and k_B is Boltzmann's constant.

Algorithm 1: Basic Outline for the Basin-Hopping algorithm

1 $\mathbf{x}_0 \leftarrow$ random initial configuration
2 $\mathbf{x}_{\text{old}} \leftarrow$ Energy Minimisation($\mathbf{x}_0$)
3 $U_{\text{old}} \leftarrow U(\mathbf{x}_{\text{old}})$
4 $j = 0$
5 **for** $i = 1$ **to** n **do**
6 $\quad \mathbf{x}_i \leftarrow \mathbf{x}_{\text{old}} + \Delta\mathbf{x}_i$
7 $\quad \mathbf{x}_{\text{new}} \leftarrow$ Energy Minimisation($\mathbf{x}_i$)
8 $\quad U_{\text{new}} \leftarrow U(\mathbf{x}_{\text{new}})$
9 $\quad r \leftarrow \text{random}(0, 1)$
10 $\quad$ **if** $U_{new} < U_{old}$ OR $r \leq \exp\left(-\frac{U_{new} - U_{old}}{k_B T}\right)$ **then**
11 $\quad\quad \mathbf{X}_j \leftarrow \mathbf{x}_{\text{new}}$, $j \leftarrow j + 1$
12 $\quad\quad U_{\text{old}} \leftarrow U_{\text{new}}$, $\mathbf{x}_{\text{old}} \leftarrow \mathbf{x}_{\text{new}}$
13 $\quad$ **end**
14 **end**
15 **return X**

In order to properly search the PES the coordinates of the system are randomly perturbed at each iteration of the algorithm (line 6 of ALGORITHM 1). Each perturbation should be a uniform step in that parameter space, and so it necessary to account for the differences in translational, rotational and lattice parametres during this step.[79,88]

2.3 Photonic Crystals

We are interested in investigating the photonic properties of colloidal open crystals. Therefore, in this section we introduce some of the key concepts required to understand photonic band structures, and the emergence of a photonic band gap. We begin by defining a single governing equation for electromagnetic states, which can be found by rearranging Maxwell's equations in macroscopic media:

$$\nabla \times \left(\frac{1}{\varepsilon(\mathbf{r})} \nabla \times \mathbf{H}(\mathbf{r}) \right) = \frac{\omega^2}{c^2} \mathbf{H}(\mathbf{r}) \tag{2.56}$$

This is known as the *master equation*, where $\mathbf{H}(\mathbf{r})$ is an eigenmode corresponding to one of the sinusoidal monochromatic waves from which the magnetic field is constructed, ω is the corresponding angular frequency, $\varepsilon(\mathbf{r})$ is the dielectric constant of a non-uniform medium and c is the vacuum speed of light. The equation is derived from Maxwell's equations in Appendix B.1.

2.3.1 Periodic Functions and the Reciprocal Lattice

The optical properties of a photonic crystal are clearly governed by its dielectric function, $\varepsilon(\mathbf{r})$, which must be periodic due to the translational symmetry of the crystal: $\varepsilon(\mathbf{r}) = \varepsilon(\mathbf{r} + \mathbf{R})$, this condition is true for all points in space, $\mathbf{r}$, and for all lattice vectors, $\mathbf{R}$.[16] We can express periodic functions using the inverse Fourier transform:

$$\varepsilon(\mathbf{r}) = \int \mathrm{d}^3\boldsymbol{k}\ \widetilde{\varepsilon}(\boldsymbol{k}) e^{i\boldsymbol{k}\cdot\mathbf{r}} \tag{2.57}$$

where, $\widetilde{\varepsilon}(\boldsymbol{k})$ is the Fourier coefficient of the plane wave, $e^{i\boldsymbol{k}\cdot\mathbf{r}}$, with wave vector $\boldsymbol{k}$. The wave vector has a magnitude equal to the wavenumber, $k = 2\pi/\lambda$, where λ is the wavelength of the plane wave, and a direction perpendicular to the wavefronts of the plane wave.[16,72,73] Therefore, the wave vector defines the wavelength and the direction of propagation for a plane wave. Due to the translational symmetry of the photonic crystal we can also write:

$$\varepsilon(\mathbf{r} + \mathbf{R}) = \int \mathrm{d}^3\boldsymbol{k}\ \widetilde{\varepsilon}(\boldsymbol{k}) e^{i\boldsymbol{k}\cdot\mathbf{r}} e^{i\boldsymbol{k}\cdot\mathbf{R}} = \int \mathrm{d}^3\boldsymbol{k}\ \widetilde{\varepsilon}(\boldsymbol{k}) e^{i\boldsymbol{k}\cdot\mathbf{r}} \tag{2.58}$$

Therefore, when $\widetilde{\varepsilon}(\boldsymbol{k}) \neq 0$, we have $e^{i\boldsymbol{k}\cdot\mathbf{R}} = 1$, for all $\mathbf{R}$, and so we can say: $\boldsymbol{k}\cdot\mathbf{R} = 2\pi l, \quad l \in \mathbb{Z}$. The wave vectors that satisfy this condition are known as reciprocal lattice vectors, which we usually denote as $\mathbf{G}$. Just as is the case for the direct lattice vectors, the linear combination of the reciprocal lattice vectors gives rise to the reciprocal lattice:

$$\mathbf{G} = \sum_{i=1}^{3} m_i \mathbf{b}_i \tag{2.59}$$

where, $\mathbf{b}_i$ is a primitive reciprocal lattice vector, and we then have:

$$\mathbf{G}\cdot\mathbf{R} = (m_1\mathbf{b}_1 + m_2\mathbf{b}_2 + m_3\mathbf{b}_3)\cdot(n_1\mathbf{a}_1 + n_2\mathbf{a}_2 + n_3\mathbf{a}_3) = 2\pi l \tag{2.60}$$

If we say that $l = \sum_{i=1}^{3} m_i n_i$ and $\mathbf{a}_i\mathbf{b}_i = \delta_{ij}$, where δ_{ij} is the Kronecker delta, then the primitive reciprocal lattice vectors are given by:

$$\mathbf{b}_1 = 2\pi\frac{\mathbf{a}_2\times\mathbf{a}_3}{\mathbf{a}_1\cdot(\mathbf{a}_2\times\mathbf{a}_3)} \qquad \mathbf{b}_2 = 2\pi\frac{\mathbf{a}_3\times\mathbf{a}_1}{\mathbf{a}_2\cdot(\mathbf{a}_1\times\mathbf{a}_3)} \qquad \mathbf{b}_3 = 2\pi\frac{\mathbf{a}_1\times\mathbf{a}_2}{\mathbf{a}_3\cdot(\mathbf{a}_1\times\mathbf{a}_2)} \tag{2.61}$$

This allows us to write the inverse Fourier transform of any periodic function as a sum over the reciprocal lattice vectors (we can ignore wave vectors that are not reciprocal lattice vectors):[16,72,73]

$$\varepsilon(\mathbf{r}) = \sum_{\mathbf{G}} \widetilde{\varepsilon}(\mathbf{G}) e^{i\mathbf{G}\cdot\mathbf{r}} \tag{2.62}$$

2.3.1.1 Brillouin Zones

The reciprocal lattice vectors also define a unit cell in reciprocal space, just like the direct lattice vectors do. The Wigner-Seitz unit cell of the reciprocal lattice is known as the Brillouin zone, where the Brillouin zone that contains the origin is called the 1st Brillouin zone. Other Brillouin zones are simply copies of the 1st Brillouin zone, translated by a reciprocal lattice vector $\mathbf{G}$. This means that for any wave vector $\boldsymbol{k}'$, there is always a wave vector $\boldsymbol{k}$ in the 1st Brillouin zone related to it by $\boldsymbol{k}' = \boldsymbol{k} + \mathbf{G}$. Therefore, we can say that two plane waves with wave vectors that differ by a reciprocal lattice vector are equivalent when $\mathbf{r} = \mathbf{R}$ (i.e., $e^{i\boldsymbol{k}\cdot\mathbf{R}} = e^{i\boldsymbol{k}'\cdot\mathbf{R}}$).[72]

2.3.2 Plane Wave Expansion and Photonic Band Structure

The master equation can be written to resemble a traditional eigenvalue problem:

$$\hat{\Theta}\mathbf{H}(\mathbf{r}) = \frac{\omega^2}{c^2}\mathbf{H}(\mathbf{r}) \tag{2.63}$$

where $\hat{\Theta}$ is the differential operator that takes the curl, divides by $\varepsilon(\mathbf{r})$ and takes the curl again.[16] Using Bloch-Floquet theory (see Appendix B.3) we can express the eigenmodes as a product of an envelope function $\mathbf{h}_{\boldsymbol{k}}(\mathbf{r})$ that has the same periodicity as the photonic crystal, and a plane wave $e^{i\boldsymbol{k}\cdot\mathbf{r}}$ that acts as a phase factor. We can then label each eigenmode according to its wave vector, $\boldsymbol{k}$, which together with the envelope function, $\mathbf{h}_{\boldsymbol{k}}(\mathbf{r})$, provides all of the necessary information about the eigenmode.[72,73] We can then write the master equation as:

$$\begin{aligned} \nabla \times \varepsilon(\mathbf{r})^{-1}\nabla \times (\mathbf{h}_{\boldsymbol{k}}(\mathbf{r})e^{i\boldsymbol{k}\cdot\mathbf{r}}) &= \frac{\omega_{\boldsymbol{k}}^2}{c^2}(\mathbf{h}_{\boldsymbol{k}}(\mathbf{r})e^{i\boldsymbol{k}\cdot\mathbf{r}}) \\ (i\boldsymbol{k}+\nabla) \times \varepsilon(\mathbf{r})^{-1}(i\boldsymbol{k}+\nabla) \times \mathbf{h}_{\boldsymbol{k}}(\mathbf{r}) &= \frac{\omega_{\boldsymbol{k}}^2}{c^2}\mathbf{h}_{\boldsymbol{k}}(\mathbf{r}) \end{aligned} \tag{2.64}$$

Due to the periodicity of the envelope function we can expand it as a Fourier series:

$$\mathbf{h}_{\boldsymbol{k}}(\mathbf{r}) = \sum_{\mathbf{G}} \mathbf{c}_{\boldsymbol{k}}(\mathbf{G})e^{i\mathbf{G}\cdot\mathbf{r}} \tag{2.65}$$

Therefore, the eigenmodes can be expressed as:

$$\mathbf{H}_{\boldsymbol{k}}(\mathbf{r}) = \left(\sum_{\mathbf{G}} \mathbf{c}_{\boldsymbol{k}}(\mathbf{G})e^{i\mathbf{G}\cdot\mathbf{r}}\right)e^{i\boldsymbol{k}\cdot\mathbf{r}} \tag{2.66}$$

The dielectric function, $\varepsilon(\mathbf{r})$, also inherits the periodicity of the crystal:

$$\frac{1}{\varepsilon(\mathbf{r})} = \sum_{\mathbf{G}} \kappa(\mathbf{G})e^{i\mathbf{G}\cdot\mathbf{r}} \tag{2.67}$$

where the Fourier coefficients, $\kappa(\mathbf{G})$, are obtained by integrating over the unit cell:

$$\kappa(\mathbf{G}) = \frac{1}{\Omega}\int_{\Omega} \frac{1}{\varepsilon(\mathbf{r})}e^{-i\mathbf{G}\cdot\mathbf{r}}\,\mathrm{d}\mathbf{r} \tag{2.68}$$

If we substitute Eqns. (2.66) and (2.67) into (2.64) our eigenvalue problem becomes:

$$-\sum_{\mathbf{G}} \kappa(\mathbf{G}'-\mathbf{G})(\boldsymbol{k}+\mathbf{G}')\times(\boldsymbol{k}+\mathbf{G})\times\mathbf{c}_{\boldsymbol{k}}(\mathbf{G}) = \frac{\omega_{\boldsymbol{k}}^2}{c^2}\mathbf{c}_{\boldsymbol{k}}(\mathbf{G}') \tag{2.69}$$

Eqn. (2.69) is an infinite set of linear equations for the infinite set of Fourier coefficients, $\mathbf{c}_{\boldsymbol{k}}(\mathbf{G})$. Each coefficient is a three-vector; however, using the divergence condition from Eqn. (B.20) and Bloch-Floquet theorem we can reduce the number of degrees of freedom by one:

$$\nabla\cdot\Big\{\mathbf{c}_{\boldsymbol{k}}(\mathbf{G})\exp[i(\boldsymbol{k}+\mathbf{G})\cdot\mathbf{r}]\Big\} = -(\boldsymbol{k}+\mathbf{G})\cdot\Big\{\mathbf{c}_{\boldsymbol{k}}(\mathbf{G})\exp[i(\boldsymbol{k}+\mathbf{G})\cdot\mathbf{r}]\Big\} = 0 \tag{2.70}$$

We can choose to represent the coefficients as a linear combination of two orthogonal unit vectors:

$$\mathbf{c}_{\boldsymbol{k}}(\mathbf{G}) = \mathrm{c}_{1,\mathbf{G}}^{\boldsymbol{k}}\hat{\mathbf{e}}_{1,\mathbf{G}} + \mathrm{c}_{2,\mathbf{G}}^{\boldsymbol{k}}\hat{\mathbf{e}}_{2,\mathbf{G}} \tag{2.71}$$

where the unit vectors are also perpendicular to $(\boldsymbol{k}+\mathbf{G})$:

$$\hat{\mathbf{e}}_{1,\mathbf{G}}\times\hat{\mathbf{e}}_{2,\mathbf{G}} = \frac{\boldsymbol{k}+\mathbf{G}}{|\boldsymbol{k}+\mathbf{G}|} \tag{2.72}$$

Our eigenvalue problem then becomes:

$$\sum_{\mathbf{G}} \kappa(\mathbf{G}'-\mathbf{G})|\boldsymbol{k}+\mathbf{G}'||\boldsymbol{k}+\mathbf{G}| \begin{pmatrix} \hat{\mathbf{e}}_{2,\mathbf{G}}\cdot\hat{\mathbf{e}}_{2,\mathbf{G}} & -\hat{\mathbf{e}}_{1,\mathbf{G}}\cdot\hat{\mathbf{e}}_{2,\mathbf{G}} \\ -\hat{\mathbf{e}}_{2,\mathbf{G}}\cdot\hat{\mathbf{e}}_{1,\mathbf{G}} & \hat{\mathbf{e}}_{1,\mathbf{G}}\cdot\hat{\mathbf{e}}_{1,\mathbf{G}} \end{pmatrix} \begin{pmatrix} \mathrm{c}_{1,\mathbf{G}}^{\boldsymbol{k}} \\ \mathrm{c}_{2,\mathbf{G}}^{\boldsymbol{k}} \end{pmatrix} = \frac{\omega_{\boldsymbol{k}}^2}{c^2} \begin{pmatrix} \mathrm{c}_{1,\mathbf{G}}^{\boldsymbol{k}} \\ \mathrm{c}_{2,\mathbf{G}}^{\boldsymbol{k}} \end{pmatrix} \tag{2.73}$$

We can solve Eqn. (2.73) numerically using a finite set of reciprocal lattice vectors of size N, where we diagonalise a $2N\times 2N$ matrix. However, there are better ways of solving the problem. For instance, the unconstrained conjugate gradient method can be applied to minimise the Rayliegh quotient to determine the lowest eigenfrequency, then all subsequent eigenfrequencies are found by minimising the Rayleigh quotient with the added constraint that the eigenmode must be orthogonal to all previously found eigenmodes.[89]

Regardless of the method used, we still have infinitely many wavevectors to solve for. However, by applying the Bloch-Floquet theorem to an eigenmode with the wave vector $\boldsymbol{k}' = \boldsymbol{k} + \mathbf{G}'$, we can show that we need only consider wave vectors in the 1st Brillouin zone:

$$\begin{aligned} \mathbf{H}_{\boldsymbol{k}'}(\mathbf{r}) &= \mathbf{h}_{\boldsymbol{k}'}(\mathbf{r}) e^{i(\boldsymbol{k}+\mathbf{G}')\cdot\mathbf{r}} \\ &= \sum_{\mathbf{G}} \mathbf{c}_{\boldsymbol{k}'}(\mathbf{G}) e^{i(\boldsymbol{k}+\mathbf{G}'+\mathbf{G})\cdot\mathbf{r}} \\ &= \left(\sum_{\mathbf{G}} \mathbf{c}_{\boldsymbol{k}'}(\mathbf{G}) e^{i(\mathbf{G}'+\mathbf{G})\cdot\mathbf{r}} \right) e^{i\boldsymbol{k}\cdot\mathbf{r}} \end{aligned} \tag{2.74}$$

If we then make a change of variables: $\mathbf{G} \to \mathbf{G} - \mathbf{G}'$, we have:

$$\mathbf{H}_{\boldsymbol{k}'}(\mathbf{r}) = \left(\sum_{\mathbf{G}} \mathbf{c}_{\boldsymbol{k}'}(\mathbf{G}) e^{i\mathbf{G}\cdot\mathbf{r}} \right) e^{i\boldsymbol{k}\cdot\mathbf{r}} \tag{2.75}$$

From this we see that the Fourier coefficients of $\mathbf{H}_{\boldsymbol{k}'}(\mathbf{r})$, and in fact any eigenmode with a wave vector of the form $\boldsymbol{k}' = \boldsymbol{k} + \mathbf{G}'$, are also eigenvectors of Eqn. (2.69).[73] This means that, for each wave vector, there are infinitely many solutions to Eqn. (2.69), where the coefficients with wave vectors that differ by a reciprocal lattice vector (i.e., $\mathbf{c}_{\boldsymbol{k}}$, $\mathbf{c}_{\boldsymbol{k}'}$, $\mathbf{c}_{\boldsymbol{k}''}$, ...) are all coupled. The eigenmodes can then be recovered from their corresponding Fourier coefficients using Eqn. (2.66). This means that we only need to consider wave vectors that lie in the 1st Brillouin zone during our calculations. For each wave vector we will have the set of eigenfrequencies $\{\omega_{n,\boldsymbol{k}}\}$, where $\omega_{n,\boldsymbol{k}} < \omega_{n+1,\boldsymbol{k}} < \omega_{n+2,\boldsymbol{k}}$ and n is known as the band index label. We therefore have a discrete eigenfrequency spectrum for each $\boldsymbol{k}$ (much like how the energy levels of 'the particle in a box' are quantized or how a rigidly held string has an infinite number of normal modes) due to modes from the n^{th} Brillouin zone being 'folded' back into the 1st Brillouin zone (and, as will be discussed in the next section due to Bragg reflection of the modes).

For two- and three-dimensional photonic crystals we do not even need to consider the entire 1st Brillouin zone as the reciprocal lattice inherits the point symmetry of the direct lattice. Instead we only consider wave vectors that lie in the region of the 1st Brillouin zone which contains wave vectors that are not related by the symmetry of the crystal, known as the irreducible Brillouin zone. We expect the frequency to vary continuously with $\boldsymbol{k}$ for a given n, and so we say that each family of continuous functions $\{\omega_n(\boldsymbol{k})\}$ form bands, which collectively form the

photonic band structure, with each eigenfrequency having the corresponding eigenmode $\mathbf{H}_{n\boldsymbol{k}}(\mathbf{r})$. We are only concerned with determining whether a particular structure possesses a photonic band gap (PBG), which we define as a frequency gap between two bands that extends across the entire width of the band structure. The minima and maxima of a given band (which determine the existence of a band gap) usually appear at the edges of the Brillouin zone, and so band structures are usually computed only for wave vectors that lie on the edge of the Brillouin zone.[16] We also require the Fourier coefficients of the dielectric function, Eqn. (2.68), in order to solve Eqn. (2.69). We can do this by dividing the unit cell into a square mesh, where the nodes of the square contain information about the permittivity of the crystal at that point, allowing us to replace the integral in (2.68) with a summation.

2.3.3 Origin of the Photonic Band Gap

The opening of a PBG in photonic crystals is understood to be due to an interplay between macroscopic Bragg scattering and the Mie resonances of the individual scattering centres. Here we briefly outline the origin of these two mechanisms.

2.3.3.1 Bragg Scattering Mechanism

A complete photonic band gap is a range of frequencies in which there are no propagating eigenmodes (i.e., modes with a real $\boldsymbol{k}$) for any $\boldsymbol{k}$. A stop band is an incomplete photonic band gap, which only exists over a subset of all possible wave vectors. However, the origins of both is the same. The physical origin of a photonic band gap can be easily understood by considering the multilayer film (see SECTION 1.1), where we have a structure of alternating dielectric constant, ε_1 and ε_2, such that $\varepsilon_1 > \varepsilon_2$. The unit cell of this one-dimensional crystal contains two particles, one of each dielectric material, and has a length of a. We can extend this conceptual crystal into a three-dimensional structure by considering the particles to be slabs of infinite height and width, but of depth $a/2$. We align the slabs so that the crystal has continuous translational symmetry in the x-y plane, and discrete translational symmetry along the z-axis. As the crystal only has periodicity along the z-axis, our problem is one-dimensional as we only have a single non-zero primitive lattice vector, $\mathbf{a} = (0, 0, a)$, and primitive reciprocal lattice vector, $\mathbf{b} = (0, 0, 2\pi/a)$. We also only consider electromagnetic waves with wave vectors

aligned with the z-axis, $\boldsymbol{k} = (0, 0, k)$ (i.e., the direction of the waves is perpendicular to the surface of the slabs). Due to the 1D nature of the problem we can express our eigenmodes as:

$$\mathbf{E}(z) = \mathbf{e}(z)e^{ikz} \tag{2.76}$$

In 1D the Bragg condition, $(\boldsymbol{k} + \mathbf{G})^2 = k^2$, for the diffraction of a wave becomes:

$$k = \pm\frac{1}{2}G = \pm\frac{n\pi}{a} \tag{2.77}$$

where, $G = 2\pi n/a$ is a reciprocal lattice vector and $n \in \mathbb{Z}$. Therefore, electromagnetic waves with wave vectors $k = \pm\pi/a$ will be reflected, creating two standing waves of the form:

$$\begin{aligned} \mathbf{E}_+(z) &\propto e^{i\pi z/d} + e^{-i\pi z/d} = 2\cos(\pi z/a) \\ \mathbf{E}_-(z) &\propto e^{i\pi z/d} - e^{-i\pi z/d} = 2i\sin(\pi z/a) \end{aligned} \tag{2.78}$$

The standing waves are labelled (+) or (-) according to whether or not they change sign when z is replaced by -z. We see in Figure 2.7 that the $\mathbf{E}_+(z)$ mode is more concentrated in the higher dielectric region than $\mathbf{E}_-(z)$. Therefore, due to Eqn. (B.32), the $\mathbf{E}_+(z)$ mode will have a lower frequency than the $\mathbf{E}_-(z)$ mode, resulting in a photonic band gap.[16,72] We refer to the bands associated with the two modes as the lower 'dielectric' band and higher 'air' band, and the size of the band gap increases as the dielectric contrast increases. We can also understand the existence of photonic band gaps by formulating our problem in the context of the electromagnetic variational theorem (see Appendix B.2). Using Eqns. (B.32) and (2.64) we see that the eigenfrequencies minimise the variational problem:

$$\omega^2_{n,\boldsymbol{k}} = \min_{\mathbf{e}_{n,\boldsymbol{k}}} \frac{\int \left|(i\boldsymbol{k} + \nabla) \times \mathbf{e}_{n,\boldsymbol{k}}(\mathbf{r})\right|^2}{\int \varepsilon(\mathbf{r})\left|\mathbf{e}_{n,\boldsymbol{k}}(\mathbf{r})\right|^2} c^2 \tag{2.79}$$

where, $\mathbf{e}_{n,\boldsymbol{k}}(\mathbf{r})$ is the envelope function of the electric field $\mathbf{E}_{n,\boldsymbol{k}}(\mathbf{r})$. We know that the modes with $n > 1$ are also constrained to be orthogonal to the lower bands from the variational theorem:

$$\langle \mathbf{h}_{m,\boldsymbol{k}}, \mathbf{h}_{n,\boldsymbol{k}} \rangle = \langle \mathbf{e}_{m,\boldsymbol{k}}, \varepsilon(\mathbf{r})\mathbf{e}_{n,\boldsymbol{k}} \rangle = 0 \qquad m < n \tag{2.80}$$

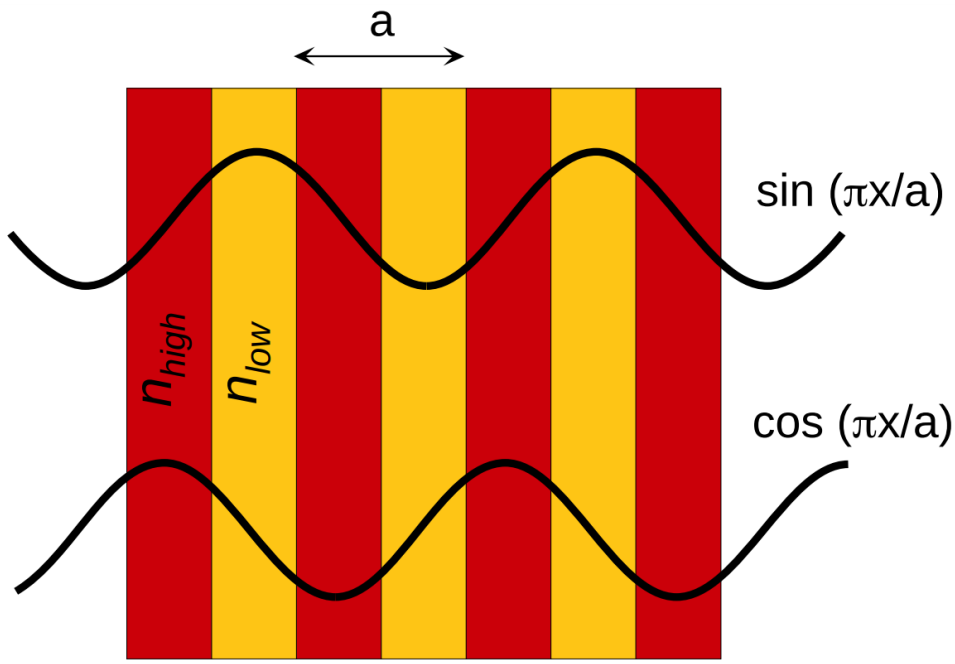

Figure 2.7: Cartoon depicting the origin of the band gap in a multilayer film. The pair of degenerate $k = \pm\pi/a$ planewaves split into $\cos(\pi x/a)$ and $\sin(\pi x/a)$ standing waves due to the periodicity of the film. The former has electric-field peaks in the high dielectric region (n_{high}) and so lies at a lower frequency than the latter (which peaks in the low dielectric region). Adapted from Ref. [90]

Therefore, band gaps arise (between adjacent bands) as the dielectric bands will be more concentrated in the high dielectric regions and so the air bands are forced into the low dielectric regions due to the orthogonality constraint. Additionally, lower frequency bands will, generally, have smaller spatial oscillations, when compared to higher frequency bands.We see that the photonic gap opens up at the edge of the Brillouin zone ($\omega = \pi c/a$) for the one-dimensional photonic crystal. We could, therefore, also expect to open up a band gap for three-dimensional photonic crystals if the edge of the Brillouin zone has the same magnitude in all directions, corresponding to a spherical Brillouin zone. There is, however, no three-dimensional crystal with a perfectly spherical Brillouin zone, and so stop gaps in different directions do not, usually, overlap perfectly with one another. However, if the dielectric contrast is large enough then it is possible to make these different gaps wide enough so that there is some overlap in frequency ranges, thus, giving rise to a complete photonic band gap. The fcc lattice has a Brillouin zone that is almost spherical (it is a truncated octahedron) and so the cubic diamond and tetrastack structures are very good candidates for a structures with a 3D photonic band gap.

The photonic properties of 2D photonic crystals differs depending on the polarisation of the incident radiation. We consider the two scenarios where either the magnetic field oscillates in the plane of the crystal and the electric field oscillates perpendicularly, or the electric field oscillates in the plane of the crystal and the magnetic field oscillates perpendicularly. We refer to these two polarisations as transverse magnetic (TM) or transverse electric (TE), respectively. A general rule of thumb has been established to open band gaps for each of these polarisations: TM PBGs are favoured for structures composed of isolated high dielectric scatterers, whereas TE PBGs are favoured in fully connected network structures.[16] There is no such definitive guideline for opening band gaps in 3D structures. However, it has been suggested that in order to maximise the band gap, the crystal should be composed of high dielectric particles that have a thin vein-like shape along which the electric field lines can traverse. This means that the lowest bands can be strongly confined to the high dielectric region, whereas the upper bands are moved to higher frequency as the particles will be unable to accommodate multiple orthogonal modes (except for two orthogonal polarizations).[16,91]

2.3.3.2 Mie Scattering Mechanism

We have just explained the existence of PBGs in terms of Bragg scattering of plane waves. However, for the Bragg condition to be met, and for standing waves to form, the reciprocal lattice of the structure must have delta function like peaks (i.e., it must be crystalline). This might suggest that amorphous dielectric materials are unable to possess a complete PBG. However, this is not the case. Therefore, Bragg scattering is not necessarily the only mechanism at play when considering the opening of a PBG in dielectric media.

The general solution to Maxwell's equations for an isolated sphere of arbitrary radius and refractive index was given in 1908 by Gustav Mie, who developed the theory to explain the scattering of light by small colloidal gold particles suspended in water.[92] A full description of Mie theory is beyond the scope of this thesis (the reader is instead referred to Ref. [93]). Mie theory provides an exact analytical solution for Maxwell's equations for the case of a plane wave incident on a spherical particle.[93] According to Mie theory, a dielectric sphere can possess strong scattering resonances, with the scattering proprieties of the sphere dependent on its dielectric constant and size relative to the wavelength of the incident light.[94]

We can consider a dielectric sphere to act as a localised basis for a photon with a wavelength corresponding to one its scattering resonances (much like an atomic orbital does for an electron). Although, the electromagnetic field is not truly localised as the field decays inversely with the distance from the centre of the sphere. These bound states of photons, and accompanying leak, are known as Mie modes.[95] If multiple scatterers are brought together, their individual resonant modes will hybridise, and energy bands will form. Then the ideas of the linear combination of atomic orbitals (LCAO) can be extended to the problem of electromagnetic waves, forming the tight binding model of photonic crystals.[96]

Figures 2.8 **(a)** and **(b)** show the internal electric field patterns for the zeroth and first order TM Mie resonances, respectively, for infinitely long dielectric cylinders. The frequency, and number of nodes in the internal field pattern, increases with the order of the resonant modes, where zeroth order and first order modes have no nodes and a single node, respectively.[97] Eigenmodes formed from the hybridisation of zeroth order Mie resonances will, therefore, have a lower frequency than those formed from first order resonances, just as is the case for the Bragg scattering picture (see **Figure** 2.8). This idea is validated by the observation that there is a direct correspondence between the band gaps calculated by the plane wave expansion method and the Mie resonances of an isolated sphere or cylinder.[96–100]

The Mie scattering mechanism therefore allows us to understand the opening of PBGs in structures that do not possess any periodicity. Additionally, this argument has not been limited to structures composed of spheres or cylinders, the idea has been extended to consider network structures where *Mie-type* resonances are understood to be vital in the opening of a PBG in both the crystalline and amorphous network gyroid and diamond structures.[23,101]

We have seen that there are two key mechanisms at play when discussing the opening of PBGs - Bragg and Mie scattering mechanisms. Therefore, photonic crystals with the widest PBGs are those which allow for a synergistic interplay between single scattering Mie resonances and macroscopic Bragg scattering. This is best achieved when the dielectric fill fraction of the crystal is optimised to allow for an overlap between the spectral ranges associated with the two mechanisms.[102]

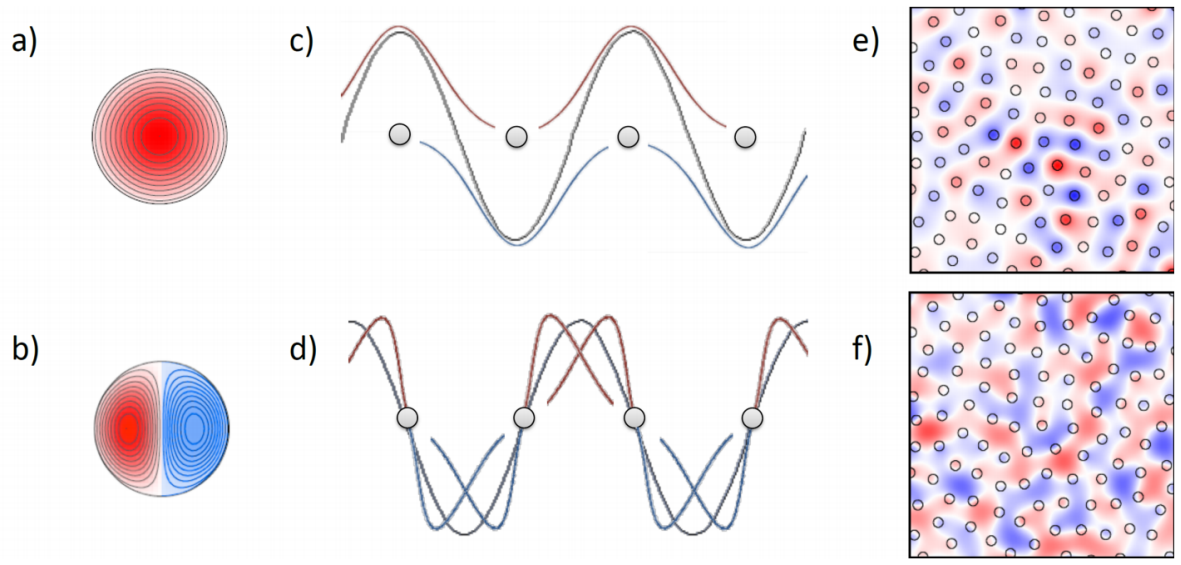

Figure 2.8: The relationship between Mie resonances and their hybridisation in photonic crystals. (**a**) and (**b**) show the zeroth and first order Mie resonances, characterised by having no node and a single node respectively. (**c**) and (**d**) show the hybridisation of individual modes to form extended hybrid modes. The red and blue lines represent the individual modes whose absolute amplitude decays inversely with the distance from the centre of the scatterer. The black lines represent the hybrid mode, where those formed from the zeroth and first order Mie resonances are concentrated in the high dielectric region and low dielectric region respectively, just as was the case for Bragg scattering picture. (**e**) and (**f**) then show example eigenmodes for a disordered 2D photonic crystal below and above the PBG, where the mode below the PBG has zero nodes inside the high dielectric material, whereas the mode above does. Adapted from Ref. [103]

Elongated Triblock Patchy Particles: Building Blocks for Photonic Crystals

3.1 Introduction

In this thesis we intended to build on the foundation that has been laid for colloidal open crystals self-assembled from spherical triblock patchy (STP) particles.[66,67] STP particles are considered to be potential building blocks for photonic crystals, having been shown to assemble into the cubic diamond[66] and tetrastack[58,59,64,65] structures. In the present body of work, we investigated the crystal structures formed by elongated triblock patchy (ETP) particles, as well as the photonic properties of these structures. The lowest frequency modes of a photonic crystal strongly confine their electrical energy to high dielectric regions; and so, structures composed of dielectric particles that have a thin vein-like shape (such as the ETP particles) provide narrow "highways" along which the electric field lines can traverse. As a result, the electrical energy of the eigenmodes for the lowest bands is strongly confined to the high dielectric region, whereas the upper bands are moved to higher frequency as the particles will be unable to accommodate multiple orthogonal modes.[104] Therefore, we would expect the photonic properties of the structures formed by the ETP particles to be superior to their spherical counterparts.

This section is outlined as follows: we present the model for the elongated particles considered here, followed by the results of this thesis. Crystal structure prediction was performed for the ETP particles in order to see what structures the particles could be expected to assemble into. The photonic band structure of these crystals were then calculated and compared to their spherical counterparts. Finally we performed virtual move Monte Carlo simulations in order to explore hierarchical self-assembly pathways for designer ETP particles into the crystal structures of interest.

3.2 Elongated Triblock Patchy Model

Here we outline the pair potential used to describe the interaction between the ETP particles. The interaction between the cores is considered to be that of soft repulsive spherocylinders (SRS), modelled by the truncated and shifted Kihara potential. The liquid crystal phases of these particles have been thoroughly studied in Refs. [105–107]. The diameter of the spherocylinder is denoted by σ and its length by L, the aspect ratio of the spherocylinder is then $L^* = L/\sigma$. Each ETP particle has two attractive patches, one on each cap, which we denote as A and B, where patch A has a half angle of α and patch B has a half angle of β. The widths of the two patches can vary independently, as can their attractive strengths. A schematic illustration of the ETP particles, as modelled here, is shown in , as shown in **Figure** 3.1.

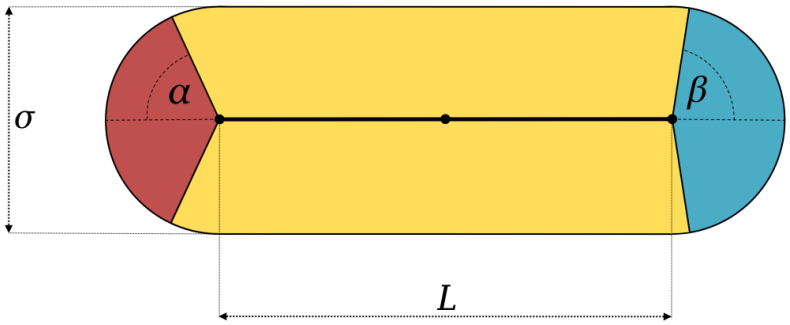

Figure 3.1: Two-dimensional representation of the ETP model, where L is the length of the line segment (thick black line) that connects the centers of the spherocylinder caps, and σ is the diameter of the spherocylinder. Attractive patches are placed at each cap (represented by the red and blue segments), that can possess varying strengths and widths. The half-widths of the patches are denoted by α and β.

The truncated and shifted Kihara potential is given by:

$$U^{\mathrm{SRS}}(d_{ij}) = \begin{cases} 4\varepsilon\left[\left(\dfrac{\sigma}{d_{ij}}\right)^{12} - \left(\dfrac{\sigma}{d_{ij}}\right)^{6} + \dfrac{1}{4}\right] & \text{if} \quad d_{ij} < \sqrt[6]{2}\sigma \\ 0 & \text{otherwise} \end{cases} \tag{3.1}$$

where d_{ij} represents the shortest distance between spherocylinders i and j, defined as the minimum distance between the line segments of the spherocylinders.[108] As a representative example, **Figure** 3.2 plots the Kihara potential for four relative orientations for a pair of spherocylinders.

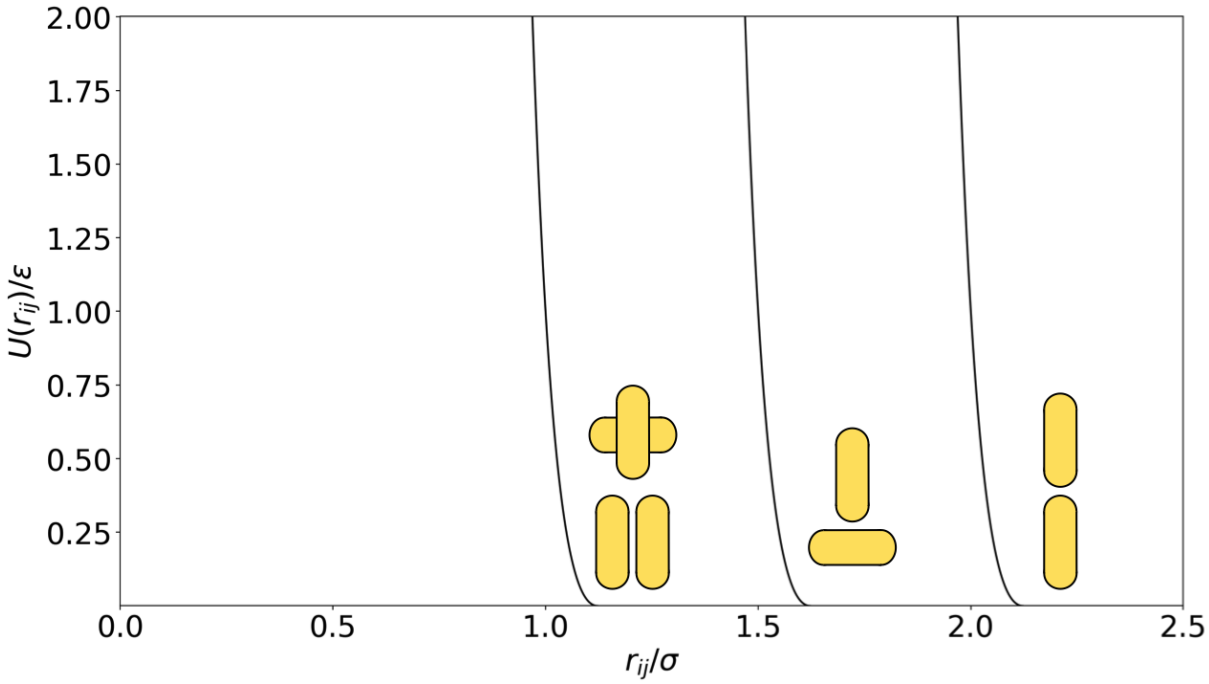

Figure 3.2: The soft repulsive spherocylinder pair potential (also known as the Kihara potential), as a function of the centre-to-centre separation of the particles, r_{ij}, for two particles with fixed relative orientations. The pair potential shown is for spherocylinders with $L = \sigma = 1$, the four relative configurations shown on the plot are isoenergetic as the shortest distance, d_{ij}, between the spherocylinders in all four configurations is the same.

As stated earlier, previous studies on spherical patchy particles have widely employed the Kern-Frenkel model. For our designer patchy particles, the patch-patch interactions are modelled in a similar spirit, but are made continuous by the use of the functional form given in Eqns. (3.2)-(3.4), as prescribed in Ref. [109], and more recently used in Ref. [66]. In this continuous patchy model the distance dependence of the patch-patch interactions is given by:

$$U(r_{ab}) = \begin{cases} -\epsilon_{ab} & \text{if } (r_{ab} - \delta) < 0 \\ -\frac{1}{2}\epsilon_{ab}[1 + \cos(\pi(r_{ab} - \delta)s)] & \text{if } 0 \leq (r_{ab} - \delta) \leq s^{-1} \\ 0 & \text{otherwise} \end{cases} \tag{3.2}$$

where r_{ab} is the distance between patch a and patch b, and δ is the largest separation at which the attraction between patch a and patch b is at its strongest. s controls the range at which the attraction decreases to zero. ϵ_{ab} is the depth of the potential due to the patch a-patch b

interaction, and determined by the geometric mean $\sqrt{\epsilon_{aa}\epsilon_{bb}}$. In this continuous version of the Kern-Frenkel model potential is modulated by the angular term, which is given by:

$$f_{kl}(\hat{\mathbf{r}}_{ab}, \hat{\mathbf{u}}_a, \hat{\mathbf{u}}_b) = \frac{1}{4}(1 + \Phi_a)(1 + \Phi_b) \tag{3.3}$$

where, $\hat{\mathbf{u}}_a$ is the unit vector describing the orientation of patch a with half angle θ, and

$$\Phi_a = \begin{cases} -1 & \text{if } (-\hat{\mathbf{r}}_{ab} \cdot \hat{\mathbf{u}}_a) < \cos\theta \\ -\cos\left(\dfrac{\pi[-\hat{\mathbf{r}}_{ab} \cdot \hat{\mathbf{u}}_a - \cos\theta]}{1 - \cos\theta}\right) & \text{otherwise} \end{cases} \tag{3.4}$$

The interaction between two ETP particles is then given by:

$$U_{ij}^{ETP}(\mathbf{r}_{ij}, \hat{\mathbf{u}}_i, \hat{\mathbf{u}}_j) = U^{SRS}(\mathbf{r}_{ij}, \hat{\mathbf{u}}_i, \hat{\mathbf{u}}_j) + \sum_{a=1}^{2}\sum_{b=1}^{2} U(r_{ab}) \cdot f_{ab}(\hat{\mathbf{r}}_{ab}, \hat{\mathbf{u}}_a, \hat{\mathbf{u}}_b) \tag{3.5}$$

where, r_{ij} and r_{ab} represent the centre-to-centre distance between the two ETP particles and patches a and b respectively; $\hat{\mathbf{u}}_i$ represents the orientation of particle i, which we define as the unit vector parallel to the line segment of the ETP particle in the direction of patch A. $\hat{\mathbf{u}}_a$ represents the orientation patch a, if $a = A$ then $\hat{\mathbf{u}}_a = \hat{\mathbf{u}}_i$, whereas if $a = B$ then $\hat{\mathbf{u}}_a = -\hat{\mathbf{u}}_i$. Therefore, we can define the reference positions of the rigid-body sites for an ETP particle of length L as:

$$\mathbf{r}_A^z = (0, 0, L/2) \qquad \mathbf{r}_B^z = (0, 0, -L/2)$$

The inter-patch vector between patches a and b on spherocylinders i and j is then given by:

$$\mathbf{r}_{ab} = \mathbf{r}_{ij} + (\boldsymbol{R}_a \cdot \mathbf{r}_a^z - \boldsymbol{R}_b \cdot \mathbf{r}_b^z) \tag{3.6}$$

where $\boldsymbol{R}_a$ represents the 3×3 rotation matrix for patch a on particle i. The particles considered in this thesis can be envisaged as an extension of the Janus matchstick particles studied in Refs. [69] and [70], with an additional patch. The pair potential for ETP particles (of arbitrary geometry) and its derivatives were implemented into `GlOSP`. These were then adapted in order to calculate the lattice energy of the ETP particle system.

The shortest distance is a function of the center-to-center inter-particle distance between spherocylinders i and j, $\mathbf{r}_{ij}$, the unit vectors describing their respective orientations, $\hat{\mathbf{u}}_i$ and $\hat{\mathbf{u}}_j$, and the length, L; the derivatives of the potential energy function were therefore taken accordingly. The $\mathrm{sgn}(x, y)$ function returns the value of x with the sign of y.

Algorithm 2: Shortest Distance Between Two Line Segments

Input : $(\mathbf{r}_{ij}, \hat{\mathbf{u}}_i, \hat{\mathbf{u}}_j, L)$

$p = \mathbf{r}_{ij} \cdot \hat{\mathbf{u}}_i, \quad q = \mathbf{r}_{ij} \cdot \hat{\mathbf{u}}_j, \quad \mathrm{u} = \hat{\mathbf{u}}_i \cdot \hat{\mathbf{u}}_j$

$l = L/2$, $c = 1 - \mathrm{u}^2$

if $c < \delta$ **then**

  if $p \neq 0$ **then**

    $\lambda_i = \mathrm{sgn}(l, \mathrm{p}), \quad \lambda_j = \lambda_i \mathrm{u} - \mathrm{q}$

    if$(|\lambda_j| > l) \quad \lambda_j = \mathrm{sgn}(l, \lambda_j)$

  else

    $\lambda_i = 0, \quad \lambda_j = 0$

  end

else

  $\lambda_i = (p - q\mathrm{u})/c, \quad \lambda_i = (p\mathrm{u} - q)/c$

  $\Lambda_i = |\lambda_i| - l, \quad \Lambda_j = |\lambda_j| - l$

  if $\Lambda_i > 0$ OR $\Lambda_j > 0$ **then**

    if $\Lambda_i > \Lambda_j$ **then**

      $\lambda_i = \mathrm{sgn}(l, \lambda_i), \quad \lambda_j = \lambda_i \mathrm{u} - q$

      if$(|\lambda_j| > l) \quad \lambda_j = \mathrm{sgn}(l, \lambda_j)$

    else

      $\lambda_j = \mathrm{sgn}(l, \lambda_j), \quad \lambda_i = \lambda_j \mathrm{u} - p$

      if$(|\lambda_i| > l) \quad \lambda_j = \mathrm{sgn}(l, \lambda_i)$

    end

  end

end

$\mathbf{d}_{ij} = \mathbf{r}_{ij} + \lambda_j \hat{\mathbf{u}}_j - \lambda_i \hat{\mathbf{u}}_i$

return $\mathbf{d}_{ij}$

3.3 Crystal Structure Prediction

Global minima on the crystal energy landscape for the ETP potential were identified using basin-hopping global optimization. The key methods described in Ref. [74] were implemented into the package `GlOSP`, a program for Global Optimization for Structure Prediction, developed in-house. Benchmarking results for the computational framework used in this thesis is provided in Appendix C. The L-BFGS algorithm was used for local minimization with 1,000,000 basin-hopping steps for unit cells containing four, six and eight ETP particles. A range of parameters were used, the aspect ratio was fixed at unity: $L^* = 1$, the patches were set to be of the same width and were in the range: $\alpha = \beta = [60° - 90°]$ and the range of patch-patch interactions was fixed at 0.2σ ($s = 5$). Simulations were set up for systems with and without a hierarchy of interaction strengths, $\epsilon_{AA} = 5$ and $\epsilon_{BB} = \{1, 5\}$, that we refer to as the AB-ETP and AA-ETP systems respectively. For all systems considered, four isoenergentic structures were found as the global minima: *cubic tetrastack* (CT), *hexagonal tetrastack* (HT), *double cubic tetrastack* (DCT) and *triple cubic tetrastack* (TCT) structures. The cubic and hexagonal tetrastack structures are similar to their spherical counterparts.

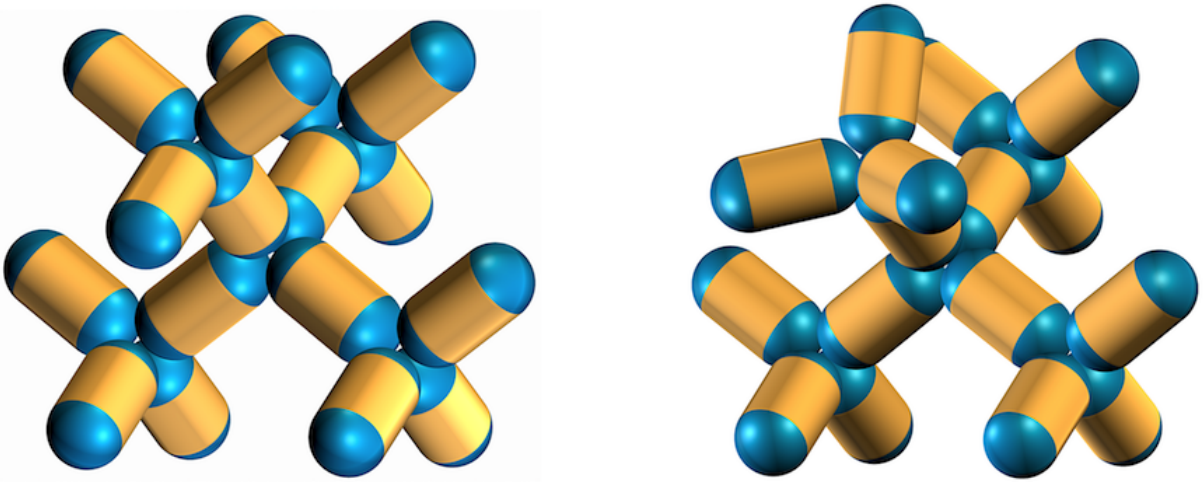

Figure 3.3: The characteristic 16 particle motif of cubic and hexagonal tetrastack can be considered as a tetrahedron of tetrahedra. Four tetrahedral units come together such that their centres are all tetrahedrally arranged, resulting in a fifth central tetrahedron. (**left**) In the cubic polymorph the tetrahedral clusters are all orientated so that they are staggered relative to the central tetrahedron. (**right**) In the hexagonal polymorph only three of the tetrahedral clusters are staggered relative to the central tetrahedron, with the forth eclipsed.

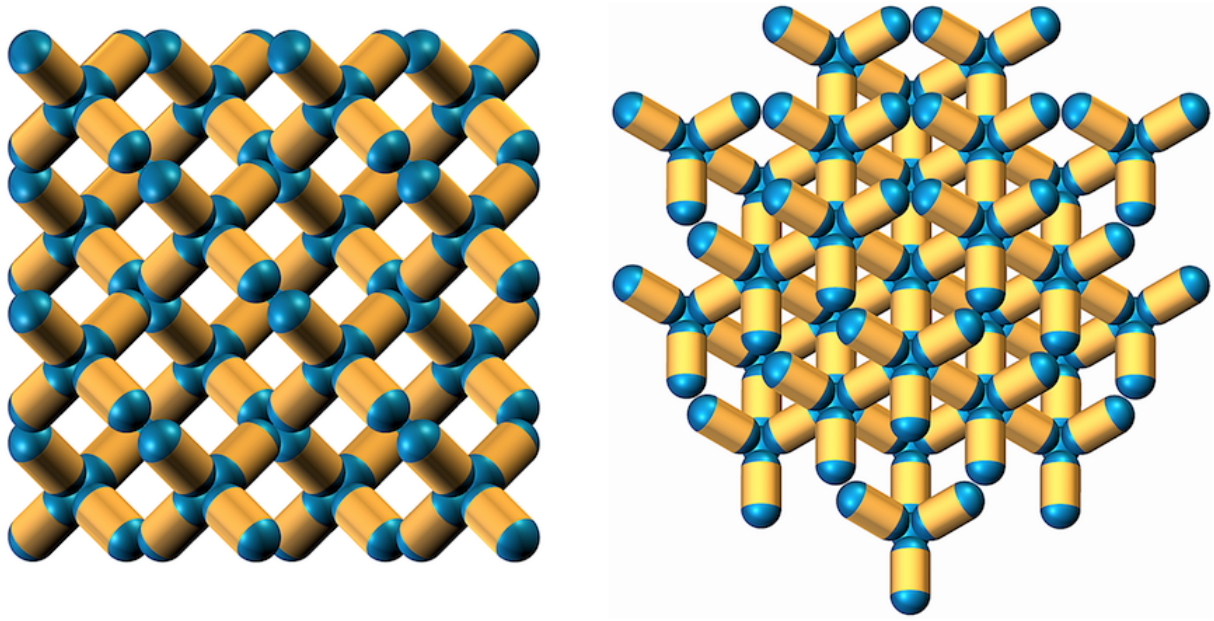

Figure 3.4: Two views of the **cubic tetrastack** structure, the left image highlights the cubic symmetry of the structure, whereas the right image showcases the ABC stacking of staggered Kagome planes in cubic tetrastack. From these two images it is clear how the structure is composed of corner sharing tetrahedra that are all staggered relative to one another.

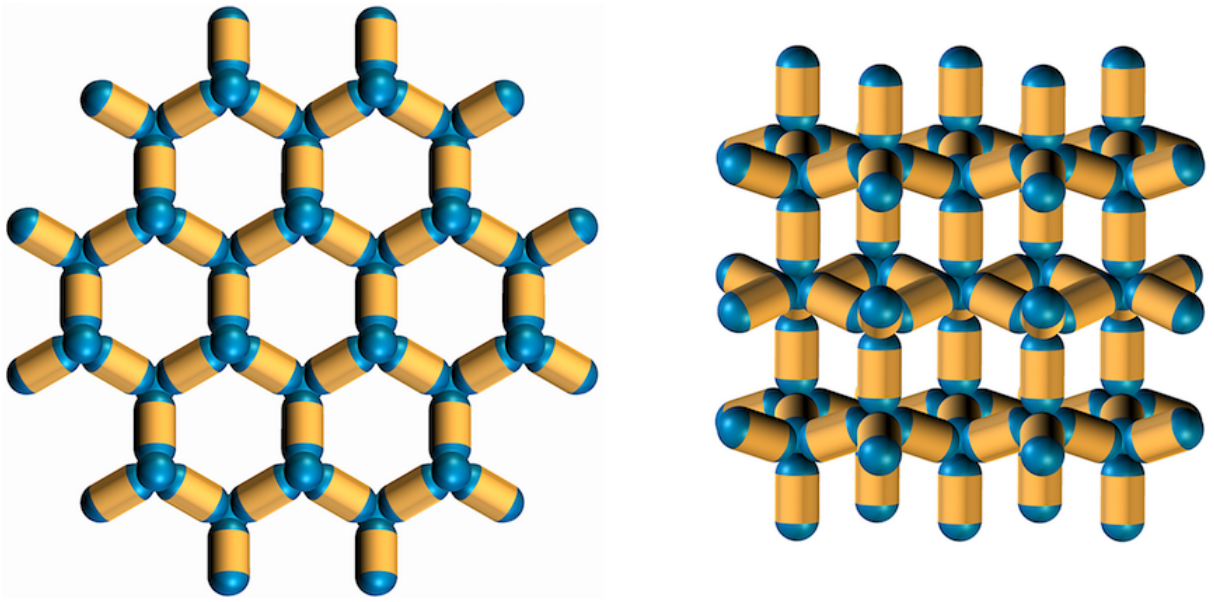

Figure 3.5: Two views of the **hexagonal tetrastack** structure, the left image is the view along the $\mathbf{a}_3$ and highlights the hexagonal symmetry of the structure, as well as showcasing the eclipsed Kagome planes of the hexagonal polymorph. The right image displays the AB stacking of the Kagome planes in hexagonal tetrastack.

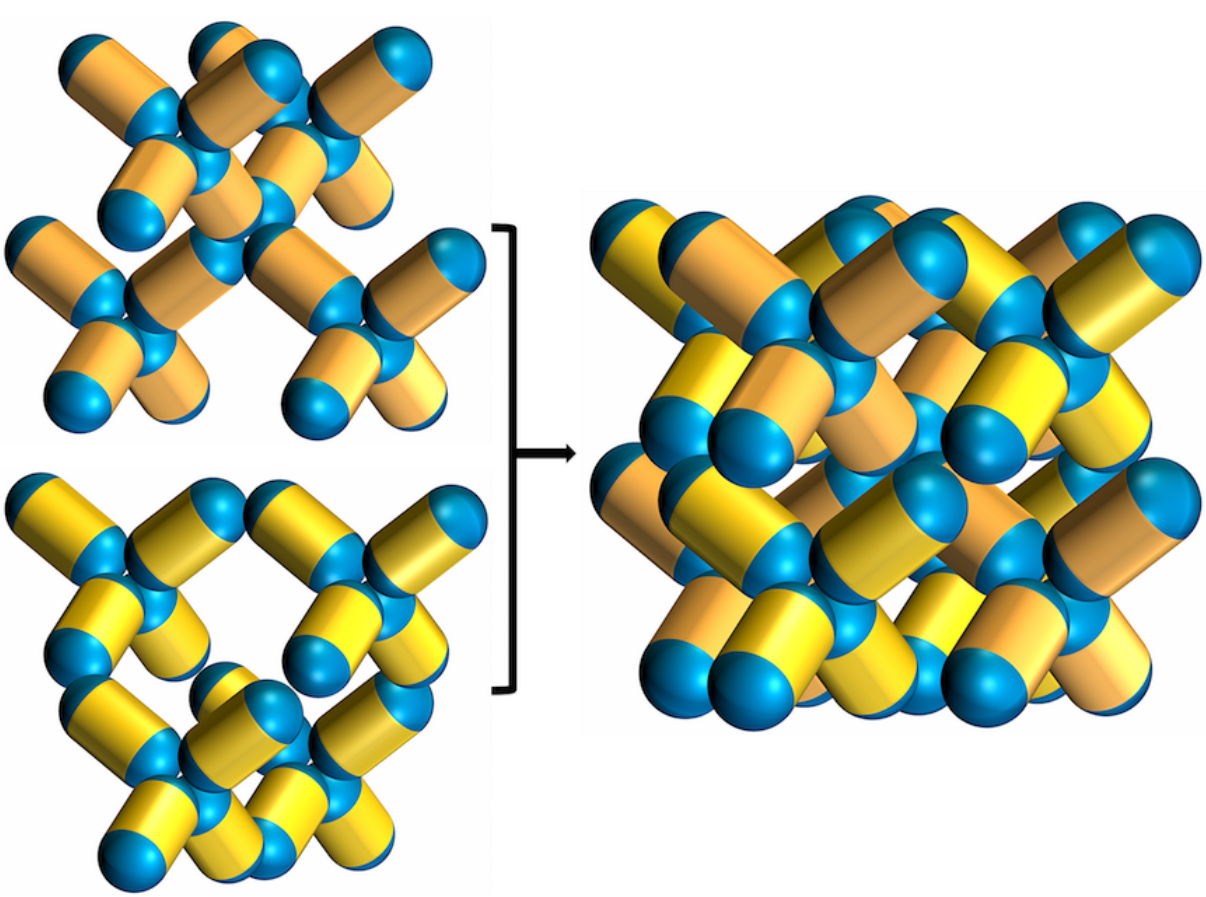

Figure 3.6: Two conventional unit cells of the CT structure are shown on the left, the particles are coloured differently simply to highlight the fact that there are two seperate CT networks. The origin of the CT structure is shifted by half a cell length between the two views, so that if they are then superimposed on one another the DCT structure is formed, as shown on the right.

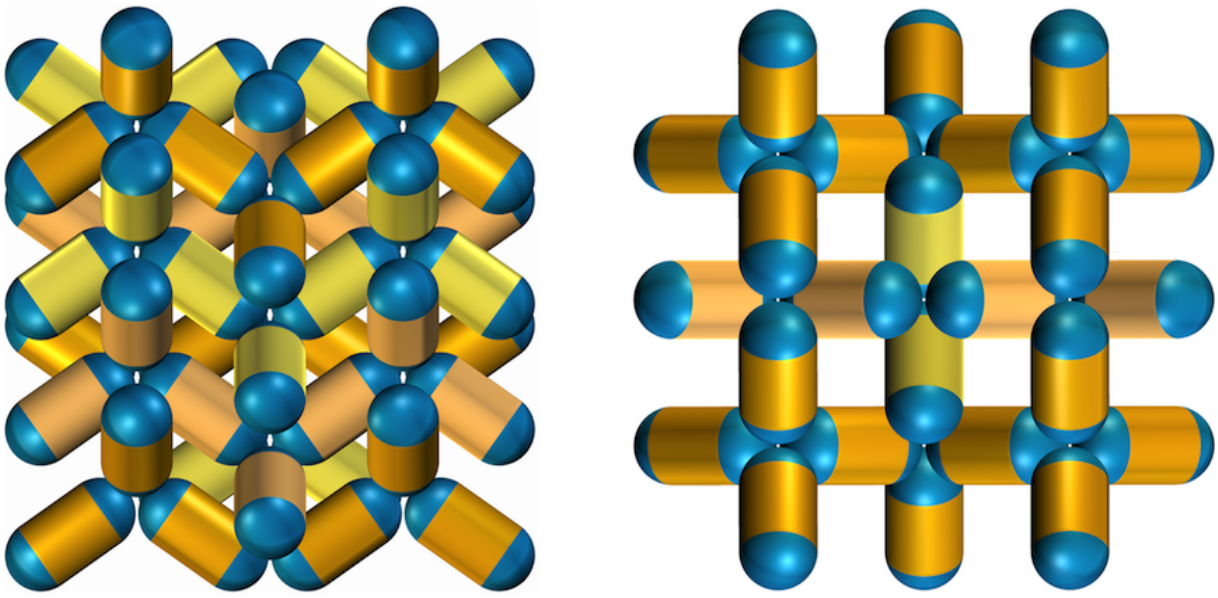

Figure 3.7: Images of the TCT structure showcasing the "close-packed" nature of the structure.

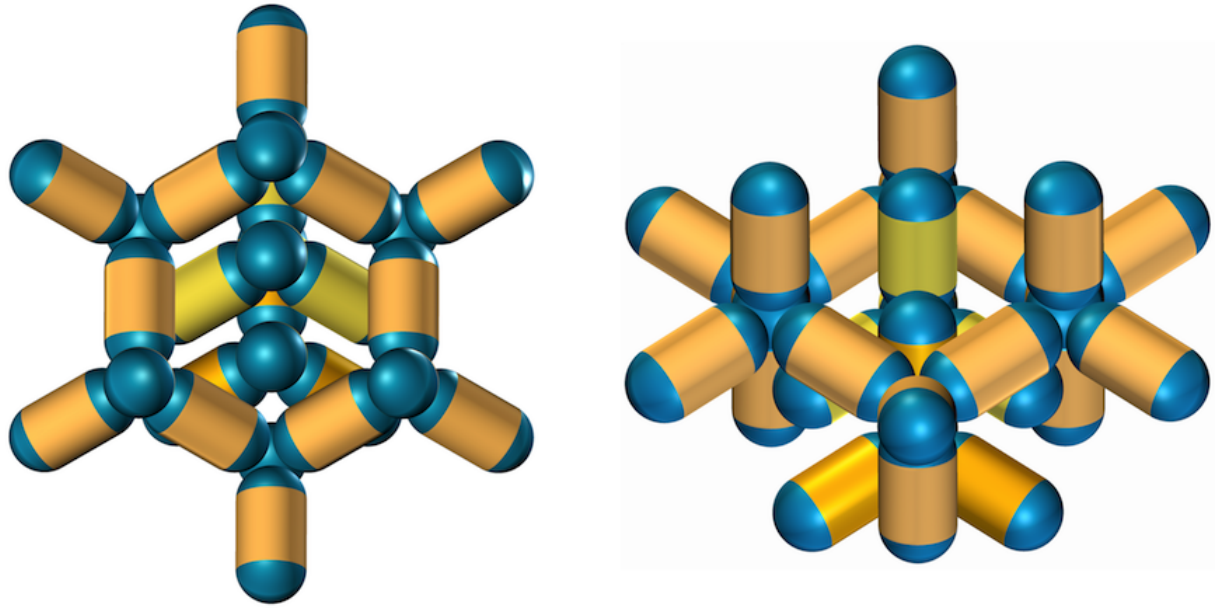

Figure 3.8: Each of the hexagonal rings that form the pores of the CT structure is wide enough to accommodate two vertically aligned particles. If these two vertically aligned particles are associated with separate CT structures, the result is the TCT structure.

The DCT and TCT structures are made up of two and three interpenetrating CT structures, respectively. The unit cells of CT and DCT both contain a single tetrahedron, with the difference between the two structures arising due to DCT possessing a primitive simple cubic unit cell, whereas CT has a primitive fcc unit cell. The length of the unit cell vectors for DCT is half of the length of the conventional unit cell vectors for CT. However, the centres of the ETP particles in DCT sit on fcc lattice points, the fcc face should be recognisable in **Figure** 3.6. Clearly, due to the different orientations of the particles it is not possible to define the structure as an fcc lattice with a one-particle motif. In addition to the DCT structrure, we also found the TCT structure, which is built up from three interpenetrating CT structures. However, unlike the CT and DCT structures, TCT does not have a cubic unit cell. Instead, the TCT structure has a body-centered tetragonal unit cell.

Each ETP particle forms a total of six bonds, three on each patch. As previously stated changing the parameters of the pair-potential does not change the global minimum structures, and so the presence of a hierarchy of interaction strengths does not change the global minimum structures observed. However, each particle in the AB system maximises the number of strong-strong patch interactions. Therefore, each particle in the AB systems has three strong-strong bonds and three weak-weak bonds. In the AA system, all of the bond lengths are identical and so the crystal structures possess an inversion centre. This changes in the AB system, as the bonds formed by weak-weak patches are slightly longer than those formed by strong-strong patches. The result is that the crystal structures lose their inversion symmetry; which in turn alters the spacegroup of the structures. The change in the spacegroup is best explained in terms of the tetrahedral vacancies of the crystal structures. If we imagine a pseudo-particle, whose volume is equal to that of the vacancy, is centred on each of the tetrahedral vacancies in CT, they will collectively form cubic diamond. In the AA system all of these pseudo-particles are of the same volume. However, in the AB system the strong-strong pseudo-particles have a smaller volume than the weak-weak pseudo-particles. As a result the AA-CT structure has the same symmetry as the cubic diamond structure – they both belong to the Fd-3m space group, whereas the AB-CT structure has the same symmetry as the zinc blende structure. This explanation can then be extended to the other tetrastack structures, with the tetrahedral vacancies in the AB-HT structure forming a wurtzite structure.

Structure	*Spacegroup*	
	$\epsilon_{BB} = 1$	$\epsilon_{BB} = 5$
CT	F-43m	Fd-3m
HT	$P6_3mc$	$P6_3/mmc$
DCT	P-43m	Pn-3m
TCT	I-4m2	$I4_1/amd$

Table 3.1: The spacegroups of the global minimum structures for the ETP system where $L = \sigma = 1$, $\epsilon_{AA} = 5$ and $\alpha = \beta = 85°$. In the presence of a hierarchy of interaction strengths, (i.e., when $\epsilon_{BB} = 1$) the structures do not possess an inversion center, which is reflected by the change in the spacegroup of the structures.

These results are not wholly unexpected, in fact it is exactly what one would have expected given the previous studies on STP particles. A sphere can be considered as a spherocylinder with $L^* = 0$, and so the patch-patch interactions are exactly the same as those for a spherocylinder with $L^* = 1$. Clearly, the local order of the structures formed by the ETP particles is governed by the geometry of the patches, just as is the case for STP particles. However, unlike their spherical counterparts, the ETP particles are is able to form interpenetrating structures. Therefore, by introducing the shape anisotropy we have opened up the possibility of forming structures that are inaccessible to the STP particles. The DCT and TCT structures are reminiscent of the close-packed tetrahedra reported by Conway and Torquato in Ref. [110]. However, it is not immediately obvious as to why interpenetrating structures for HT were not found. This remains to be clearly understood; however, it is most likely because the structure cannot be formed by simply changing the shape of the unit cell. By considering **Figure** 3.4 it should be clear that for double hexagonal tetrastack (DHT), the two interpenetrating structures will be related by a translation *and* an inversion. Given that all of the structures are isoenergetic, we can expect this system to suffer from the same issue of polymorphism that plagues their spherical counterparts. Additionally, there is the added complication of the interpenetrating structures with the ETP particles. We would also expect the number of interpenetrating structures that can be accomodated to increase as the aspect ratio of the ETP particles increases, due to the wider hexagonal rings that would be formed.

3.4 Photonic Band Structure Calculations

Having found the potential crystal structures that can be assembled from ETP particles, we are interested in identifying whether any of these structures exhibit a complete photonic band gap. The photonic properties of the structures found from global optimisation are investigated using the freely available `MIT Photonic-Bands` (`MPB`) software package, version 1.5.[89] The `MPB` software computes fully vectorial eigenmodes of Maxwell's equations with periodic boundary conditions by a preconditioned conjugate-gradient minimization of the block Rayleigh quotient in a plane wave basis. The `MPB` takes the fractional coordinates, geometry and dielectric constant of the particles, and the primitive lattice basis of the crystal structure as input. The `GlOSP` package outputs the optimised centers of mass and orientations of the particles with unit cell parameters that do not necessarily correspond to the primitive or conventional unit cell. Therefore, in order to set up the photonic band structure calculations the minima found from global optimisation must first be converted to a primitive lattice basis. We use the freely available `spglib`[111] package in order to to standardise the unit cell parameters extracted from `GlOSP` into primitive cell parameters and extract the corresponding fractional coordinates of the particles. However, neither `MPB` nor `spglib` have a standard spherocylinder geometric object. To work around this issue we deconstruct each spherocylinder into a rigid body made up of three components: a cylinder and two hemispherical caps. We use `spglib` to extract primitive lattice basis and the fractional coordinates of these sites. Then the orientation of the ETP particles in fractional space can be calculated by computing the unit vector that connects the center of mass of each ETP particle with one of the hemispherical cap sites. The spherocylinders can then be defined in `MPB` using two cylinders and two spheres. Two dielectric spheres are positioned at the hemisphere sites, then a cylinder of the correct length and orientation is positioned at the center of mass and defined to have a dielectric constant of *nothing*. This has the effect of "punching a hole" in the dielectric spheres to convert them into hemispheres. Finally a second dielectric cylinder, of the same length and orientation is defined in order to complete the spherocylinder.

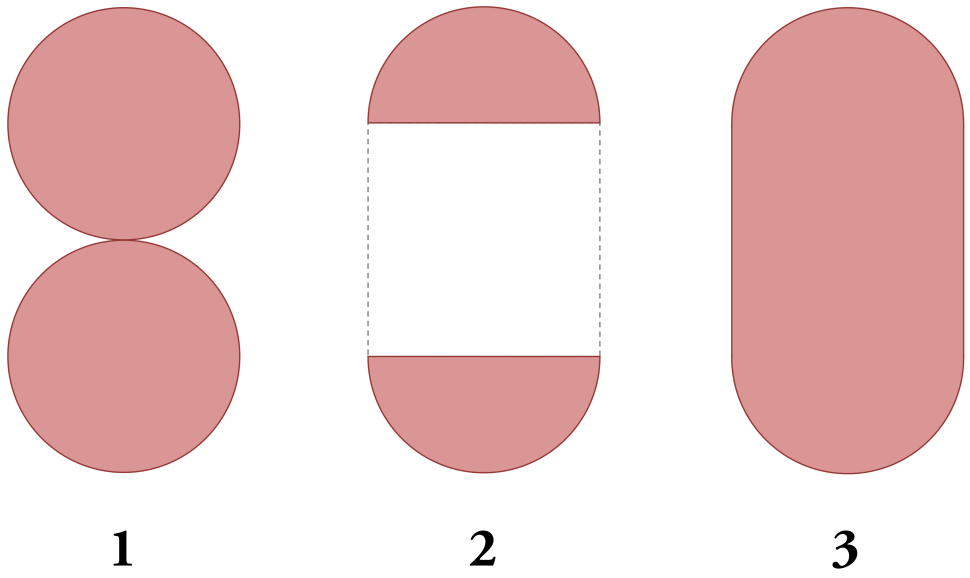

Figure 3.9: Cartoon depicting the geometric objects used to define each of the ETP particles within the `MPB` package. **(1)** First, two dielectric spheres with a diameter of 1 and dielectric constant of 12 are defined. Each sphere is centred on one of the hemispherical sites for the ETP particle. **(2)** Next a cylinder, with the correct length and orientation, is defined. This cylinder has a dielectric constant of *nothing* and "punches a hole" in the dielectric spheres to convert them into hemispheres (see page 37 of the `MPB` manual). **(3)** Finally, a second cylinder, with the same length and orientation, is defined which connects the two hemispheres and gives the complete ETP particle.

The `MPB` package requires the user to also specify certain key parameters – *resolution*, *mesh size* and ***k**-points*. The *resolution* defines the number of spatial grid points that are used to discretize the unit cell. At each grid point the dielectric constant, and its inverse, are averaged over a uniform mesh extending halfway to the neighboring grid points. The mesh resolution is controlled by the *mesh size* variable. Finally, the ***k**-points* variable defines the set of wavevectors for which the eigenmodes and eigenfrequencies will be determined. We choose the wavevectors in such a way that they form a continuous path along the IBZ of each crystal, and so the patch varies depending on the symmetry of the crystal structure. We use `spglib` to determine the spacegroup of the crystal structures, then use Ref. [112] in order to choose the correct high symmetry points for each lattice and define the correct path along the edge of the IBZ. The pipeline of `GlOSP` → `spglib` → `MPB` was benchmarked using the inverse opal structures and cubic tetrastack with spherical particles, these are shown in **Appendix** D.

Following the example of previous studies, we consider our ETP particles to be composed of silicon, $\varepsilon = 12$, and are embedded within a low-index host material (air, $\varepsilon_{air} = 1$).[21,63,113,114] The dielectric function for all of the structures were visualised to ensure that `MPB` was correctly drawing the ETP particles, and that the structures had the correct periodicity. The dielectric functions of the CT and HT structures are shown in **Figure 3.10**.

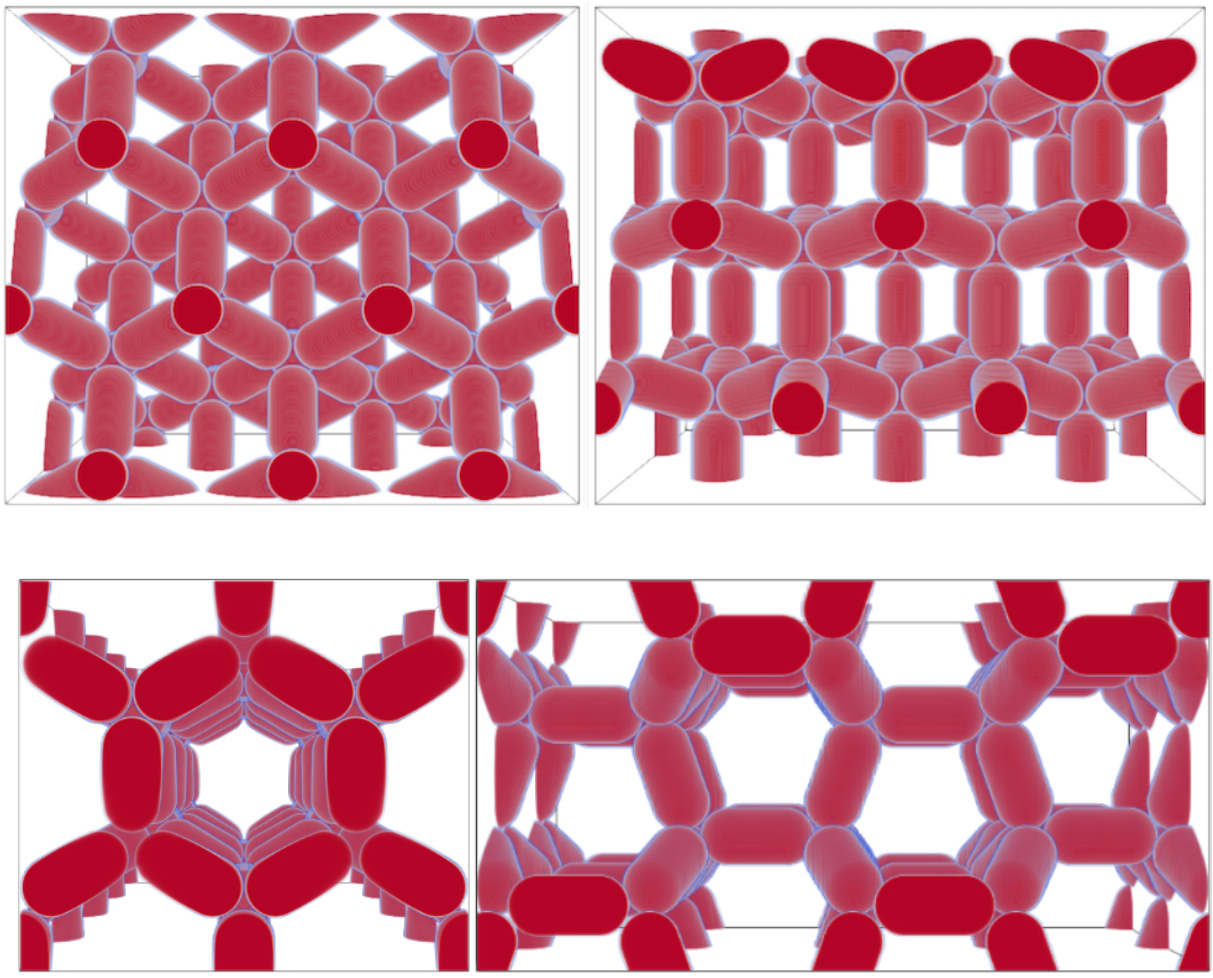

Figure 3.10: Visualisation of the dielectric function for CT (**top**) and HT (**bottom**) using a *resolution* of 128 and a *mesh size* of 50.

The photonic band structures for the CT, HT, DCT and TCT crystals are shown in **Figures** 3.14, 3.16, 3.11 and 3.13, respectively. Here the frequencies of both band structures are given in the reduced units of: $\omega^* = \omega a/2\pi c$ to allow for a direct comparison of the CT and HT band structures; where, a is the edge length of the CT conventional unit cell and c is the vacuum speed of light.

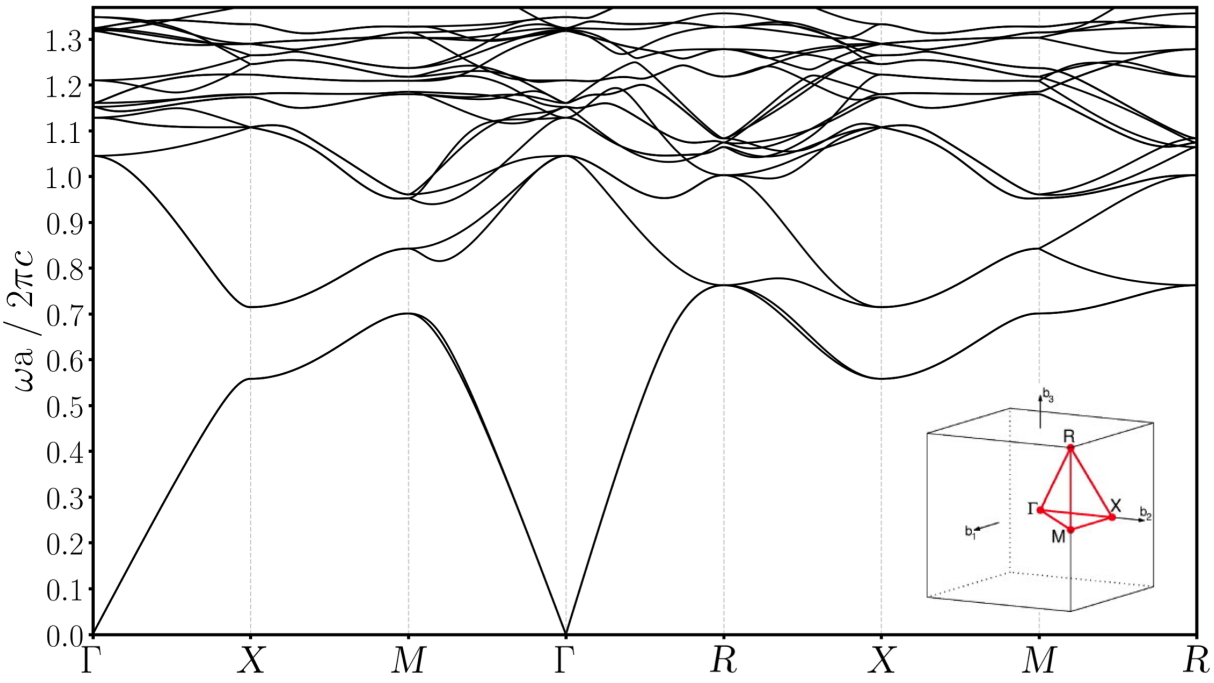

Figure 3.11: The first 25 bands from the photonic band diagram for the DCT structure.

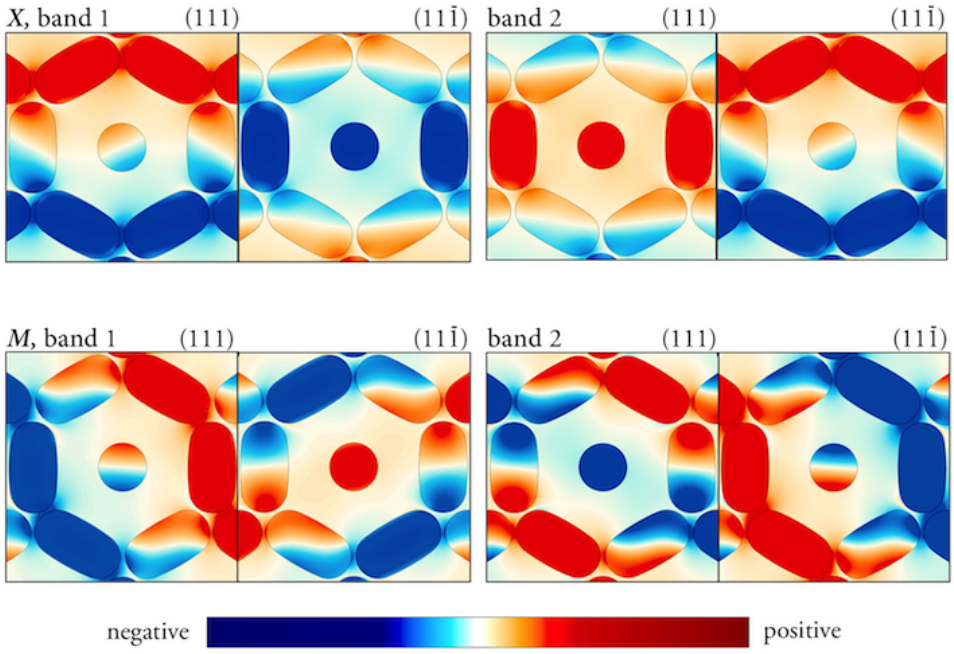

Figure 3.12: Planes of the displacement field of the DCT structure for the first and second bands at the M-points. The (111) and (11$\bar{1}$) planes are shown, where the two planes represent a Kagome plane from different interpenetrating structures. Focusing on the 1st band we see that the two interpenetrating structures have different internal field patterns. Then if we look at the 2nd band we see that the field patterns have switched between the two interpenetrating structures.

Neither DCT or TCT display a complete PBG, whereas the CT and HT structures do. Therefore, we focus mainly on the latter structures in this section. An interesting observation; however, is the origin of the degenerate states for the first four bands of DCT at the Γ, X and M-points. **Figure** 3.12 shows slices of the displacement field for the first and second bands of the DCT band structure at the M-point, where each slice shows the Kagome plane of one of the interpenetrating structures. Focusing on the first band (the left side of **Figure** 3.12), we see that the two interpenetrating structures have different internal field patterns, that also resemble those shown for the first two bands of CT. Then if we look at the second band we see that the field patterns have switched between the two interpenetrating structures resulting in a pair of degenerate states.

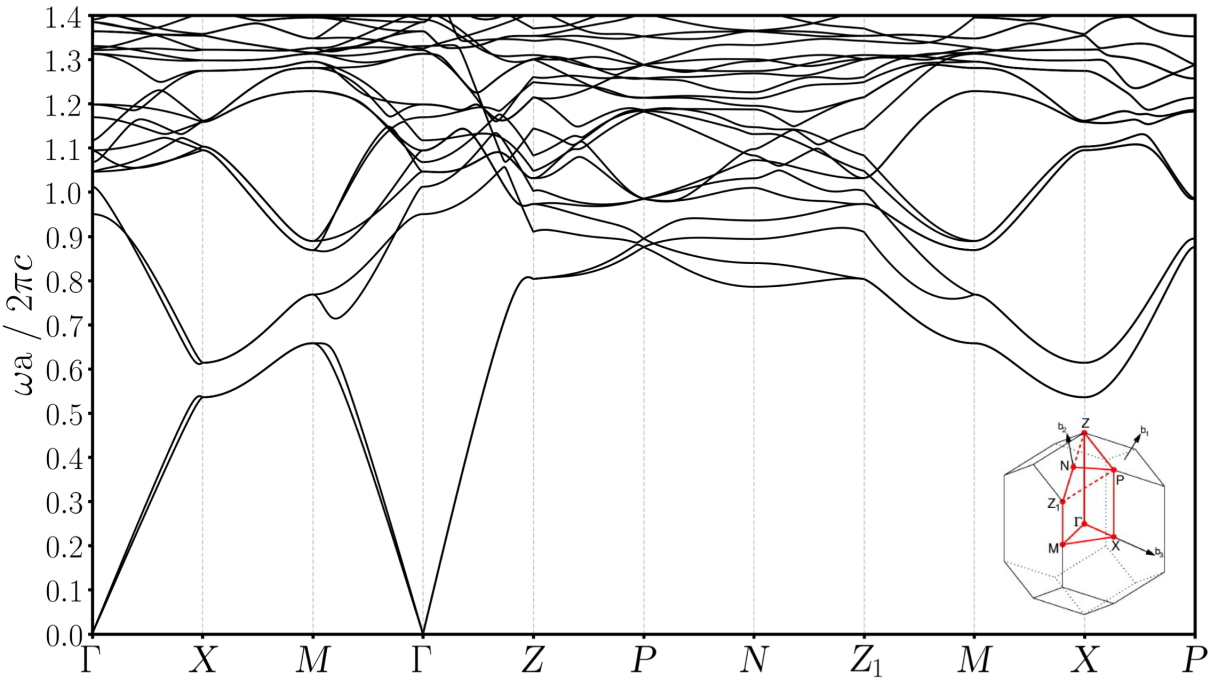

Figure 3.13: The first 25 bands from the photonic band diagram for the TCT structure.

The CT structure possesses a complete PBG between the 2nd and 3rd bands, with a band gap–midgap ratio of $\Delta\omega^*/\omega_m^* = 18.1\%$. Surprisingly, the HT structure also possesses a complete PBG between the 4th and 5th bands, with a band gap–midgap ratio of $\Delta\omega^*/\omega_m^* = 7.45\%$. Due to the lower symmetry of the hexagonal Brillouin zone, the band structure of HT has, approximately, twice as many bands in a given frequency range than CT. This in turn leads to the narrower band gap of the HT structure. A similar observation has previously been made for the electronic band structure of the cubic and hexagonal diamond phases of Si, where the extra bands in the hexagonal phase were attributed to its lower symmetry leading to fewer degenerate modes.[115]

Cubic and hexagonal tetrastack are both constructed from layers of stacked Kagome planes. Along the [111] direction of CT the planes are staggered, and along the [001] direction of HT the planes are eclipsed. Due to this common structural feature, there is a direct correspondence between some of the high symmetry points of their respective Brillouin zones. For instance, the $\Gamma \to L$ path (i.e., the [111] direction) of CT corresponds to the $\Gamma \to A$ path (i.e., the [001] direction) of the HT Brillouin zone. Additionally, the $\Gamma \to X$ path of the CT Brillouin zone can be mapped onto the $\Gamma \to M$ path of HT.[116] We, therefore, chose to compare the displacement fields, as defined in Eqn. (B.8), at the X and M points for the CT and HT structures, respectively, to see whether there is any correspondence between the field patterns of the eigenmodes. **Figures** 3.15 and 3.17 show slices of the displacement fields, taken through the (111) and (001) Kagome planes of the CT and HT structures, respectively, as these views allow for the most direct comparison of the eigenmodes of the two structures. We see that similar field patterns are exhibited by both structures. Additionally, the field patterns of the eigenmodes at the top and bottom of the band gap are the same for both structures. For there to be such a striking similarity in their field patterns, the local short-ranged order of both tetrastack structures must be a crucial factor for the opening of the band gap. Therefore, we suggest that the Mie scattering mechanism is also crucial for the opening of the band gap. Interestingly, there is a notable similarity between these eigenmodes and the internal field patterns of the Mie resonances for dielectric cylinders that were discussed in SECTION 2.3.3. If we focus on the eigenmodes of the CT structure, the first two bands display zeroth order Mie-type resonances, whereas the 3rd band clearly exhibits first order Mie-type modes as there are nodal planes that cleanly cut perpendicularly through

the ETP particles. The nodal plane along the length of the particles in the 3rd band causes some of the field amplitude to spill into the low dielectric region.[16] Therefore, the fraction of electrical energy in the high dielectric region is greatly reduced, as compared to the lower bands, resulting in the band gap (see SECTION B.2).[16,98,104] In addition to the zeroth and first order Mie-type resonances, there are modes that are not immediately identifiable as Mie-type resonances. The origin of the extra bands in the HT band structure also becomes apparent when we consider the displacement fields of the first and fourth bands at the M-point, shown in **Figure** 3.17. Both modes seem to have the same field pattern for the (001) plane; however, the field pattern for the (110) plane of the first band alternates sign only in a single direction, whereas the (110) plane of the forth band forms a checker-board pattern.

The hypothesis that the local short-ranged order of the structures is the critical factor for the opening of the band gap draws support from the so-called "photonic amorphous diamond" (PAD) that was discussed in SECTION 1.1.1.[21,22] Despite having no long-range order, the structure still has a complete PBG of 18%; additionally, its midgap frequency coincides with that of the rod-connected diamond structure.[21] This suggests that the dominant factor for the band gap in both structures is the same, meaning Bragg scattering cannot be primarily responsible for the formation of a PBG in these diamond-like structures. Rather, it must be associated with the short-ranged order of the structures.[21–23,117] The ETP-CT structure is equivalent to the rod-connected diamond structure, where each cylinder and tetrahedral junction point are replaced by a spherocylinder and a vacancy, respectively. Therefore, we would also expect the local short-ranged order of the tetrastack structures to be the key for the opening of the band gap. The dependence of the band gap–midgap ratio on the dielectric contrast is shown in **Figure** 3.18. The smallest dielectric contrast for which ETP-CT displays a complete band gap is $\varepsilon = 5.6$, similar to that of rod-connected diamond, $\varepsilon \approx 3.6$,[19,71] despite its lack of a network topology.[91]

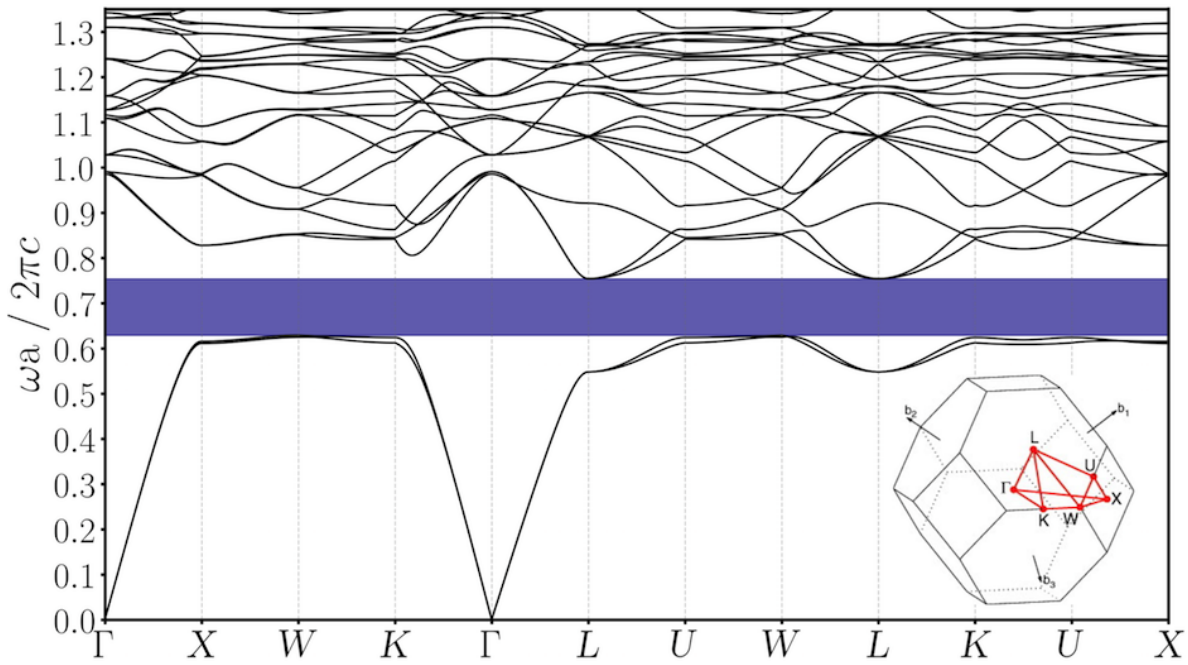

Figure 3.14: The first 25 bands from the photonic band structure for CT, with $L^* = 1$, $\alpha = \beta = 85°$, $\epsilon_{AA} = \epsilon_{BB} = 5$ and $s = 5$. A resolution of 32 and a mesh-size of 50 were used to produce this band structure. There is a complete PBG between the 2nd and 3rd bands, with $\Delta\omega^*/\omega_m^* = 18.1\%$.

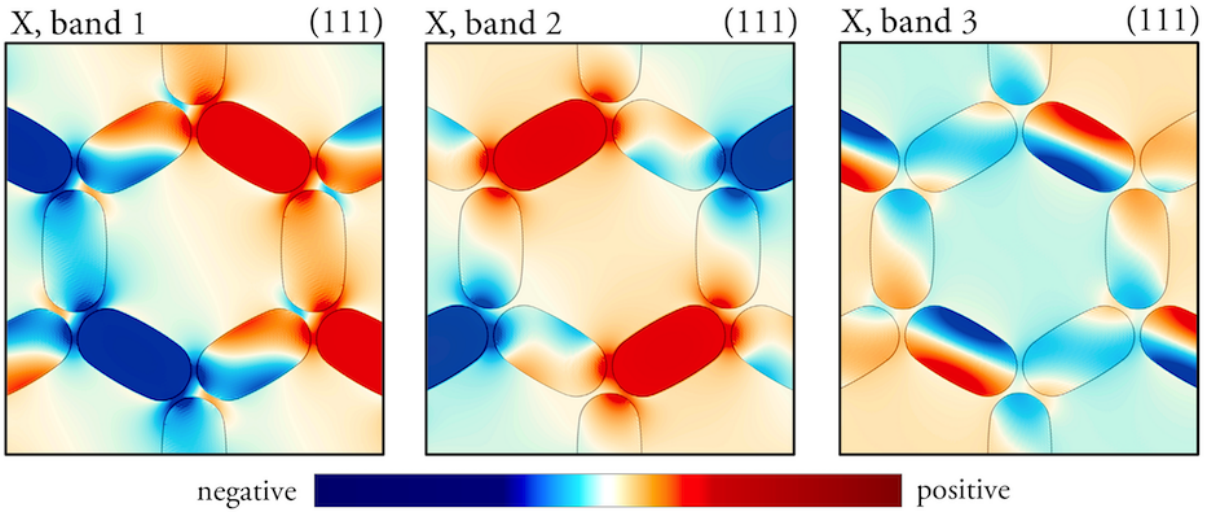

Figure 3.15: Slices of the displacement field, $\mathbf{D}(\mathbf{r}, t)$, for the first three bands of the CT structure at the X-point, where `MPB` picks a canonical phase for the eigenstates. The slices show the Kagome planes that form the (111) plane of the CT structure. It is clear that these eigenmodes are dominated by the Mie-type resonances centered on certain ETP particles. These particles in the first two bands display zeroth order Mie-type resonances, whereas in the 3rd band they resemble first order Mie-type resonances. The modes that are not immediately identifiable as Mie-type resonances, are hybrid modes made up from zeroth and first order Mie-type resonances.

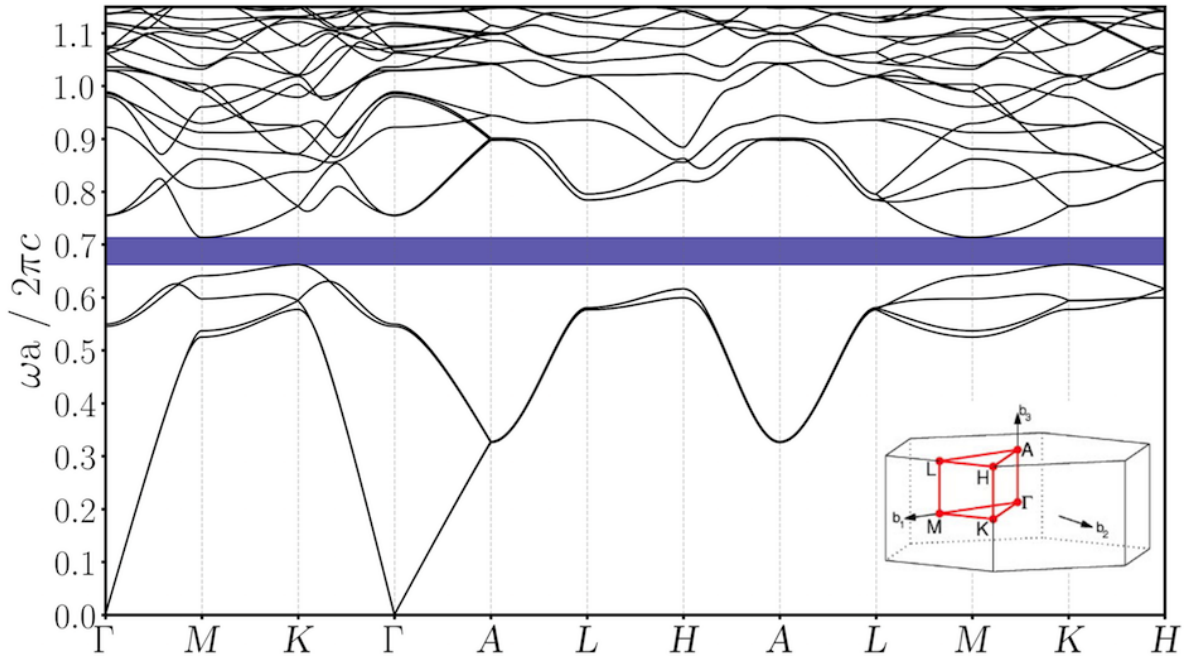

Figure 3.16: The first 25 bands from the photonic band structure for HT, with $L^* = 1$, $\alpha = \beta = 85°$, $\epsilon_{AA} = \epsilon_{BB} = 5$ and $s = 5$. There is a complete PBG between the 4th and 5th bands, with $\Delta\omega^*/\omega_m^* = 7.45\%$.

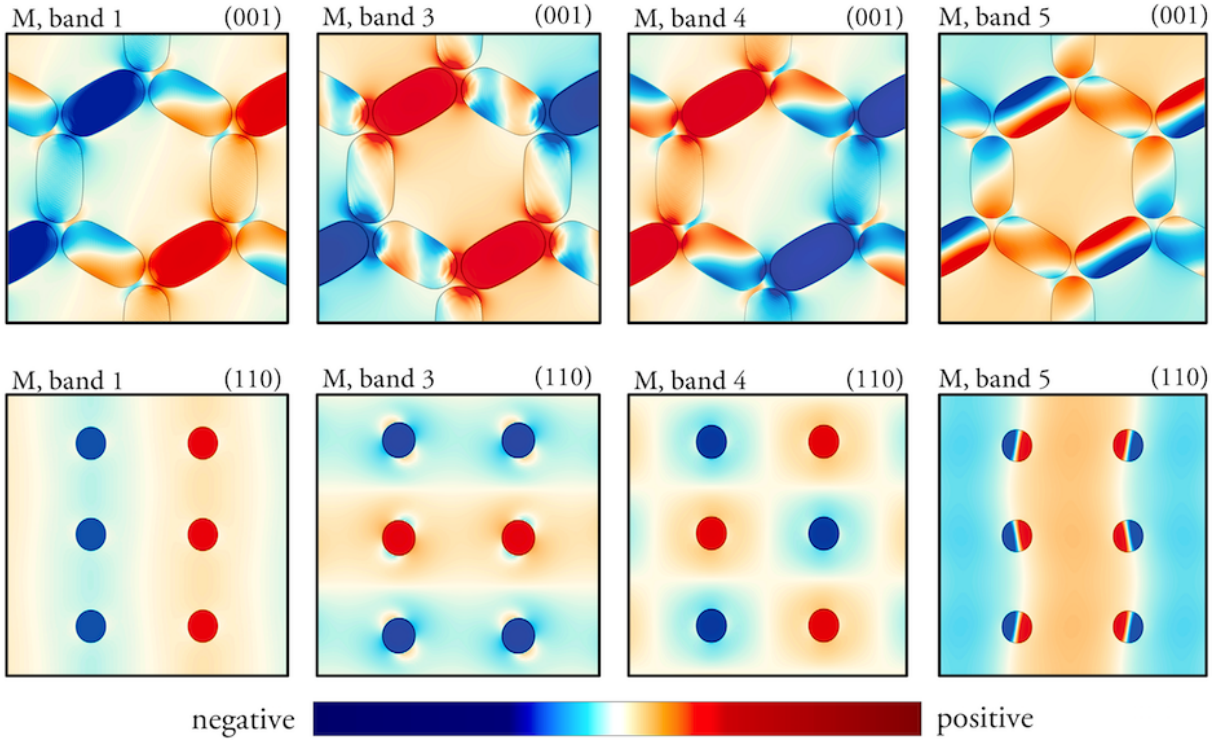

Figure 3.17: Slices of the displacement field, $\mathbf{D}(\mathbf{r}, t)$, for bands 1, 3, 4 and 5 of the HT structure at the M-point. The first and second rows depict views along the (001) and (110) planes respectively.

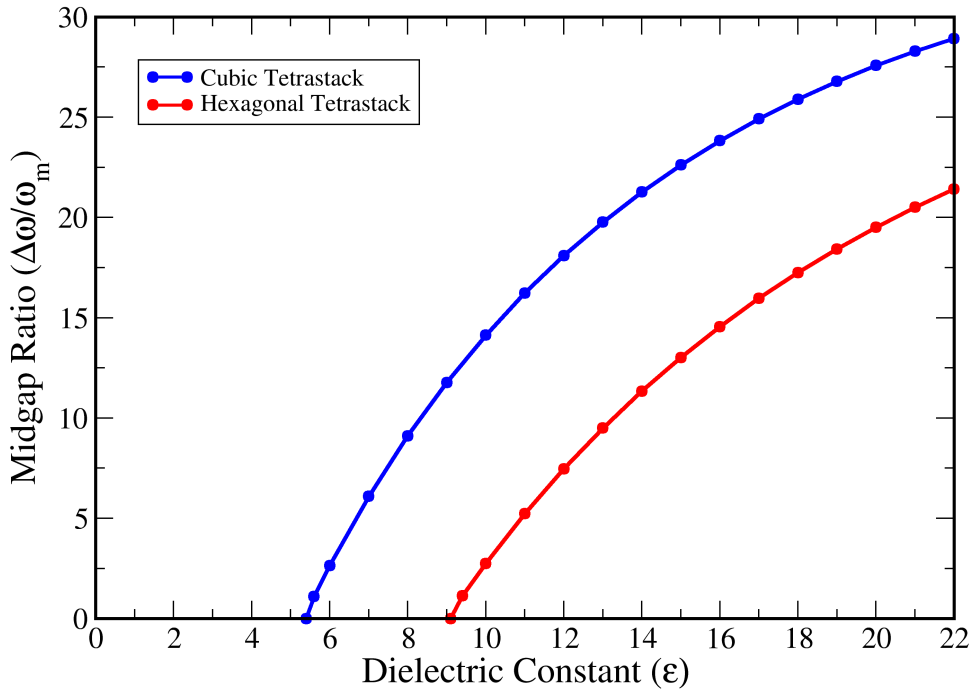

Figure 3.18: The dependence of the band gap–midgap ratio on the dielectric constant of the particles for the CT and HT structures. The lowest dielectric constant for which CT and HT exhibit a complete photonic band gap larger than 1% is 5.6 and 9.4 respectively.

At the limit of $L^* = 0$, the ETP particles are spherical and can be considered as STP particles. The STP-CT structure only has a band gap–midgap ratio of 4.2% for $\varepsilon = 12$. We have seen that the lowest two bands strongly confine their electric field energy to the high dielectric region. However, the third band has a nodal plane along the length of the particles which causes the electric field energy to spill into the low dielectric region. Increasing the length of the particles will increase the fraction of energy that spills into the high dielectric region for this third band, causing the band gap to increase in size,[16,104] as is shown to be the case in **Table** 3.2. The fraction of the electric field, for a given mode, that is contained within the high dielectric region can be quantified by the concentration factor, φ:

$$\varphi = \frac{\int_{\varepsilon_{high}} \mathrm{d}^3\mathbf{r}\ \varepsilon(\mathbf{r})|\mathbf{E}(\mathbf{r})|^2}{\int \mathrm{d}^3\mathbf{r}\ \varepsilon(\mathbf{r})|\mathbf{E}(\mathbf{r})|^2} \tag{3.7}$$

The concentration factor for the 3rd band of the CT structure approximately halves when transitioning from STP to ETP particles. The same observation is also made for the HT structure.

Point	Band	φ	
		$L^* = 0$	$L^* = 1$
X	dielectric	50%	50%
	air	45%	22%
L	dielectric	42%	44%
	air	47%	20%

Table 3.2: The concentration fraction, φ (i.e., the fraction of the time averaged electric field energy density located in the high dielectric region), as given by `MPB`, for the dielectric (band 2) and air (band 3) bands of cubic tetrastack at the X and L points, for $L^* = 0$ and $L^* = 1$.

As shown in the previous section, the symmetry of the tetrastack structures formed by the AB-ETP particles is different from those formed by the AA-ETP particles. This is expected to have an effect on the size of the band gap, and so the photonic band structures for the crystal structures formed by the AB-ETP particles were calculated. We find that the general nature of the band structures remains the same; however, the band gap decreases in size. This change arises because the particles in these crystals are not overlapping or touching, due to their repulsive interactions. Therefore, the electric field lines cannot be completely confined to the high dielectric region. As a result the electric field lines must cross through the low dielectric regions corresponding to the tetrahedral holes between the particles. The tetrahedral voids formed by the weaker patches have a slightly larger volume than those formed by the stronger patches. Therefore, more of the electric field energy leaks into the low dielectric region for the crystal structures formed by the AB-ETP particles. This is shown by the first and second rows of **Table** 3.3, where the band gap is shown to be larger for the CT structure formed by the AA-ETP particles as compared to the one formed by the AB-ETP particles since the concentration factor for the dielectric band is larger in the former. A larger band gap can be recovered for the CT structure formed by the AB-ETP particles simply by decreasing the range of the patch-patch interactions, as shown by System 3 in **Table** 3.3. By decreasing the range of the patch-patch interactions we reduce the size of the tetrahedral voids between the particles, thereby minimising the fraction of the electric field energy that leaks into the low dielectric region.

System	$\Delta\omega^*/\omega_m^*$	φ_{diel}	φ_{air}
1	18.1%	58%	22%
2	15.5%	54%	21%
3	18.8%	60%	22%

Table 3.3: The band gap–midgap ratio and concentration factors of the dielectric (second) and the air (third) band at the X point for CT are compared for three different systems with $\alpha = \beta = 85°$. **System 1**: $\epsilon_{AA} = \epsilon_{BB} = 5$ and $s = 5$, **System 2**: $\epsilon_{AA} = 5$, $\epsilon_{BB} = 1$ and $s = 5$ and **System 3**: $\epsilon_{AA} = 5$, $\epsilon_{BB} = 1$ and $s = 10$

The CT structure composed of overlapping dielectric spheres has previously been reported to possess a band gap–midgap ratio of nearly 14%.[61–63] Therefore, we have shown that the structures formed by the ETP particles have superior photonic band gap properties to their spherical counterparts; this is especially evident for the HT structure which does not have a band gap when constructed from spherical particles. The rod-connected diamond is well known to be the "champion" photonic band gap structure, with a band gap–midgap ratio of 30% between the second and third bands.[19,20,71] Although the ETP-CT structure has a narrower band gap, its allure is that it should be realisable using a bottom-up approach, unlike the rod-connected diamond structure which was fabricated by directly drilling into a block of high dielectric material.

Additionally, the Mie scattering mechanism was suggested to be the key in the formation of the band gap in the CT and HT structures. This is in line with previous observations that amorphous diamond structures also exhibit a complete band gap, with the local tetrahedral coordination of the particles suggested to be the key to the opening of a complete photonic band gap. Given that the amorphous diamond structure has a band gap, it is not unreasonable to suggest that an amorphous tetrastack structure will also display a complete photonic band gap. This is still a conjecture at this point; however, this is of particular importance as much effort has previously been placed into fabricating the perfect CT structure, but to little avail. Previous computational studies explored potential routes, using either highly complex particles or SDAs.[64,65]

3.5 Exploration of a Hierarchical Self-Assembly Strategy

Having explored what lies at the bottom of the potential energy landscape (PEL) of various small cell periodic systems, it was important to also investigate how the PES is sampled in thermal conditions at equilibrium. To this end, a series of Monte Carlo (MC) simulations were carried out in the canonical ensemble. A standard MC algorithm makes use of single-particle moves, which are known to be inadequate in the context of emergent structural hierarchy where the collective motion of clusters of particles are likely to be crucial.[66,118] We therefore used the virtual-move Monte Carlo (VMMC) algorithm as implemented in `PaSSion`, a Package for Soft Matter Simulation developed in-house following the prescription of Růžička and Allen.[119,120] The VMMC algorithm is a cluster-move algorithm involving collective movements of the particles, and has recently been found to be quite efficient in the study of hierarchical self-assembly of anisotropic colloidal particles.[66]

A series of VMMC simulations were performed in the canonical ensemble for systems of $N = 256$ and $N = 500$ ETP particles. For these simulations, the aspect ratio was again fixed at unity: $L^* = 1$, and the patches were set to be of the same width: $\alpha = \beta = 85°$. A hierarchy of interaction strengths was used, with $\epsilon_{AA} = 5$ and $\epsilon_{BB} = 1$ and the range of interaction fixed at 0.2σ ($s = 5$). The ideal density of cubic and hexagonal tetrastack, as given by `GlOSP`, is 0.1115, and so the density was set to 0.104 in order to account for thermal fluctuations during the simulation. The simulations are performed under periodic boundary conditions, using a cubic box and the minimum image convention. The orientations of the particles are represented by quaternions, and each VMMC cycle consists of N translational or collective rotational moves, with each move chosen with equal probability. The maximum step size for both translational and orientational degrees of freedom was fixed at 0.1. The potential energy was computed using a spherical cut-off 2.5σ (for the distance between the centres-of-mass of the particles), and a neighbour list for computational efficiency. The temperature at which each VMMC simulation is performed is quoted in the reduced units of ϵ/k_B, where k_B is the Boltzmann constant and this reduced temperature is represented by T^*. The particles initially start on an fcc lattice with random orientations. An initial run at $T^* = 1$ is then performed in order to "melt" the system and obtain a random initial configuration. At each T^* at least 1×10^6 cycles are performed

for equilibration, followed by a production stage. The number of steps in the production stage depends on the T^*, with each simulation allowed to proceed until the average energy plateaus. At $T^* = 0.3$, 3×10^7 VMMC cycles were performed. From the trajectory generated five independent configurations were extracted and cooled further.

In order to follow the progression of the self-assembly process, the number of tetrahedral clusters formed by the particles in the system were identified using the local orientational order parameter, q:

$$q = 1 - \frac{3}{8} \sum_{i=1}^{N_b-1} \sum_{j=i+1}^{N_b} \left(\cos \psi_{ij} + \frac{1}{3} \right)^2 \tag{3.8}$$

where N_b is the number of particles in the cluster under consideration (i.e., the nearest neighbours of particle i), ψ_{ij} is the angle subtended at the center of the cluster by the two vectors joining the center of particle i and j. The clusters of particles were determined using the rigid body site of the strong patch in order to ensure that only the emergent tetrahedra are considered during the simulation. For a perfect tetrahedron $q = 1$ and $N_b = 4$. For a perfect tetrastack crystal, each of these tetrahedra will sit on a diamond lattice point. We can, therefore, make use of previous analysis techniques that have been applied to study the assembly of colloidal particles into diamond. Specifically, we use the Steinhardt local order parameter $\bar{q}_{3m}(i)$, based on spherical harmonics $Y_{3m}(\hat{\mathbf{r}}_{ij})$:

$$\bar{q}_{3m}(i) = \frac{1}{N_b} \sum_{j=1}^{N_b(i)} Y_{3m}(\hat{\mathbf{r}}_{ij}) \tag{3.9}$$

$$\mathbf{q}_3(i) = \frac{\bar{q}_{3m}(i)}{\left[\sum_{m=-3}^{3} |\bar{q}_{3m}(i)|^2 \right]^{1/2}} \tag{3.10}$$

The probability distribution of the complex conjugate scalar product between the Steinhardt local bond order parameters of two neighbouring particles i and j, $\mathbf{q}_3(i) \cdot \mathbf{q}_3^*(j)$ can be used to distinguish between cubic and hexagonal diamond. In the probability distributions of both cubic and hexagonal diamond, there is a peak at -1. However, in hexagonal diamond only three neighbours give the $\mathbf{q}_3(i) \cdot \mathbf{q}_3^*(j) = -1$ signature, and there is an additional peak at -0.115.

The $N = 256$ simulations were predominantly performed for the purpose of rapidly exploring the state points on the temperature–number density plane to identify the region where crystallisation is observed. **Figure** 3.20 (**top**) shows how the average number of tetrahedra N_{Td}, characterised in terms of the orientational order parameter defined in Eqn. (3.8), and the average potential energy per particle, $U/(N\epsilon)$, evolve with T^*. We see that there is an initial drop in $U/(N\epsilon)$ coupled with an increase in N_{Td}. At $T^* = 0.1$ the first stage of assembly reaches completion with the formation of tetrahedral clusters exclusively corresponding to $N_{Td} = 64$. It was confirmed by visual inspection that the stronger patch-patch interactions drive the first stage of assembly, as would be expected. A short lived plateau in N_{Td} followed by a sharp increase was observed (along with a decrease in $U/(N\epsilon)$) between $T^* = 0.09$ and $T^* = 0.08$. This is suggestive of a structural transition taking place across this temperature window leading to emergent tetrahedra in a second stage of assembly driven by weaker patch-patch interactions. The peaks that appear in the radial distribution function (RDF) shown in **Figure** 3.20 (**bottom**) confirm the emergence of long-range correlations through the second stage of assembly. The essence of this two stage assembly process is captured by **Figure** 3.19.

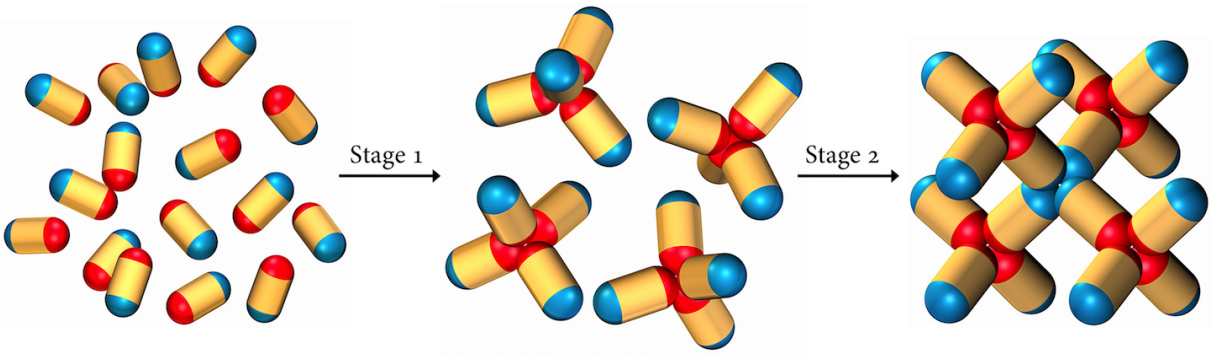

Figure 3.19: The hierarchical self-assembly pathway for ETP particles with $\epsilon_{AA} > \epsilon_{BB}$, where in the image the red patches symbolise patch A, and the blue patches patch B, will have two stages. **Stage 1** is the formation of the tetrahedral units, where the ETP particles maximise the number of strong-strong interaction. **Stage 2** is the assembly of the crystal structure, where the weak-weak patches come into play and an extended structure can form.

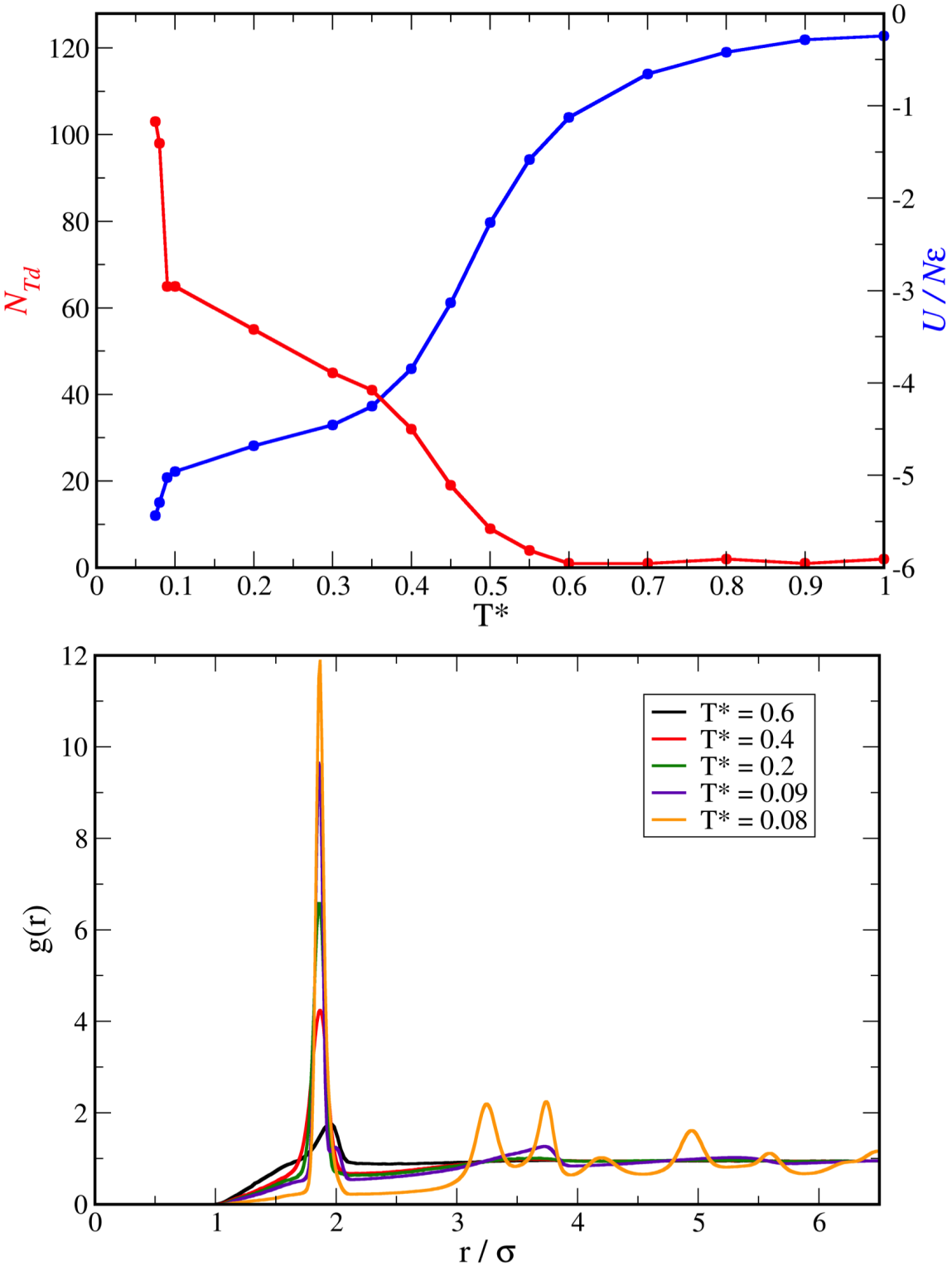

Figure 3.20: (**top**) The evolution of the number of tetrahedra, N_{Td}, and the average potential energy per particle, $U/(N\epsilon)$, for the $N = 256$ system of ETP particles, with a number density of $n = 0.104$. (**bottom**) The radial distribution function for this ETP system at five different reduced temperatures, using the center-to-center distances between the particles.

Following this initial exploration, we studied a system of $N = 500$ particles. The system was rapidly cooled from $T^* = 1$ to $T^* = 0.3$. Just as before, for all five systems the first stage of assembly was complete by $T^* = 0.1$. Each system was then cooled to $T^* = 0.09$. Given that the second stage of assembly was found to occur between $T^* = 0.09$ and $T^* = 0.08$, the systems were cooled more slowly below $T^* = 0.09$. We observed that the second stage of assembly began at $T^* = 0.089$, as revealed by the RDFs shown in **Figures** 3.21 and 3.23 for systems 3 and 5, respectively. Each system was then cooled further to a final temperature of $T^* = 0.085$. The tetrahedral centres were extracted for each trajectory, using the the order parameter q. The probability distribution of the complex conjugate scalar product between the Steinhardt local bond order parameters of two neighbouring particles i and j, $\mathbf{q}_3(i) \cdot \mathbf{q}_3^*(j)$, were also computed. Two of these probability distributions are shown in **Figures** 3.22 and 3.24 for systems 3 and 5, respectively. In a perfect CD structure, all four neighbours (denoted by j) of particle i have a $\mathbf{q}_3(i) \cdot \mathbf{q}_3^*(j) = -1$, whereas in the HD structure each particle only has three neighbours with $\mathbf{q}_3(i) \cdot \mathbf{q}_3^*(j) = -1$ and one other with $\mathbf{q}_3(i) \cdot \mathbf{q}_3^*(j) = -0.115$. It is clear from **Figures** 3.22 and 3.24 that both systems display regions of CD and HD as they display both peaks; however, the peak at -0.115 is much more defined for system 3 than for system 5. This suggests that both systems formed a mixed CT/HT phase; however, system 3 was more “HT-like” than system 5.

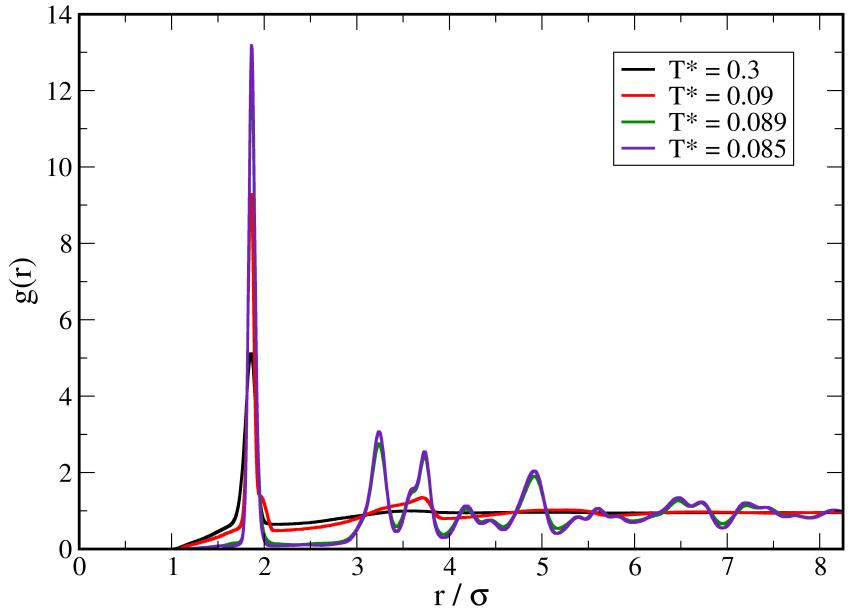

Figure 3.21: The radial distribution function (RDF) for the third independent system of $N = 500$ ETP particles at four different reduced temperatures, using the center-to-center distances. The structural transition that occurs at $T^* = 0.089$ is clearly shown by the increased number of peaks in the RDF, that then become better defined as the temperature is decreased.

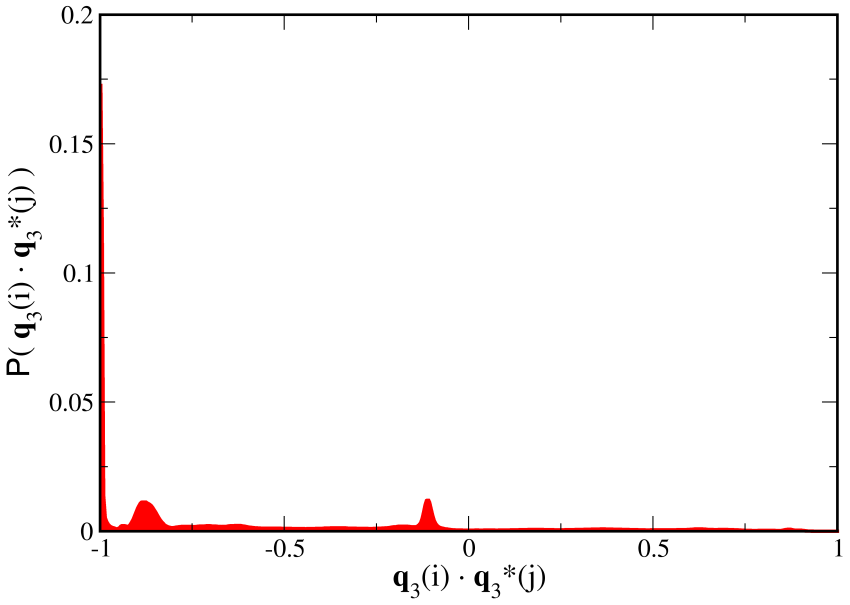

Figure 3.22: The probability distribution of the complex conjugate scalar product between the Steinhardt local bond order parameters of two neighbouring particles i and j, $\mathbf{q}_3(i) \cdot \mathbf{q}_3^*(j)$ for the third independent system of $N = 500$ ETP particles at $T^* = 0.085$, using the tetrahedral centres of the system. The peak at -1 is characteristic of cubic diamond, with the additional peak at -0.115 suggesting that hexagonal diamond motifs are also present.

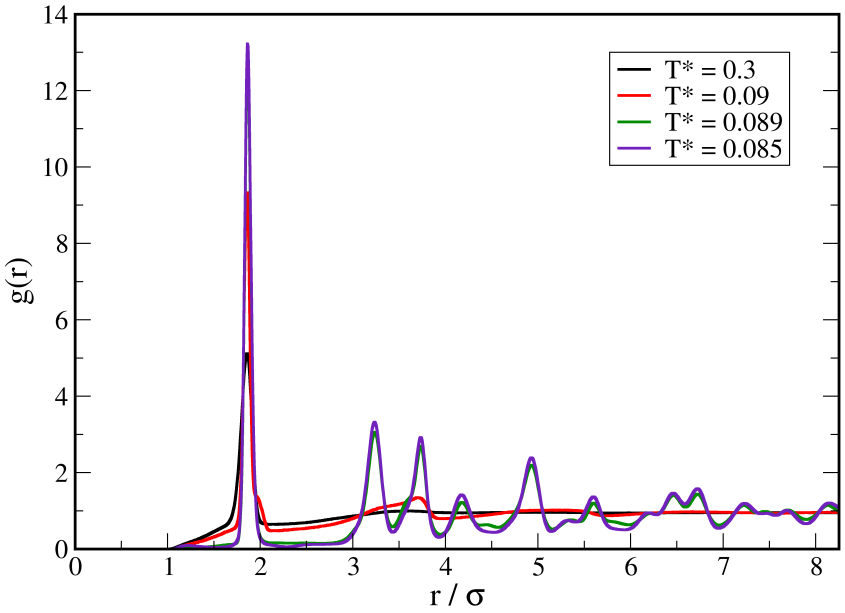

Figure 3.23: The radial distribution function (RDF) for the fifth independent system of $N = 500$ ETP particles at four different reduced temperatures, using the center-to-center distances. The structural transition that occurs at $T^* = 0.089$ is clearly shown by the increased number of peaks in the RDF, that then become better defined as the temperature is decreased.

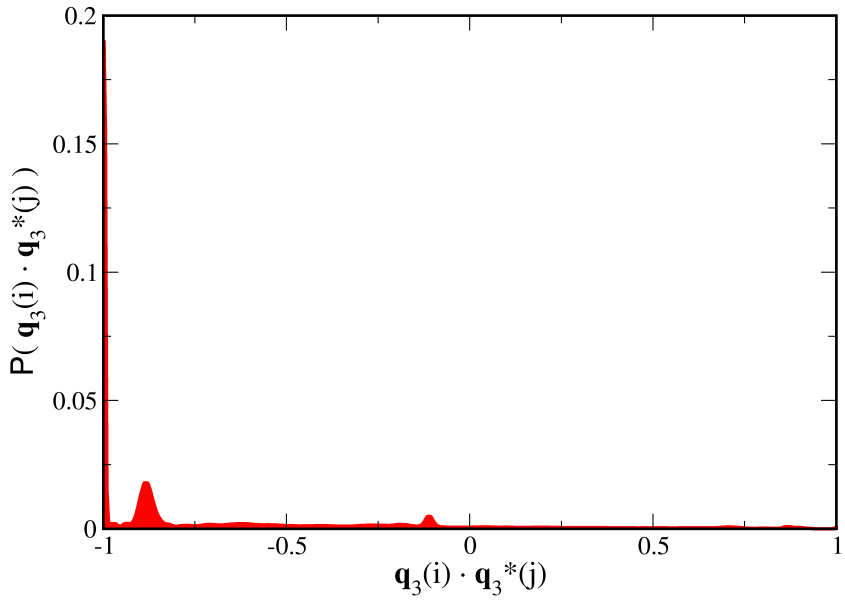

Figure 3.24: The probability distribution of the complex conjugate scalar product between the Steinhardt local bond order parameters of two neighbouring particles i and j, $\mathbf{q}_3(i) \cdot \mathbf{q}_3^*(j)$ for the fifth independent system of $N = 500$ ETP particles at $T^* = 0.085$, using the tetrahedral centres of the system. The peak at -1 is characteristic of cubic diamond, with the additional peak at -0.115 suggesting that hexagonal diamond motifs are also present.

In order to have an approximate quantitative measurement of how "CT-like" or "HT-like" each system is, the extended common neighbour analysis method can be used. CNA involves classifying particles according to their local environment. For each particle a list of N_b nearest neighbours, according to some cutoff, is generated. Then for each of those nearest neighbours three indices are computed, $\{a, b, c\}$, forming their CNA signature. The complete set of N_b CNA signatures are used to characterise each particle. Index a is the number of neighbours that the nearest neighbour under consideration has in common with the central particle (i.e., the number of common neighbours), b is the number of bonds between those common neighbours and c is the longest continuous chain of common neighbours. This analysis is easily applied to systems with close packing, however, for CD and HD the nearest neighbours have no bonds between them and so $a = 4$ and $b = c = 0$ for CD and HD. This issue can be remedied however, by exploiting the fact that CD and HD are formed from two interpenetrating fcc and hcp structures respectively. For a given particle its first nearest neighbours are identified (of which there are four), then their nearest neighbours are also identified (giving twelve additional second nearest neighbours to the central particle). A particle that represents a CD centre will form {4,2,1} pairs with all of the second nearest neighbours, whereas a HD centre will {4,2,1} pairs with six of the second nearest neighbours, and {4,2,2} pairs with the other six. This is known as the extended CNA.[121] If we focus on a perfect cubic tetrastack crystal, each particle is associated with two tetrahedral units, where the centre of each tetrahedral unit sits on a diamond lattice point. Given that cubic tetrastack and diamond share the same unit cell, we can say that in the unit cell of CT there are two unique tetrahedral vacancies (i.e., the lattice points for cubic diamond) and therefore, there are $N/2$ tetrahedral vacancies in a perfect CT crystal of N particles. The same argument can be applied to hexagonal tetrastack and diamond, therefore, we say that for a system of N particle we expect at most to identify $N/2$ unique tetrahedra. Therefore, we can exploit the fact that the centres of the tetrahedra that form CT and HT lie on diamond lattice points to determine whether a given system has more cubic diamond (CD) or hexagonal diamond (HD) character. The extended CNA algorithm, as implemented in the freely available visualisation software `OVITO`[122], is used in tandem with the order parameter q, to provide an approximate description of whether a given tetrahedral centre displays CD-like or HD-like character. The general idea behind this is shown in **Figure** 3.25.

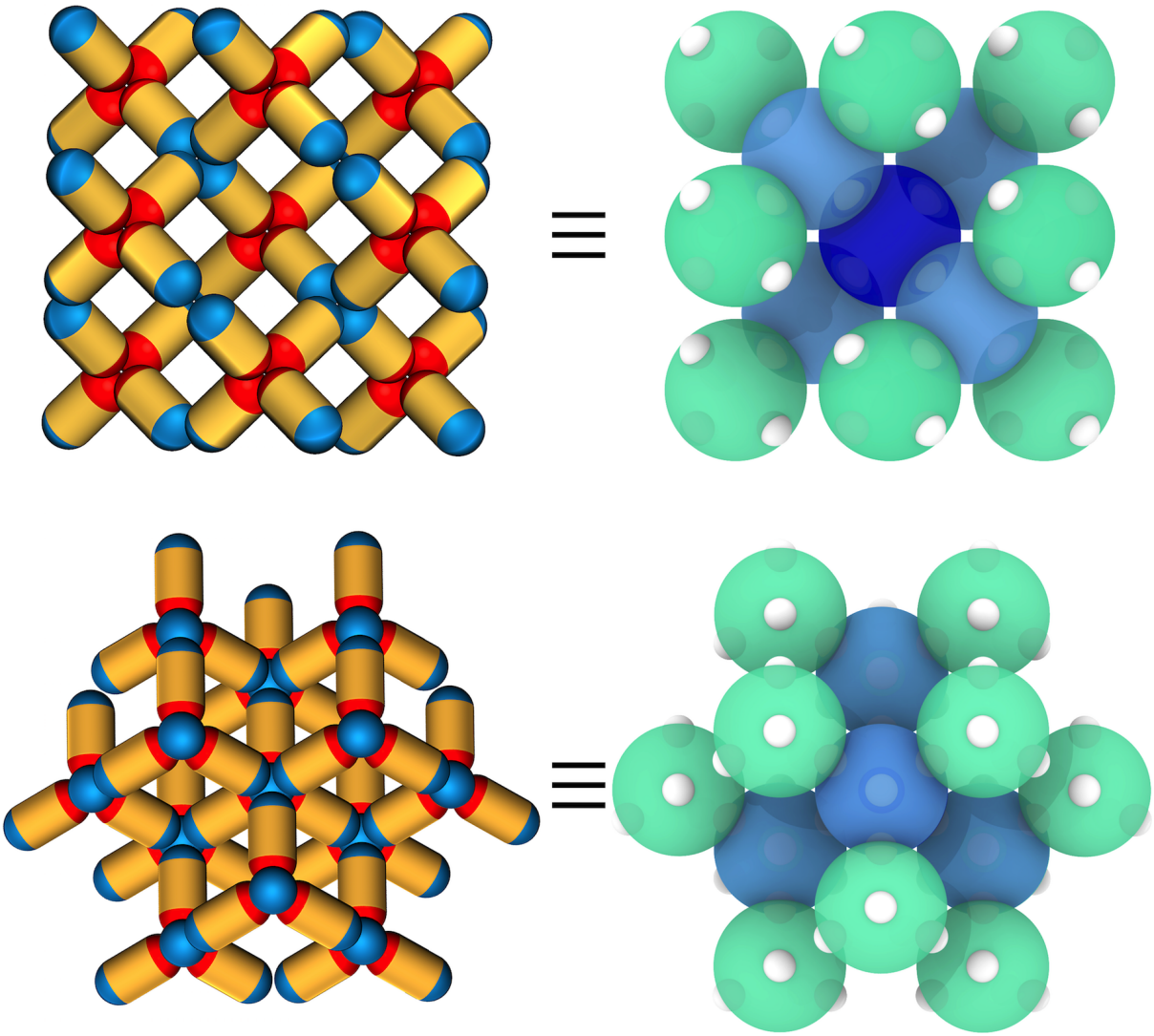

Figure 3.25: (**left**) The (001) and (111) views of a segment of cubic tetrastack with ETP particles are shown. There are 17 unique tetrahedral centres, with 13 formed by strong-strong interactions (red) and 4 formed by weak-weak interactions (blue). (**right**) The tetrahedral centres are represented as translucent spheres, with the centres-of-mass of the particles represented by the white spheres. The central (navy) sphere indicates a tetrahedron labelled as a cubic diamond centre, the sky blue and green spheres are the first and second neighbours of this centre respectively.

Given that the simulation is performed in a cubic box, and the density of the system is not the ideal density, we expect N_{Td} to be smaller than the maximum value of $N/2$. **Table** 3.4 shows the average fraction of tetrahedra assembled, $\langle f_{Td} \rangle = \langle 2N_{Td}/N \rangle$, and the average fraction of those tetrahedra characterised as diamond centres, $\langle f_x^0 \rangle$, first neighbours to a diamond centre, $\langle f_x^1 \rangle$ or second neighbours to a diamond centre, $\langle f_x^2 \rangle$, where $x = cd$ for cubic diamond and $x = hd$ for hexagonal diamond.

System	$\langle f_{Td} \rangle$	$\langle f_{cd}^0 \rangle$	$\langle f_{cd}^1 \rangle$	$\langle f_{cd}^2 \rangle$	$\langle f_{hd}^0 \rangle$	$\langle f_{hd}^1 \rangle$	$\langle f_{hd}^2 \rangle$
1	0.81	0.09	0.14	0.17	0.07	0.15	0.24
2	0.83	0.15	0.16	0.17	0.13	0.13	0.16
3	0.83	0.08	0.09	0.12	0.17	0.20	0.24
4	0.78	0.07	0.06	0.08	0.10	0.19	0.27
5	0.83	0.21	0.22	0.25	0.05	0.07	0.08

Table 3.4: The fraction of tetrahedra formed at $T^* = 0.085$ for the five $N = 500$ VMMC simulations. The fraction of those tetrahedra that are characterised as cubic or hexagonal diamond centres are given. Additionally, the fraction of tetrahedra that are not diamond centres, but are first or second neighbours of a diamond centre are shown.

It is clear that a mixed phase was observed in all of the systems studied, as they all gave signatures for both CD and HD. Although a perfect crystal was not formed, we saw that systems 3 and 5 displayed a clear majority of HD and CD respectively. Images of these structures are shown in **Figures** 3.26 and 3.27, using the representation of **Figure** 3.25. The tetrahedral centres are coloured according to whether they are characterised as CD or HD centres, or whether they are first or second neighbours of a CD or HD centre. Additionally, grey particles represent tetrahedra that are unrelated to either diamond structure. In **Figure** 3.26 the characteristic hexagonal columns of HT are clearly visible, separated by a region of CT. Whereas, the (111) staggered Kagome planes of CT are visible in **Figure** 3.27, with regions of CT dominating the system.

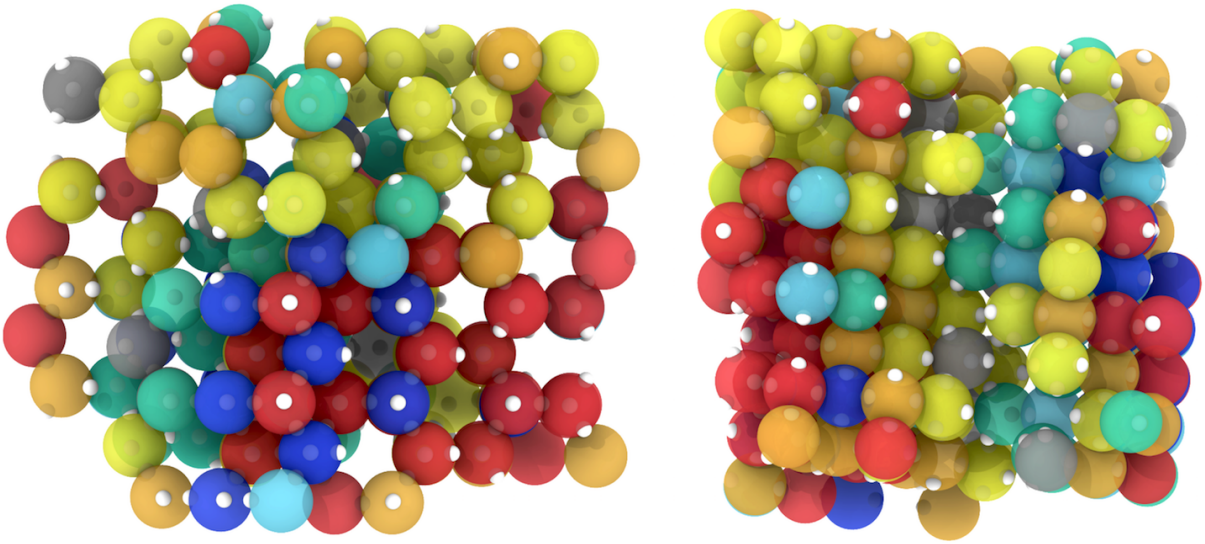

Figure 3.26: The final configuration of system 3 visualised using `OVITO`. The image on the left hand side particularly highlights the emergence of hexagonal tetrastack in this system, with the columns of eclipsed tetrahedra showing.

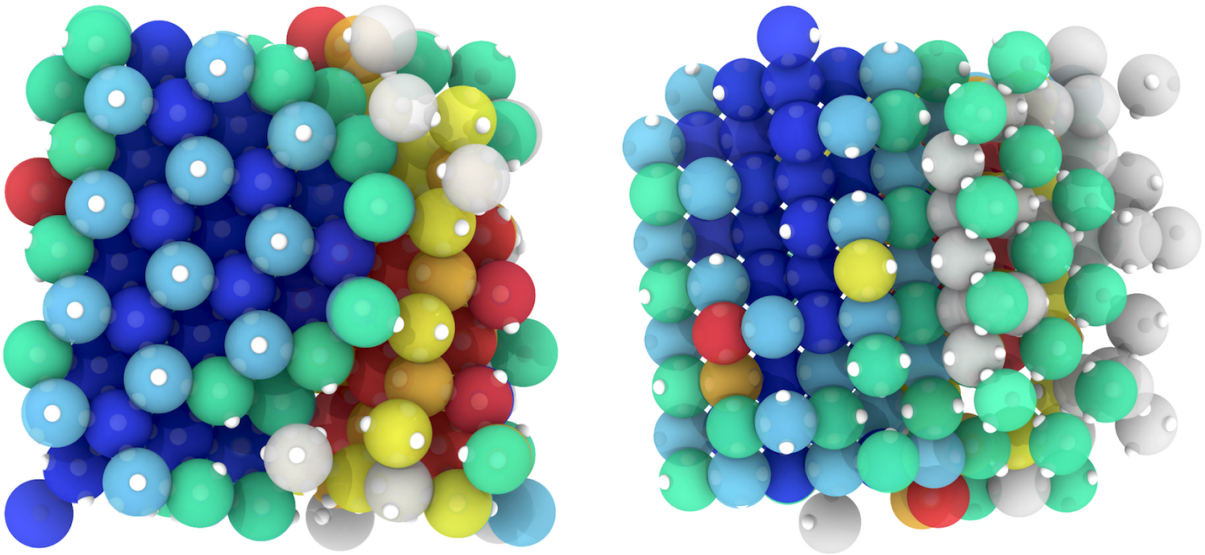

Figure 3.27: The final configuration of system 5, visualised using `OVITO`. The image on the left hand side particularly highlights the emergence of cubic tetrastack in this system, with the planes of staggered tetrahedra clearly visible.

Nothing	CD	CD($1st$)	CD($2nd$)	HD	HD($1st$)	HD($2nd$)
grey	navy	sky blue	teal	red	orange	yellow

Table 3.5: Colour key for the characterisation of tetrahedral centres in **Figures** 3.26 and 3.27

We have shown that, by following a hierarchical self-assembly pathway, the ETP particles can be expected to form a mixed phase of CT and HT under equilibrium conditions. This has often been suggested to be an issue, in the context of the spherical particles, as it is suggested that only a perfect CT structure will possess a photonic band gap. However, as we have discussed in the previous section, this is not necessarily the case; and that the photonic band gap for the CT and HT structures formed with ETP particles can be attributed to the tetrahedral coordination of the particles. Therefore, although a perfect crystal has not been formed, we can still expect the ETP particles to assemble into a structure that possesses a complete photonic band gap.

Summary and Outlook

We set out to explore, using a variety of computational methods, a bottom-up route to certain colloidal open crystals. While the diamond and tetrastack crystals composed of dielectric spheres are well-known to have complete photonic band gaps, the rod-connected diamond structure is currently the champion structure for photonic crystals. This set the context for us to target elongated analogues of the tetrastack crystals, in anticipation of finding enhanced properties relative to the spherical counterparts. To this end, we have considered elongated triblock patchy particles on the colloidal scale and shown that the design space supports elongated analogues of tetrastack crystals, with the cubic and hexagonal polymorphs both displaying a complete photonic band gap of 18% and 7% respectively. For the spherical counterparts, the cubic polymorph displays a band gap of 4% and the hexagonal polymorph has no band gap. We have, therefore, shown that through the introduction of geometric anisotropy into the particles, the photonic properties of the structures is indeed enhanced. Additionally, we have shown that the eigenmodes of the cubic and hexagonal polymorphs have almost identical field patterns, which suggested that Mie scattering, and the tetrahedral coordination of the particles, are crucial for the opening of the band gap. The cubic polymorph has the wider band gap most likely due to its more spherical Brillouin zone, resulting in greater synergy between the Bragg and Mie scattering mechanisms. We have devised a strategy for designer triblock patchy particles to follow a hierarchical self-assembly pathway to form a crystalline, albeit mixed, cubic and hexagonal tetrastack phase. However, as it is the tetrahedral coordination of the particles which is suggested to play the major role in the opening of the band gap, and given that both polymorphs display a complete band gap, it is expected that these mixed phases would also have a complete photonic band gap. However, further studies are required in order to confirm this.

Additionally, given the emphasis we have put on the role of Mie resonant scattering for the photonic properties of these structures we also suggest that scattering studies for the individual particles be performed, as well as, for clusters of the particles. This is to confirm the role of the Mie-like resonances observed in the crystal structures in the opening of the band gap. The field patterns of the eigenmodes for the diamond structures with spherical particles should also be visualised in order to see whether there is a correlation between the field patterns of diamond and tetrastack. This would, again, provide further evidence for the role of the tetrahedral coordination of the particles in their photonic properties.

There is an undeniable relationship with the local coordination of the particles and the photonic properties of their crystal structures. Additionally, hierarchical self-assembly provides a particularly attractive route to ordered crystal structures. Looking beyond this system, and that of diamond, these two observations could be used in tandem to potentially realise other structures that display complete photonic band gaps. A series of metamolecular structures have previously been proposed to mimic the chemical bonds in molecules, giving plasmonic molecules.[123–125] We propose that it should also be possible to generate "dielectric molecules". Guided by the photonic properties of clusters of dielectric particles, it should be possible to rationally design the hierarchical self-assembly of dielectric molecules into photonic band gap materials.

Appendices

Inexact Line Search Methods

A.1 The Wolfe Conditions

The most obvious inexact line search condition to enforce at each iteration is that α_k provides a decrease in U_k, so that $U(\boldsymbol{x}_k + \alpha_k \boldsymbol{d}_k) < U(\boldsymbol{x}_k)$. However, this condition is not sufficiently stringent as it does not prevent steps that are too long. Instead we formulate a condition that provides a *sufficient decrease* in U_k Given a descent direction, $\boldsymbol{d}_k$, the coordinates, $\boldsymbol{x}_k$ and a constant, $c_1 \in (0, 1)$ we say that α_k satisfies the **Armijo condition** if:

$$U(\boldsymbol{x}_k + \alpha_k \boldsymbol{d}_k) \leq U(\boldsymbol{x}_k) + c_1 \alpha_k \nabla U_k \cdot \boldsymbol{d}_k \tag{A.1}$$

We can use the Armijo condition to find a suitable step-length in *backtracking algorithm*, where we take some initial guess of α_k and gradually decrease it until the Armijo condition is satisfied.

Algorithm 3: Backtracking Armijo line-search algorithm

$U_k = U(\boldsymbol{x}_k),\ \boldsymbol{d}_k \leftarrow -\nabla U_k$
$\alpha_0 > 0,\ c_1 \in (0, 1),\ \tau \in (0, 1)$
$i = 0$
while $U(\boldsymbol{x}_k + \alpha_i \boldsymbol{d}_k) \leq U(\boldsymbol{x}_k) + c_1 \alpha_i \nabla U_k \cdot \boldsymbol{d}_k$ **do**
    $\alpha_{i+1} \leftarrow \tau \alpha_i$
    $i = i + 1$
end
return $\alpha_k \leftarrow \alpha_i$

The Armijo condition is not enough to guarantee that a suitable step size is chosen as *Eqn.* (A.1) is satisfied for *all* sufficiently small values of α_k. To exclude steps that are too short we must introduce a second requirement for α_k to satisfy. Given a descent direction, $\boldsymbol{d}_k$, the coordinates, $\boldsymbol{x}_k$ and a constant, $c_2 \in (c_1, 1)$ we say that α_k satisfies the **curvature condition** if:

$$\nabla U(\boldsymbol{x}_k + \alpha_k \boldsymbol{d}_k) \cdot \boldsymbol{d}_k \geq c_2 \nabla U_k \cdot \boldsymbol{d}_k \tag{A.2}$$

The left hand side of *Eqn.* (A.2) is simply: $\mathrm{d}U(\boldsymbol{x}_{k+1})/\mathrm{d}\alpha_k$, and so the curvature condition ensures that the gradient of $\mathrm{U}(\boldsymbol{x}_{k+1})$ is c_2 times greater than the initial gradient at $\mathrm{U}(\boldsymbol{x}_k)$. Therefore, if α_k satisfies the curvature condition we cannot expect much more of a decrease in U_k along the current direction. Taken together *Eqns.* (A.1) and (A.2) are known as the *weak Wolfe conditions*. However, we can alter the curvature condition slightly, to ensure that $U(\boldsymbol{x}_k + \alpha_k \boldsymbol{d}_k)$ is in the region of a stationary point and arrive at the *strong Wolfe conditions*: Given a descent direction, $\boldsymbol{d}_k$, the coordinates, $\boldsymbol{x}_k$ and the constants, $0 < c_1 < c_2 < 1$ we say that α_k satisfies the **strong Wolfe condition** if:

$$\begin{gathered} U(\boldsymbol{x}_k + \alpha_k \boldsymbol{d}_k) \leq U(\boldsymbol{x}_k) + c_1 \alpha_k \nabla U_k \cdot \boldsymbol{d}_k \\ \text{and} \\ |\nabla U(\boldsymbol{x}_k + \alpha_k \boldsymbol{d}_k) \cdot \boldsymbol{d}_k| \leq c_2 |\nabla U_k \cdot \boldsymbol{d}_k| \end{gathered} \tag{A.3}$$

The only difference between the weak Wolfe conditions and the strong Wolfe conditions is that $\mathrm{d}U(\boldsymbol{x}_{k+1})/\mathrm{d}\alpha_k$ is not allowed to be too large, and so we only consider points that are in the region of a stationary point. We can outline an algorithm that uses the strong Wolfe conditions to find α_k in two stages: (i) Given an initial estimate of α_k, keep increasing it until it is acceptable or an interval that brackets acceptable step lengths is found. (ii) If the interval is found, an auxiliary function is called to iteratively decrease the size of the interval until an acceptable value for α_k is found.

Background Theory for Photonic Crystals

B.1 Derivation of the Master Equation

This section takes inspiration from Ref. [16] and so the the reader is directed here for a complete exposition of the subject. First we must be able to describe the propagation of electromagnetic waves through a photonic crystal. We start with the four macroscopic Maxwell equations:

$$\nabla \cdot \mathbf{D}(\mathbf{r}, t) = \rho \tag{B.1}$$

$$\nabla \cdot \mathbf{B}(\mathbf{r}, t) = 0 \tag{B.2}$$

$$\nabla \times \mathbf{E}(\mathbf{r}, t) = -\frac{\partial \mathbf{B}(\mathbf{r}, t)}{\partial t} \tag{B.3}$$

$$\nabla \times \mathbf{H}(\mathbf{r}, t) = \frac{\partial \mathbf{D}(\mathbf{r}, t)}{\partial t} + \mathbf{J} \tag{B.4}$$

where $\mathbf{r}$ is vector describing a point in Cartesian space and t is time. These are the Maxwell equations in differential form and in SI units, this form is chosen to make the derivation simpler. We will consider our photonic crystals to be mixed dielectric media, and so contain regions of homogeneous, dielectric material without any free charges or currents. In the case of non-conductive media, such as silica, the current and charge density are: $\mathbf{J} = \mathbf{0}$ and $\rho = 0$. The magnetic and electric flux densities ($\mathbf{B}$ and $\mathbf{D}$) are related to the magnetic and electric field vectors ($\mathbf{H}$ and $\mathbf{E}$) by the constitutive relations:

$$\begin{aligned} \mathbf{B}(\mathbf{r}, t) &= \mu_0 \mathbf{H}(\mathbf{r}, t) + \mathbf{M} \\ \mathbf{D}(\mathbf{r}, t) &= \varepsilon_0 \mathbf{E}(\mathbf{r}, t) + \mathbf{P} \end{aligned} \tag{B.5}$$

where ε_0 is the permittivity of free space, $8.85 \times 10^{-12}\ F/\mathrm{m}$, and μ_0 is the permeability of free space, $4\pi \times 10^{-7}\ H/\mathrm{m}$. $\mathbf{M}$ is the induced magnetic polarisation of the medium, and for a

non-magnetic medium (such as silica) $\mathbf{M} = \mathbf{0}$, therefore we take the magnetic flux density to be:

$$\mathbf{B}(\mathbf{r}, t) = \mu_0 \mathbf{H}(\mathbf{r}, t) \tag{B.6}$$

$\mathbf{P}$ is the induced polarisation of the medium, where for a dielectric medium a nonzero $\mathbf{P}$ is induced by an external electric field, $\mathbf{E}$. If we consider a medium made up of positive and negative charges (e.g. protons and electrons), then when an electric field is present the positive and negative charges will become separated. This charge separation results in an additional electric field called the induced polarisation, $\mathbf{P}$. The nature of the induced polarisation depends on the medium considered. If the medium is linear and isotropic then the induced polarisation is linearly proportional to the external electric field and can be expressed as:

$$\mathbf{P} = \varepsilon_0 \cdot \chi \mathbf{E}(\mathbf{r}, t) \tag{B.7}$$

where χ is the electric susceptibility, and can be considered as a proportionality constant between $\mathbf{P}$ and $\mathbf{E}$. For an isotropic medium, such as silica glass, linear susceptibility can be taken to be a scalar, we can now re-write the electric flux density as:

$$\mathbf{D}(\mathbf{r}, t) = \varepsilon_0 \varepsilon \mathbf{E}(\mathbf{r}, t) \tag{B.8}$$

where $\varepsilon = 1 + \chi$, and is known as the *dielectric constant* (or relative permittivity) of a dielectric material. The higher the value of ε the slower the propagation of light through that medium. The dielectric constant of a non-uniform medium is denoted by $\varepsilon(\mathbf{r})$.
We can now re-write the Maxwell equations as:

$$\nabla \cdot \Big[\varepsilon(\mathbf{r})\mathbf{E}(\mathbf{r}, t)\Big] = 0 \tag{B.9}$$

$$\nabla \cdot \mathbf{H}(\mathbf{r}, t) = 0 \tag{B.10}$$

$$\nabla \times \mathbf{E}(\mathbf{r}, t) = -\mu_0 \frac{\partial \mathbf{H}(\mathbf{r}, t)}{\partial t} \tag{B.11}$$

$$\nabla \times \mathbf{H}(\mathbf{r}, t) = \varepsilon_0 \varepsilon(\mathbf{r}) \frac{\partial \mathbf{E}(\mathbf{r}, t)}{\partial t} \tag{B.12}$$

We can eliminate $\mathbf{E}(\mathbf{r},t)$ from Eqn. (B.12) to obtain a wave equation for the magnetic field. We divide Eqn. (B.12) by $\varepsilon(\mathbf{r})$ to get:

$$\frac{1}{\varepsilon(\mathbf{r})}\nabla\times\mathbf{H}(\mathbf{r},t)=\varepsilon_0\frac{\partial\mathbf{E}(\mathbf{r},t)}{\partial t} \tag{B.13}$$

Next we take the curl of both sides:

$$\nabla\times\left(\frac{1}{\varepsilon(\mathbf{r})}\nabla\times\mathbf{H}(\mathbf{r},t)\right)=\varepsilon_0\frac{\partial}{\partial t}\nabla\times\mathbf{E}(\mathbf{r},t) \tag{B.14}$$

We can then insert Eqn. (B.11) into (B.14):

$$\nabla\times\left(\frac{1}{\varepsilon(\mathbf{r})}\nabla\times\mathbf{H}(\mathbf{r},t)\right)=-\varepsilon_0\mu_0\frac{\partial^2}{\partial t^2}\mathbf{H}(\mathbf{r},t) \tag{B.15}$$

If we then repeat a similar process for Eqn. (B.11) we arrive at the two wave equations:

$$\nabla\times\left(\frac{1}{\varepsilon(\mathbf{r})}\nabla\times\mathbf{H}(\mathbf{r},t)\right)=-\frac{1}{c^2}\frac{\partial^2}{\partial t^2}\mathbf{H}(\mathbf{r},t) \tag{B.16}$$

$$\frac{1}{\varepsilon(\mathbf{r})}\nabla\times\left(\nabla\times\mathbf{E}(\mathbf{r},t)\right)=-\frac{1}{c^2}\frac{\partial^2}{\partial t^2}\mathbf{E}(\mathbf{r},t) \tag{B.17}$$

where c is the vacuum speed of light: $c=1/\sqrt{\varepsilon_0\mu_0}=2.9979\times10^8$ m/s. We can describe the electric and magnetic fields as a set of superimposed sinusoidal monochromatic waves (i.e. sinusoidal waves with a constant angular frequency, ω). We can then write the fields as the product of a spatial pattern, $\mathbf{H}(\mathbf{r})$ and $\mathbf{E}(\mathbf{r})$, and a complex exponential:

$$\begin{aligned}\mathbf{H}(\mathbf{r},t)&=\sum_\omega \mathrm{Re}\left\{\mathbf{H}(\mathbf{r})\exp(-i\omega t)\right\}\\ \mathbf{E}(\mathbf{r},t)&=\sum_\omega \mathrm{Re}\left\{\mathbf{E}(\mathbf{r})\exp(-i\omega t)\right\}\end{aligned} \tag{B.18}$$

where we take the real parts to acquire the physical fields. The two divergence equations require $\mathbf{H}(\mathbf{r})$ and $\mathbf{E}(\mathbf{r})$ to be perpendicular to the direction of propagation, meaning that the fields must be built from transverse electromagnetic waves.

We can then re-write the Maxwell equations (for the last time) as:

$$\nabla \cdot \Big[\varepsilon(\mathbf{r})\mathbf{E}(\mathbf{r})\Big] = 0 \tag{B.19}$$

$$\nabla \cdot \mathbf{H}(\mathbf{r}) = 0 \tag{B.20}$$

$$\nabla \times \mathbf{E}(\mathbf{r}) = i\omega\mu_0\mathbf{H}(\mathbf{r}) \tag{B.21}$$

$$\nabla \times \mathbf{H}(\mathbf{r}) = -i\omega\varepsilon_0\varepsilon(\mathbf{r})\mathbf{E}(\mathbf{r}) \tag{B.22}$$

Eqn. (B.16) also then simplifies to:

$$\nabla \times \left(\frac{1}{\varepsilon(\mathbf{r})}\nabla \times \mathbf{H}(\mathbf{r})\right) = \left(\frac{\omega}{c}\right)^2 \mathbf{H}(\mathbf{r}) \tag{B.23}$$

This is known as the *Master Equation*, where each eigenmode, $\mathbf{H}(\mathbf{r})$, (also referred to as the harmonic modes or normal modes) correspond to one of the sinusoidal monochromatic waves from which the magnetic field is constructed, and the eigenvalues, $(\omega/c)^2$, provide the corresponding angular frequencies. The electric field can then be computed using:

$$\mathbf{E}(\mathbf{r}) = \frac{i}{\omega\varepsilon_0\varepsilon(\mathbf{r})}\nabla \times \mathbf{H}(\mathbf{r}) \tag{B.24}$$

B.2 Electromagnetic Variational Theorem

The eigenmodes, $\mathbf{H}(\mathbf{r})$, represent the spatial patterns of the magnetic field and the eigenvalues, ω^2/c^2, are proportional to the squared frequencies of those modes. The differential operator, $\hat{\Theta}$, is a Hermitian operator. If we define some arbitrary Hermitian operator, $\hat{\Xi}$, and two fields $\mathbf{A}(\mathbf{r})$ and $\mathbf{B}(\mathbf{r})$, then $\hat{\Xi}$ has the special property:

$$\int \mathrm{d}^3\mathbf{r}\ \mathbf{A}^*(\mathbf{r}) \cdot \hat{\Xi}\mathbf{B}(\mathbf{r}) = \int \mathrm{d}^3\mathbf{r}\ \left\{\hat{\Xi}\mathbf{A}(\mathbf{r})\right\}^* \cdot \mathbf{B}(\mathbf{r}) \tag{B.25}$$

where '$*$' denotes the complex conjugate and the integral over all space of a dot product of the two fields $\mathbf{A}(\mathbf{r})$ and $\mathbf{B}(\mathbf{r})$ is known as the *inner product* which we can denote as:

$$\langle \mathbf{A}, \mathbf{B} \rangle \triangleq \int \mathrm{d}^3\mathbf{r}\ \mathbf{A}^*(\mathbf{r}) \cdot \mathbf{B}(\mathbf{r}) \tag{B.26}$$

Therefore, we can rewrite Eqn. (B.25) as:

$$\langle \mathbf{A}, \hat{\Xi}\mathbf{B} \rangle = \langle \hat{\Xi}\mathbf{A}, \mathbf{B} \rangle \tag{B.27}$$

We can then show that the Hermicity of $\hat{\Theta}$ forces any two eigenmodes, $\mathbf{H}_1(\mathbf{r})$ and $\mathbf{H}_2(\mathbf{r})$, with different corresponding eigenfrequencies, ω_1 and ω_2, to have an inner product of zero:

$$\begin{gathered} \langle \mathbf{H}_2, \hat{\Theta}\mathbf{H}_1 \rangle = (\omega_1^2/c^2)\langle \mathbf{H}_2, \mathbf{H}_1 \rangle \\ \omega_1^2 \langle \mathbf{H}_2, \mathbf{H}_1 \rangle = c^2 \langle \mathbf{H}_2, \hat{\Theta}\mathbf{H}_1 \rangle = c^2 \langle \hat{\Theta}\mathbf{H}_2, \mathbf{H}_1 \rangle = \omega_2^2 \langle \mathbf{H}_2, \mathbf{H}_1 \rangle \\ \therefore \quad (\omega_1^2 - \omega_2^2)\langle \mathbf{H}_2, \mathbf{H}_1 \rangle = 0 \end{gathered} \tag{B.28}$$

Therefore, if $\omega_1 \neq \omega_2$, then $\langle \mathbf{H}_2, \hat{\Theta}\mathbf{H}_1 \rangle = 0$ and so we say that $\mathbf{H}_1(\mathbf{r})$ and $\mathbf{H}_2(\mathbf{r})$ are orthogonal modes. The idea of orthogonality is most easily understood in terms of 1-dimensional functions:

$$\langle f, g \rangle = \int f(x) g(x) \, \mathrm{d}x = 0 \tag{B.29}$$

For example consider the integral of the product of two sine curves, i.e., let $f(x) = \sin x$ and $g(x) = \sin 2x$. If the frequencies of the two sine curves are different then between some interval, for instance $[0, 2\pi]$, the two curves are of opposite sign as often as they are of the same sign. The product of these two sinusoidal functions will therefore be positive as often as it is negative, therefore, the integral of their product will be zero. The set of functions $f_n(x) = \sin(n\pi x/L)$ can be shown to all be orthogonal to one another for $x \in [0, L]$. Each of these functions has a different number of nodes, with f_n having $n-1$ nodes. The concept that orthogonal modes, of different frequencies, possess a different number of spatial nodes can be extended to three-dimensional functions, with a harmonic mode of lower frequency *generally* possessing fewer nodes than higher frequency modes. There is in fact more to consider for the eigenmodes that we extract for our photonic crystal. We return to the Master equation, this time written as:

$$\frac{\langle \mathbf{H}, \hat{\Theta}\mathbf{H} \rangle}{\langle \mathbf{H}, \mathbf{H} \rangle} = \frac{\omega^2}{c^2} \tag{B.30}$$

From this we define the functional $U_f(\mathbf{H})$, called *Rayleigh quotient*:

$$U_f(\mathbf{H}) \triangleq \frac{\langle \mathbf{H}, \hat{\Theta}\mathbf{H} \rangle}{\langle \mathbf{H}, \mathbf{H} \rangle} \tag{B.31}$$

where the lowest eigenfrequency mode has the corresponding field pattern that minimises $U_f(\mathbf{H})$, which can be shown to be equal to:

$$U_f(\mathbf{H}) = \frac{\langle \nabla \times \mathbf{E}, \nabla \times \mathbf{E} \rangle}{\langle \mathbf{E}, \varepsilon(\mathbf{r})\mathbf{E} \rangle} = \frac{\int \mathrm{d}^3\mathbf{r} \; |\nabla \times \mathbf{E}(\mathbf{r})|^2}{\int \mathrm{d}^3\mathbf{r} \; \varepsilon(\mathbf{r}) |\mathbf{E}(\mathbf{r})|^2} \tag{B.32}$$

By minimising the variational functional, we see that the lowest energy modes are those with an electric field profile that is localised within high dielectric regions (i.e., maximising the denominator), and have little spatial oscillation (i.e., minimising the numerator), whilst also being orthogonal to other modes of a different frequency.

B.3 Bloch-Floquet Theorem

We know that the differential operator, $\hat{\Theta}$, and the eigenmodes, $\mathbf{H}(\mathbf{r})$, possess the translational symmetry of the crystal. We can therefore introduce a translation operator, $\hat{\mathrm{T}}_{\mathbf{R}}$, such that:

$$\hat{\mathrm{T}}_{\mathbf{R}} \mathbf{H}(\mathbf{r}) \triangleq \mathbf{H}(\mathbf{r} + \mathbf{R}) \tag{B.33}$$

Application of $\hat{\mathrm{T}}_{\mathbf{R}}$ to the Master equation gives:

$$\hat{\mathrm{T}}_{\mathbf{R}} \hat{\Theta}(\mathbf{r}) \mathbf{H}(\mathbf{r}) = \hat{\Theta}(\mathbf{r} + \mathbf{R}) \mathbf{H}(\mathbf{r} + \mathbf{R}) = \hat{\Theta}(\mathbf{r}) \mathbf{H}(\mathbf{r} + \mathbf{R}) = \hat{\Theta}(\mathbf{r}) \hat{\mathrm{T}}_{\mathbf{R}} \mathbf{H}(\mathbf{r}) \tag{B.34}$$

We see that $\hat{\mathrm{T}}_{\mathbf{R}}$ commutes with $\hat{\Theta}$ ($\hat{\mathrm{T}}_{\mathbf{R}} \hat{\Theta} = \hat{\Theta} \hat{\mathrm{T}}_{\mathbf{R}}$) and so we can assert that a given eigenmode, $\mathbf{H}(\mathbf{r})$, is simultaneously an eigenfunction of both operators:

$$\hat{\Theta}\mathbf{H}(\mathbf{r}) = \frac{\omega^2}{c^2}\mathbf{H}(\mathbf{r}) \quad \text{and} \quad \hat{\mathrm{T}}_{\mathbf{R}} \mathbf{H}(\mathbf{r}) = t(\mathbf{R})\mathbf{H}(\mathbf{r}) \tag{B.35}$$

Additionally, we see that the application of two successive translations to $\mathbf{H}(\mathbf{r})$ gives:

$$\hat{\mathrm{T}}_{\mathbf{R}}\hat{\mathrm{T}}_{\mathbf{R}'}\mathbf{H}(\mathbf{r}) = t(\mathbf{R})\hat{\mathrm{T}}_{\mathbf{R}'}\mathbf{H}(\mathbf{r}) = t(\mathbf{R})t(\mathbf{R}')\mathbf{H}(\mathbf{r}) \tag{B.36}$$

equivalently, we can write:

$$\hat{\mathrm{T}}_{\mathbf{R}}\hat{\mathrm{T}}_{\mathbf{R}'}\mathbf{H}(\mathbf{r}) = \hat{\mathrm{T}}_{\mathbf{R}+\mathbf{R}'}\mathbf{H}(\mathbf{r}) = t(\mathbf{R}+\mathbf{R}')\mathbf{H}(\mathbf{r}) \tag{B.37}$$

Therefore, the eigenvalues for the translation operator must satisfy the following relation:

$$t(\mathbf{R}+\mathbf{R}') = t(\mathbf{R})t(\mathbf{R}') \tag{B.38}$$

They can thus be decomposed into a product of three components, one for each lattice vector:

$$t(\mathbf{R}) = t(\mathbf{a}_1)^{n_1}t(\mathbf{a}_2)^{n_2}t(\mathbf{a}_3)^{n_3} \tag{B.39}$$

It is immediately obvious that we can always choose $t(\mathbf{a}_i)$ to be of the form: $t(\mathbf{a}_i) = e^{i2\pi x_i}$, where, $x_i \in \mathbb{R}$ (x_i can actually be any complex number, however, due to the periodic boundary conditions imposed on the eigenmode x_i must be real). This means that we can express the eigenvalues as: $t(\mathbf{R}) = e^{i\boldsymbol{k}\cdot\mathbf{R}}$ where, $\boldsymbol{k} = \sum_{i=1}^{3} x_i\mathbf{b}_i$, and $\mathbf{b}_i$ is a reciprocal lattice vector satisfying the condition: $\mathbf{a}_i \cdot \mathbf{b}_i = 2\pi\delta_{ij}$. We now have:

$$\hat{\mathrm{T}}_{\mathbf{R}}\mathbf{H}(\mathbf{r}) = \mathbf{H}(\mathbf{r}+\mathbf{R}) = \mathbf{H}(\mathbf{r})e^{i\boldsymbol{k}\cdot\mathbf{R}} \tag{B.40}$$

This is known as the Bloch-Floquet theorem, which states that for every eigenmode $\mathbf{H}(\mathbf{r})$ there is a wave vector $\boldsymbol{k}$ that ensures any translation by a direct lattice vector $\mathbf{R}$ is equivalent to multiplying the eigenmode by the phase factor $e^{i\boldsymbol{k}\cdot\mathbf{R}}$.[72,73] We can also interpret the Bloch-Floquet theorem in another way, we can equivalently express the eigenmodes as a product of an envelope function $\mathbf{h}_{\boldsymbol{k}}(\mathbf{r})$ that has the same periodicity as the photonic crystal, $\mathbf{h}_{\boldsymbol{k}}(\mathbf{r}) = \mathbf{h}_{\boldsymbol{k}}(\mathbf{r}+\mathbf{R})$, and a plane wave $e^{i\boldsymbol{k}\cdot\mathbf{r}}$, that acts as a phase factor:

$$\mathbf{H}(\mathbf{r}) \equiv \mathbf{H}_{\boldsymbol{k}}(\mathbf{r}) = \mathbf{h}_{\boldsymbol{k}}(\mathbf{r})e^{i\boldsymbol{k}\cdot\mathbf{r}} \tag{B.41}$$

Benchmarking of Crystal Structure Prediction Framework

In order to ensure that the crystal structure prediction machinery implemented in GlOSP works as intended, a general Ewald sum (or accelerated lattice sum) was implemented and used to predict the crystal structures of benzene. In this section we outline the accelerated convergence treatment of lattice sums and present the benchmarking data.

C.1 Acceleration of Lattice Sums

Lattice sums that include long-range interactions require special measures in order to ensure that the sums converge. The generalised Ewald sum is one such method that can be applied to a potential energy function that includes a negative power of distance: z_{ab}^{m}, where m is the exponent. We are considering the interaction between two rigid bodies i and j, with sites a and b respectively. The distance between sites a and b is given by:

$$\mathrm{z}_{ab} = \|\mathbf{z}_i + \boldsymbol{R}_i \cdot \mathbf{z}_a^0 - \mathbf{z}_j - \boldsymbol{R}_j \cdot \mathbf{z}_b^0\| \tag{2.17}$$

where: $\mathbf{z}_i$ is the center of mass of particle i, $\mathbf{z}_a^0$ is the reference position of site a and $\boldsymbol{R}_i$ is the rotation matrix describing the orientation of particle i.

The general premise of the generalised Ewald sum is to decompose the function into two components:

$$U(\mathrm{z}_{ab}) = \frac{1}{2}\sum_{\mathbf{n}}^{*}\sum_{i,j}^{N}\sum_{a,b}^{N_s}\frac{B_{ab}\phi(\mathrm{z}_{ab})}{\mathrm{z}_{ab,\mathbf{n}}^{m}} + \frac{B_{ab}[1-\phi(\mathrm{z}_{ab})]}{\mathrm{z}_{ab,\mathbf{n}}^{m}} \tag{C.1}$$

where $\phi(\mathrm{z}_{ab})$ is known as a convergence function, z_{ab} is the distance between sites a and b of particles i and j, B_{ab} is the potential energy coefficient and (*) indicates that when $\mathbf{n} = 0$ the self-terms with $i = j$ are omitted. The function $\phi(\mathrm{z}_{ab})$ is chosen to be a rapidly converging

function so as to allow the first component of *Eqn.* (C.1) to converge quickly, although the second term still converges slowly. However, the Fourier transform of this second term converges rapidly in reciprocal space. Therefore, we can calculate part of the sum in direct-space, and the other part in reciprocal-space.

The generalised Ewald sum for any inverse power potential depends on a convergence function. The key property of this function is that it converges quickly in real space, and $1-\phi(x)$ converges quickly in reciprocal space. Nijboer and de Wette[126] chose the convergence function to be:

$$\phi(x) = \frac{\Gamma(\frac{m}{2}, \alpha^2 x^2)}{\Gamma(\frac{m}{2})} \tag{C.2}$$

where $\Gamma(w)$ and $\Gamma(w,x)$ are the gamma function and upper incomplete gamma function respectively, the gamma function is the optimal choice for the convergence function.[127] The α parameter is known as the convergence parameter and controls the relative contribution of the two decomposed sums. The gamma function is given by the equations:

$$\Gamma(w) = (w-1)! \tag{C.3}$$

$$\Gamma(w\tfrac{1}{2}) = \frac{(w-2)!!\sqrt{\pi}}{2^{(n-1)/2}} \tag{C.4}$$

The incomplete gamma function can be computed by using the following known values:

$$\Gamma(0,x) = \gamma + ln(x) + \sum_{i}^{\infty} \frac{x^i}{ii!} \tag{C.5}$$

$$\Gamma(\tfrac{1}{2},x) = \sqrt{\pi}\ \mathrm{erfc}(\sqrt{x}) \tag{C.6}$$

$$\Gamma(1,x) = e^{-x} \tag{C.7}$$

where *Eqn.* (C.5) corresponds to the exponential integral, and $\mathrm{erfc}(x)$ is the complementary error function. Using these values, with the following recursive relationships, it is possible to

compute $\Gamma(w, x)$ for integer and half-integer values of w:

$$\Gamma(w+1, x) = w\Gamma(w, x) + x^w e^{-x} \tag{C.8}$$

$$\Gamma(w, x) = \frac{1}{w}\Gamma(w+1, x) - \frac{x^w e^{-x}}{w} \tag{C.9}$$

where *Eqn.* (C.8) is used if w is positive and *Eqn.* (C.9) is used if w is negative.

The derivative of the incomplete gamma function when w is equal to 1 is given by:

$$\frac{\partial\Gamma(1, x)}{\partial x} = -e^{-x} \tag{C.10}$$

This can then be generalised for any value of a with the equation:

$$\frac{\partial\Gamma(w, x)}{\partial x} = -x^{w-1}e^{-x} \tag{C.11}$$

Which we can then use to give an expression for any function of x:

$$\frac{\partial\Gamma(w, x^n)}{\partial x} = (nx^{n-1})(-x^n)^{w-1}(e^{-x^n}) \tag{C.12}$$

Substituting *Eqn.* (C.2) into (C.1) gives us the real-space (U^r) and reciprocal-space (U^f) components of the lattice sum:[128,129]

$$U^r = \frac{1}{2\Gamma(\frac{m}{2})} \sum_{\mathbf{n}}^{*} \sum_{i,j}^{N} \sum_{a,b}^{N_s} B_{ab} \frac{\Gamma(\frac{m}{2}, \alpha^2 \mathrm{z}_{ab,\mathbf{n}}^2)}{\mathrm{z}_{ab,\mathbf{n}}^m} \tag{C.13}$$

$$U^f = \frac{\pi^{3/2}}{2^{m-2}\Gamma(\frac{m}{2})\Omega} \sum_{\mathbf{G}\neq 0} \mathrm{G}^{m-3}\Gamma\left(\frac{3-m}{2}, \frac{\mathrm{G}^2}{4\alpha^2}\right)\left[\sum_{i,j}^{N}\sum_{a,b}^{N_s} B_{ab}\cos(\mathbf{G}\cdot\mathbf{z}_{ab})\right] \tag{C.14}$$

where Ω is the volume of the unit cell and $\mathbf{G}$ is a reciprocal lattice vector. We omit the origin term, $\mathbf{G} = 0$, from the reciprocal space sum, and so calculate it separately as U^0. Additionally, the reciprocal space sum implicitly includes self-interactions, and so we require a correction

term, U^{self}, to ensure that these interactions are deducted from the final sum.

$$U^{self} = -\sum_{i}^{N}\left\{\frac{\alpha^m}{m\Gamma(\frac{m}{2})}\left[\sum_{a}^{N_s} B_{aa}\right] + \frac{1}{2}\sum_{\substack{a,b \\ a\neq b}}^{N_s}\frac{B_{ab}}{z_{ab}^m}\left[1 - \frac{\Gamma(\frac{m}{2}, \alpha^2 z_{ab}^2)}{\Gamma(\frac{m}{2})}\right]\right\} \tag{C.15}$$

$$U^0 = \frac{\pi^{3/2}\alpha^{m-3}}{(m-3)\Gamma(\frac{m}{2})\Omega}\left[\sum_{i,j}^{N}\sum_{a,b}^{N_s} B_{ab}\right] \tag{C.16}$$

When put together the lattice sum takes the form:

$$U = U^r + U^f + U^{self} + U^0 \tag{C.17}$$

C.1.1 Truncation of the Accelerated Lattice Sum

Truncation of the infinite sums can introduce error into the energy and force calculations, and so cannot be chosen arbitrarily. The α parameter controls the convergence properties of the two sums. Given $\Gamma(n, 0) = \Gamma(n)$, we see that, at the limit of $\alpha = 0$, the reciprocal sum is equal to zero. This means that increasing α decreases the contribution of the direct-space sum, and increases that of the reciprocal-space sum (and vice-versa).We calculate α, and the cut-off values for the real-space and reciprocal space sums using:

$$\alpha_{opt} = \left(\frac{\pi^3(N \cdot N_s)}{\Omega^2}\right)^{\frac{1}{3}} \qquad r_{cut} = \frac{f}{\sqrt{\alpha_{opt}}} \qquad \mathrm{G}_{cut} = 2f\sqrt{\alpha_{opt}}$$

where $f = \sqrt{-\ln \varepsilon}$ and ε is the desired accuracy for the sum.

C.1.2 Energy Derivatives

Taking the derivative of the energy with respect to the coordinates of the molecules and the unit cell parameters is required in order to perform local optimisation. We require the derivatives of the lattice energy with respect to the translational and rotational coordinates of the particles, as well as, the derivatives with respect to the lattice parameters. Additionally, we require three sets of derivatives for the direct-space, reciprocal-space and correction terms in the lattice energy. As far as we are aware these derivatives are not given in any other literature for the general Ewald method as applied to rigid body systems, and so we outline them below.

Direct-Space Derivatives

Taking the derivative of the direct-space component of the energy with respect to the translational and rotational coordinates of the molecules is reasonably straightforward:

$$\frac{\partial U^r}{\partial \mathbf{z}_i} = \sum_{\mathbf{n}}^{*} \sum_{j}^{N} \sum_{a,b}^{N_s} \frac{\partial U_i^r}{\partial \mathbf{z}_{ab,\mathbf{n}}} \frac{\partial \mathbf{z}_{ab,\mathbf{n}}}{\partial \mathbf{z}_i} \tag{C.18}$$

$$= \frac{1}{\Gamma(\frac{m}{2})} \sum_{\mathbf{n}}^{*} \sum_{j}^{N} \sum_{a,b}^{N_s} B_{ab} \frac{\Gamma(\frac{m}{2}, \alpha^2 \mathrm{z}_{ab,\mathbf{n}}^2)}{\mathrm{z}_{ab,\mathbf{n}}^m} \frac{\partial}{\partial \mathrm{z}_{ab,\mathbf{n}}} \frac{\partial \mathrm{z}_{ab,\mathbf{n}}}{\partial \mathbf{z}_{ab,\mathbf{n}}} \tag{C.19}$$

Using *Eqn.* (C.12) we see that:

$$\frac{\partial \Gamma(\frac{m}{2}, \alpha^2 \mathrm{z}_{ab,\mathbf{n}}^2)}{\partial \mathrm{z}_{ab,\mathbf{n}}} = (2\alpha^2 \mathrm{z}_{ab,\mathbf{n}}) \Big[- (\alpha^{m-2} \mathrm{z}_{ab,\mathbf{n}}^{m-2}) \exp\Big(-\alpha^2 \mathrm{z}_{ab,\mathbf{n}}^2\Big) \Big] \tag{C.20}$$

The derivative of the lattice energy, for molecule i, with respect to the translational coordinates is then:

$$\frac{\partial U^r}{\partial \mathbf{z}_i} = \frac{-1}{\Gamma(\frac{m}{2})} \sum_{\mathbf{n}}^{*} \sum_{j}^{N} \sum_{a,b}^{N_s} B_{ab} \hat{\mathbf{z}}_{ab,\mathbf{n}} \left[\frac{m\Gamma(\frac{m}{2}, \alpha^2 \mathrm{z}_{ab,\mathbf{n}}^2)}{\mathrm{z}_{ab,\mathbf{n}}^{m+1}} + \frac{2\alpha^m \exp\Big(-\alpha^2 \mathrm{z}_{ab,\mathbf{n}}^2\Big)}{\mathrm{z}_{ab,\mathbf{n}}} \right] \tag{C.21}$$

We can then use *Eqn.* (2.37) to extract the derivatives of the lattice energy with respect to the rotational coordinates:

$$\frac{\partial U^r}{\partial \mathrm{u}_i^k} = \frac{\partial U^r}{\partial \mathbf{z}_{ab,\mathbf{n}}} \frac{\partial \mathbf{z}_{ab,\mathbf{n}}}{\partial \mathrm{u}_i^k} = \frac{\partial U^{\mathrm{r}}}{\partial \mathbf{z}_{ab,\mathbf{n}}} \cdot \left(\mathbf{z}_a^0 \cdot \frac{\partial \boldsymbol{R}_i}{\partial \mathrm{u}_i^k} \right) \tag{C.22}$$

The derivative of the real-space sum with respect to the cell parameters is:

$$\frac{\partial U^r}{\partial \mathbf{p}} = \frac{\partial U^r}{\partial \mathbf{z}_{ab,\mathbf{n}}} \frac{\partial \mathbf{z}_{ab,\mathbf{n}}}{\partial \mathbf{p}} \tag{C.23}$$

$$= \frac{-1}{2\Gamma(\frac{m}{2})} \sum_{\mathbf{n}}^{*} \sum_{i,j}^{N} \sum_{a,b}^{N_s} B_{ab} \hat{\mathbf{z}}_{ab,\mathbf{n}} \left[\frac{m\Gamma(\frac{m}{2}, \alpha^2 \mathrm{z}_{ab,\mathbf{n}}^2)}{\mathrm{z}_{ab,\mathbf{n}}^{m+1}} + \frac{2\alpha^m \exp\Big(-\alpha^2 \mathrm{z}_{ab,\mathbf{n}}^2\Big)}{\mathrm{z}_{ab,\mathbf{n}}} \right] \cdot \left(\frac{\partial \mathbf{A}}{\partial \mathbf{p}} \cdot \mathbf{n} \right) \tag{C.24}$$

where the derivatives of the cell matrix, $\mathbf{A}$, with respect to the lattice parameters, $\mathbf{p}$, is given in **Table** 2.1.

Reciprocal-Space Derivatives

The derivatives of the reciprocal-space term in the lattice energy, with respect to the translational and rotational coordinates of the molecules are:

$$\frac{\partial U^f}{\partial \mathbf{z}_{ab,\mathbf{n}}} = -\frac{\pi^{3/2}}{2^{m-3}\Gamma(\frac{m}{2})\Omega}\sum_{\mathbf{G}\neq 0}\mathrm{G}^{m-3}\Gamma\left(\frac{3-m}{2},\frac{\mathrm{G}^2}{4\alpha^2}\right)\left[\sum_j^N\sum_{a,b}^{N_s}B_{ab}\sin(\mathbf{G}\cdot\mathbf{z}_{ab})\mathbf{G}\right] \tag{C.25}$$

$$\frac{\partial U^f}{\partial \mathrm{u}_i^k} = \frac{\partial U^f}{\partial \mathbf{z}_{ab,\mathbf{n}}}\cdot\left(\mathbf{z}_a^0\cdot\frac{\partial \boldsymbol{R}_i}{\partial \mathrm{u}_i^k}\right) \tag{C.26}$$

The derivative of the reciprocal-space sum with respect to the cell parameters is:

$$\frac{\partial U^f}{\partial \mathbf{p}} = \frac{\partial U^f}{\partial \Omega}\frac{\partial \Omega}{\partial \mathbf{p}} + \frac{\partial U^f}{\partial \mathbf{G}}\frac{\partial \mathbf{G}}{\partial \mathbf{p}} \tag{C.27}$$

Given that we also have:

$$\frac{\partial \mathrm{G}^{m-3}}{\partial \mathbf{G}} = (m-3)(\mathrm{G}^{m-5})\mathbf{G} \tag{C.28}$$

$$\frac{\partial \Gamma(\frac{3-m}{2},\frac{\mathrm{G}^2}{4\alpha^2})}{\partial \mathbf{G}} = \left(\frac{1}{2\alpha^2}\right)\left(\frac{\mathrm{G}}{2\alpha}\right)^{1-m}\exp\left(-\frac{\mathrm{g}^2}{4\alpha^2}\right)\mathbf{G} \tag{C.29}$$

We can write the derivative of the reciprocal-space term with respect to the cell parameters as:

$$\begin{aligned}\frac{\partial U^f}{\partial \mathbf{p}} = \\ \frac{-U^f}{\Omega}\frac{\partial \Omega}{\partial \mathbf{p}} + \frac{\pi^{3/2}}{2^{m-2}\Gamma(\frac{m}{2})\Omega}\sum_{\mathbf{G}\neq 0}\sum_{i,j}^{N}\sum_{a,b}^{N_s}B_{ab}\mathrm{G}^{m-3}\Bigg\{\cos(\mathbf{G}\cdot\mathbf{z}_{ab})\Bigg[\left(\frac{(m-3)\mathbf{G}}{\mathrm{G}^2}\right)\Gamma\left(\frac{3-m}{2},\frac{\mathrm{G}^2}{4\alpha^2}\right)- \\ \left(\frac{1}{2\alpha^2}\right)\left(\frac{\mathrm{G}}{2\alpha}\right)^{1-m}\exp\left(-\frac{\mathrm{G}^2}{4\alpha^2}\right)\mathbf{G}\Bigg] - \sin(\mathbf{G}\cdot\mathbf{z}_{ab})\mathbf{z}_{ab}\Gamma\left(\frac{3-m}{2},\frac{\mathrm{G}^2}{4\alpha^2}\right)\Bigg\}\cdot\frac{\partial \mathbf{G}}{\partial \mathbf{p}}\end{aligned} \tag{C.30}$$

For a given lattice vector, $\mathbf{R} = \mathbf{A}\cdot\mathbf{n}$, the corresponding reciprocal lattice vector is given by:

$$\mathbf{G} = 2\pi\mathbf{A}^{-1}\cdot\mathbf{n} \tag{C.31}$$

Therefore the partial derivative of a given reciprocal lattice vector with respect to the cell parameters is:

$$\frac{\partial \mathbf{G}}{\partial \mathbf{p}} = 2\pi \left(\frac{\partial \mathbf{A}^{-1}}{\partial \mathbf{p}} \right) \cdot \mathbf{n} \tag{C.32}$$

where the derivatives of the inverse cell matrix with respect to the cell parameters are:

$$\frac{\partial \mathbf{A}^{-1}}{\partial \mathrm{a}_1} = \begin{bmatrix} \frac{1}{\mathrm{a}_1^2} & -\frac{\cos\gamma}{\mathrm{a}_1^2 \sin\gamma} & -\frac{\cos\beta - \cos\alpha\cos\gamma}{\mathrm{a}_1^2 \sqrt{W}\sin\gamma} \\ 0 & 0 & 0 \\ 0 & 0 & 0 \end{bmatrix} \qquad \frac{\partial \mathbf{A}^{-1}}{\partial \mathrm{a}_2} = \begin{bmatrix} 0 & 0 & 0 \\ 0 & \frac{1}{\mathrm{a}_2^2 \sin\gamma} & -\frac{\cos\alpha - \cos\beta\cos\gamma}{\mathrm{a}_2^2 \sqrt{W}\sin\gamma} \\ 0 & 0 & 0 \end{bmatrix}$$

$$\frac{\partial \mathbf{A}^{-1}}{\partial \mathrm{a}_3} = \begin{bmatrix} 0 & 0 & 0 \\ 0 & 0 & 0 \\ 0 & 0 & \frac{\sin\gamma}{\mathrm{a}_3^2 \sqrt{W}} \end{bmatrix}$$

$$\frac{\partial \mathbf{A}^{-1}}{\partial \alpha} = \begin{bmatrix} 0 & 0 & \frac{(\sin\alpha\sin\gamma)(\cos\gamma - \cos\alpha\cos\beta)}{\mathrm{a}_1 W^{\frac{3}{2}}} \\ 0 & 0 & \frac{-(\sin\alpha\sin\gamma)(\sin^2\beta\sin\gamma)}{\mathrm{a}_2 W^{\frac{3}{2}}} \\ 0 & 0 & \frac{(\sin\alpha\sin\gamma)(\cos\alpha - \cos\beta\cos\gamma)}{\mathrm{a}_3 W^{\frac{3}{2}}} \end{bmatrix} \qquad \frac{\partial \mathbf{A}^{-1}}{\partial \beta} = \begin{bmatrix} 0 & 0 & \frac{-(\sin\beta\sin\gamma)(\sin^2\alpha\sin\gamma)}{\mathrm{a}_1 W^{\frac{3}{2}}} \\ 0 & 0 & \frac{(\sin\beta\sin\gamma)(\cos\gamma - \cos\alpha\cos\beta)}{\mathrm{a}_2 W^{\frac{3}{2}}} \\ 0 & 0 & \frac{(\sin\beta\sin\gamma)(\cos\beta - \cos\alpha\cos\gamma)}{\mathrm{a}_3 W^{\frac{3}{2}}} \end{bmatrix}$$

$$\frac{\partial \mathbf{A}^{-1}}{\partial \gamma} = \begin{bmatrix} 0 & \frac{1}{\mathrm{a}_1 \sin^2\gamma} & \frac{(\cos\alpha - \cos\beta\cos\gamma)}{\mathrm{a}_1\sqrt{W}\sin^2\gamma} - \frac{(\cos\beta - \cos\alpha\cos\gamma)(\cos\gamma - \cos\alpha\cos\beta)}{\mathrm{a}_1 W^{\frac{3}{2}}} \\ 0 & \frac{\cos\gamma}{\mathrm{a}_2 \sin^2\gamma} & \frac{(\cos\beta - \cos\alpha\cos\gamma)}{\mathrm{a}_2\sqrt{W}\sin^2\gamma} - \frac{(\cos\alpha - \cos\beta\cos\gamma)(\cos\gamma - \cos\alpha\cos\beta)}{\mathrm{a}_2 W^{\frac{3}{2}}} \\ 0 & 0 & \frac{\cos\gamma}{\mathrm{a}_3\sqrt{W}} - \frac{(\cos\gamma - \cos\alpha\cos\beta)\sin^2\gamma}{\mathrm{a}_3 W^{\frac{3}{2}}} \end{bmatrix}$$

Table C.1: Derivatives of the inverse cell matrix with respect to cell lengths, $\{\mathrm{a}_1, \mathrm{a}_2, \mathrm{a}_3\}$, and the cell angles $\{\alpha, \beta, \gamma\}$

Correction Terms Derivatives

The self term, U^{self}, accounts for only intra-molecular interactions and as a result its value does not change during the optimisation process. The charged system term, U^0, is also independent of the position of the molecules in the crystal, however it does depend on the volume of the unit cell. As a result its derivative with respect to the cell parameters must be evaluated:

$$\frac{\partial U^0}{\partial \mathbf{p}} = \frac{U^0}{\Omega}\frac{\partial \Omega}{\partial \mathbf{p}} \tag{C.33}$$

The derivatives of the reciprocal space term and the charged system term both require the partial derivative of the volume of the unit cell with respect to the cell parameters. These are given by:[11]

$$\frac{\partial \Omega}{\partial \mathrm{a}_l} = \frac{\Omega}{\mathrm{a}_l} \tag{C.34}$$

$$\frac{\partial \Omega}{\partial \omega_i} = \frac{\Omega[\sin\omega_i(\cos\omega_i - \cos\omega_j\cos\omega_k)]}{W} \tag{C.35}$$

where $\omega_i, \omega_j, \omega_k \in \{\alpha, \beta, \gamma\}$, $i \neq j \neq k$ and $l \in \{1, 2, 3\}$.

C.2 Crystal Structures of Benzene

The crystal structures of benzene have been well studied with multiple models, and so is an ideal system to benchmark the crystal structure prediction code. We chose to use the simple rigid body model given by Williams and Starr[130], where the pair potential is given by:

$$U(\mathrm{z}_{ab}) = B_{ab}\exp\{(-C_{ab}\mathrm{z}_{ab})\} - \frac{A_{ab}}{\mathrm{z}_{ab}^6} + \frac{q_a q_b}{\mathrm{z}_{ab}} \tag{C.36}$$

These parameters were generated through empirically fitting of structural data. A list of hypothetical benzene structures has previously been generated using this model and energy minimisation.[131] 30 structures were found at zero pressure, with the lattice energy, spacegroup and cell parameters provided for each structure.

	A	B	C
C-C	2414	367,250	3.60
H-H	136	11,677	3.74
C-H	573	65,485	3.67

q_C = -q_H = -0.153e

Table C.2: Williams and Starr (1977)[130] force field parameters.

Basin-hopping global optimisation, using the L-BFGS local minimiser, was performed using this system where the exponent-6 term and Coulomb term were both evaluated using the Ewald method outlined above, and the exponential term was calculated by the direct sum method. A single run of 10,000 Monte-Carlo steps was performed with four molecules in the unit cell, starting from a random initial configuration. The lowest 500 minima were saved and then the spacegroups and conventional unit cells of those minima were determined using `spglib`. A list of unique minima was then generated and compared to the minima provided in by van Eijck *et. al.*, that we will refer to as the literature values from now on. The comparison between minima found using `GlOSP` and the literature values is provided in **Table** C.3. Of the 30 literature minima, 20 were found during the short basin-hopping simulation. Only these 20 minima are tabulated in **Table** C.3, where we see that the spacegroups and lattice parameters for these minima are exactly the same (with the exception of a few cell parameters differing by 0.01 Å or 0.01°) with the literature values. However, there is a slight difference in the lattice energies. This is most likely due to the energy minimisation in the literature being discontinued when the magnitude of the gradient is less than 1×10^3 kJ mol^{-1} Å^{-1}, whereas each minimisation step in `GlOSP` is considered as converged when the root mean square difference (RMSD) of the magnitude of the gradient is less than 1×10^6 kJ mol^{-1} Å^{-1}. Additionally, a visualisation of Benzene I is provided in **Figure** C.1, as given by `GlOSP`. It is clear from this that we are able to realiably predict potential crystal structures of rigid body systems using `GlOSP`, and extract the spacegroups and primitive/conventional unit cell parameters for those structures using `spglib`.

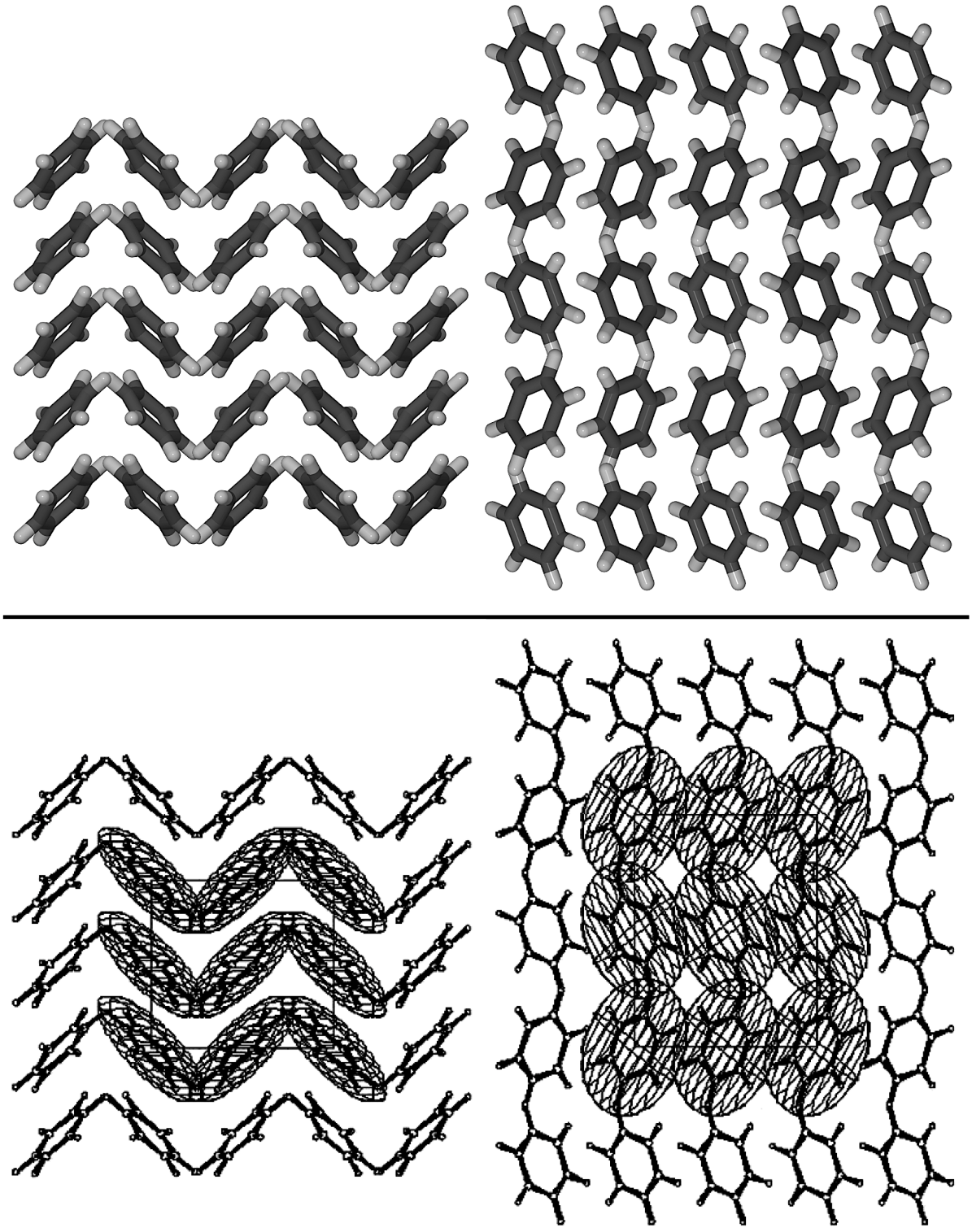

Figure C.1: (**top**) The predicted global minimum of benzene using the `GlOSP`. (**bottom**) An image of the crystal structure of benzene from ref. [132].

Literature								GlOSP							
U/kJ·mol^{-1}		a_1/Å	a_2/Å	a_3/Å	α / °	β / °	γ / °	U/kJ·mol^{-1}		a_1/Å	a_2/Å	a_3/Å	α/°	β/°	γ/°
-52.25	Pbca	6.98	7.43	9.28	90	90	90	-52.30	Pbca	6.98	7.42	9.28	90	90	90
-51.96	$P2_1/c$	5.71	6.94	7.20	90	123	90	-52.01	$P2_1/c$	5.71	6.94	7.20	90	123	90
-51.32	$P2_1/c$	5.54	5.57	8.01	90	108	90	-51.37	$P2_1/c$	5.54	5.57	8.01	90	108	90
-51.14	$P4_32_12$	5.54	5.54	15.32	90	90	90	-51.18	$P4_32_12$	5.54	5.54	15.32	90	90	90
-50.69	$Pca2_1$	9.94	5.42	8.94	90	90	90	-50.72	$Pca2_1$	9.94	5.42	8.94	90	90	90
-50.01	C2/c	21.63	5.62	7.85	90	93	90	-52.06	C2/c	21.62	5.62	7.85	90	93	90
-49.74	Pbcn	5.62	11.38	7.46	90	90	90	-49.78	Pbcn	5.62	11.38	7.46	90	90	90
-49.51	C2/c	11.74	5.56	7.99	90	113	90	-49.55	C2/c	11.74	5.56	7.99	90	113	90
-48.85	$P2_12_12_1$	5.65	13.22	6.54	90	90	90	-48.90	$P2_12_12_1$	5.65	6.54	13.22	90	90	90
-48.31	Pbca	5.60	8.19	10.66	90	90	90	-48.35	Pbca	5.60	8.19	10.66	90	90	90
-48.31	$C222_1$	5.64	11.51	7.46	90	90	90	-48.35	$C222_1$	5.63	11.51	7.46	90	90	90
-47.68	C2/c	21.82	5.73	7.89	90	98	90	-47.76	C2/c	21.82	5.73	7.88	90	98	90
-46.50	$Pna2_1$	7.32	9.93	6.76	90	90	90	-46.54	$Pna2_1$	7.32	9.92	6.76	90	90	90
-46.47	$P2_1/c$	5.41	15.10	6.81	90	119	90	-46.52	$P2_1/c$	5.41	15.10	6.80	90	120	90
-46.15	$P2_1/c$	6.81	7.44	11.88	90	125	90	-46.20	$P2_1/c$	6.81	7.44	11.88	90	125	90
-45.79	C2/c	11.69	5.53	16.35	90	108	90	-45.84	C2/c	11.69	5.53	16.35	90	108	90
-45.49	$R\bar{3}$	6.74	6.74	9.36	90	90	120	-45.52	$R\bar{3}$	6.73	6.73	9.36	90	90	120
-45.42	$P2_1/c$	5.44	5.45	17.43	90	105	90	-45.47	$P2_1/c$	5.44	5.44	17.43	90	105	90
-44.59	$P\bar{1}$	5.03	5.11	10.17	100	101	98	-44.63	$P\bar{1}$	5.03	5.11	10.17	100	101	98

Table C.3: Comparison of the minima given by van Eijck *et. al.*[131] and the corresponding minima found using GlOSP. The lattice energy, spacegroups and cell parameters are provided in the table.

Benchmarking of Photonic Band Structure Calculations

In order to make sure that the pipeline of `GlOSP` → `spglib` → `MPB` provides the correct final output, we decided to reproduce band structures that have previously been reported in literature.

D.1 Band Structure of Inverse Opals

Initially we reproduced the band structures for the inverse fcc[16] and hcp[133] structures to make sure that both cubic and hexagonal structures are properly represented within the MIT `MPB` framework. The generalised Lennard-Jones pair potential was implemented in `GlOSP`, using the Ewald summation framework outlined in **Appendix** C:

$$U(\mathrm{z}_{ij}) = 2\epsilon_{ij} \sum_{\mathbf{n}}^{*} \sum_{i,j}^{N} \left[\left(\frac{\sigma_{ij}}{\mathrm{z}_{ij}} \right)^{2m} - \left(\frac{\sigma_{ij}}{\mathrm{z}_{ij}} \right)^{m} \right] \tag{D.1}$$

where, ϵ_{ij} and σ_{ij} are the well-depth and the distance at which the pair potential is zero. They satisfy the combination rules: $\sqrt{\epsilon_{ii}\epsilon_{jj}}$ and $(\sigma_{ii} + \sigma_{jj})/2$, and we set $\epsilon_{ii} = \epsilon_{jj} = 1$ and $\sigma_{ii} = \sigma_{jj} = 1$. First we performed basin-hopping global optimisation with $m = 6$, and with two particles in the unit cell ($Z = 2$), in order to benchmark the implementation. The lowest two minima were found to be the hcp and fcc structures, whose lattice energies are shown in **Table** D.1 and agree with those previously reported by Stillinger.[134]

Structure	$U\,/\,Z$
hcp	-8.61107
fcc	-8.61020

Table D.1: Dimensionless lattice energies for the hcp and fcc structures as extracted from `GlOSP`. The values agree well with those previously reported in ref. [134]

As the Lennard-Jones exponent, m, tends to infinity we approach the hard-sphere limit. However, a value of $m = 60$ provides a close enough approximation to hard-spheres. The hcp and fcc structures found for $m = 6$ were used as seeds for short global optimisation runs with $m = 60$. The primitive and conventional unit cells for the "hard-sphere" hcp and fcc structures were then extracted using `spglib` and used to set up the scripts to calculate the band structures for their inverse structures using the MIT `MPB` package.

The radii of the spheres in both calculations were set to $r = \mathrm{a}_{fcc}/\sqrt{8}$, where a_{fcc} is the cell length of the conventional unit cell of fcc. This corresponds to the close-packing limit where the spheres are touching and both structures have a volume fraction of $\sim 74\%$. The dielectric constant of the spheres was then set to $\varepsilon_b = 1$ and the background medium was set to $\varepsilon_a = 13$ for the inverse fcc structure[16] and $\varepsilon_a = 11.9$ for the inverse hcp structure,[133] resulting in two lattices composed of air spheres, that are just touching, embedded in a dielectric medium. The frequencies are reported in the reduced units of $\omega \mathrm{a}/2\pi c$, where $\mathrm{a} = \|\mathbf{a}_1\|$ for each of the respective structures (i.e., for the fcc structure $\mathrm{a} = \mathrm{a}_{fcc}$).

The band structure of the inverse fcc structure is shown in **Figure** D.1. There is band gap between the 8th and 9th bands, which has a midgap ratio of $\Delta\omega/\omega_m = 6.1\%$. The band structure is identical to that given on page 104 of ref. [16]. The band structure calculated for the inverse hcp structure is shown in **Figure** D.2, and agrees well with the band structure given in ref. [133], with both showing a complete band gap between the 16th and 17th bands. However, there is a slight discrepancy between the size of the band gap quoted in ref. [133] (2.8%) and that calculated here (4.1%).

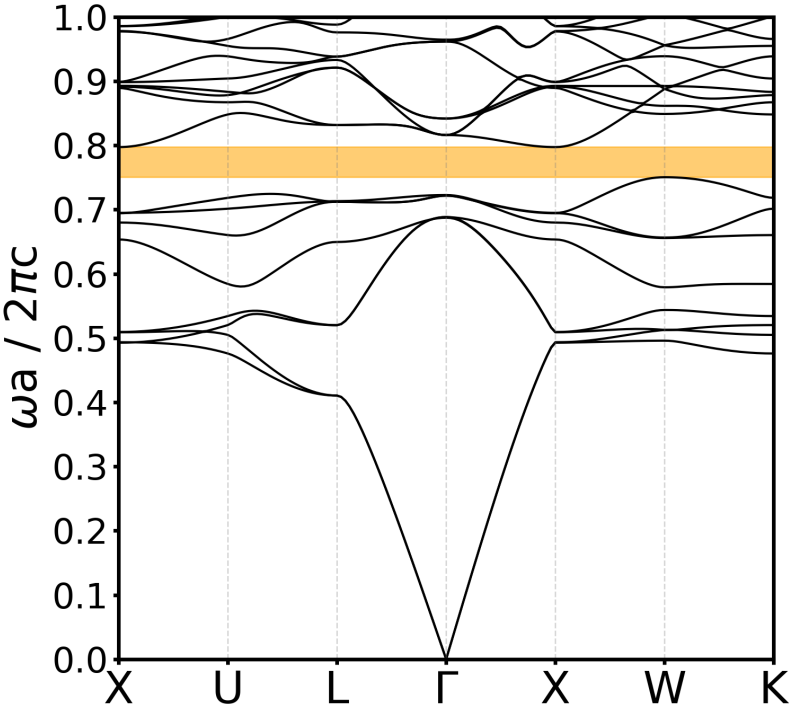

Figure D.1: The photonic band structure of a face-centred cubic lattice of air spheres embedded in a high dielectric medium of $\varepsilon = 13$.

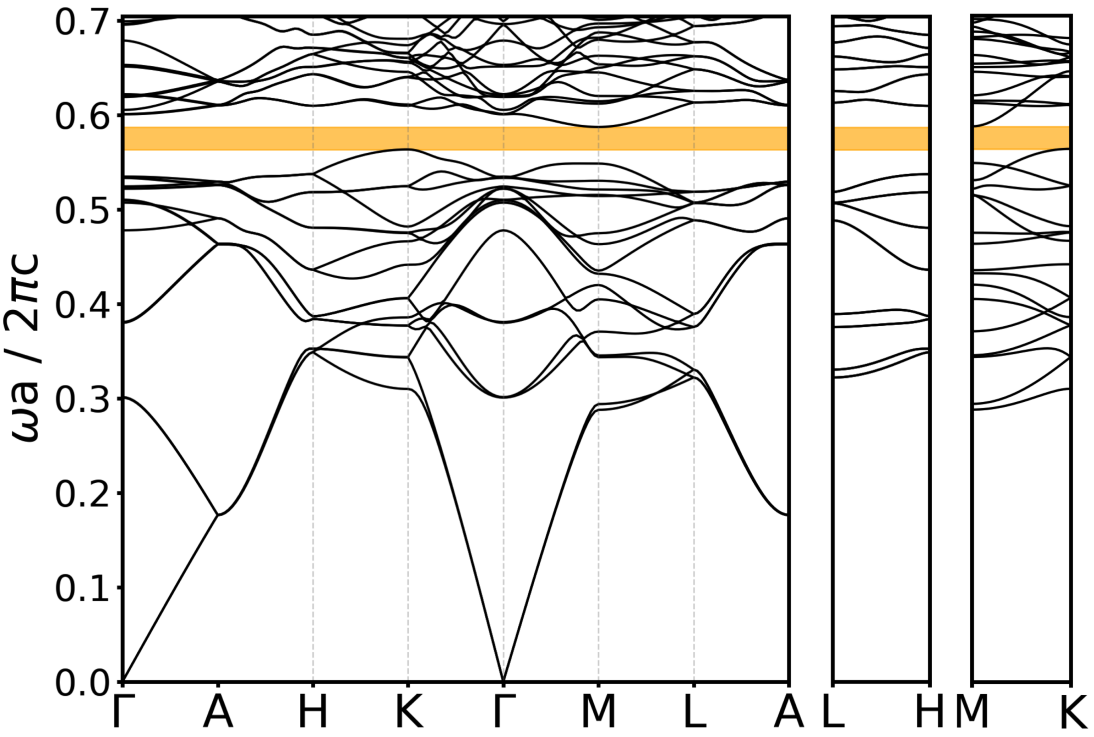

Figure D.2: The photonic band structure of a hexagonal close-packed lattice of air spheres embedded in a high dielectric medium of $\varepsilon = 11.9$.

D.2 Band Structure of Cubic Tetrastack

The photonic properties of the cubic tetrastack structure, with spherical particles, is well known. The band structures for the direct and inverse cubic tetrastack structures are reported in the supplementary information of Ref. [63]. Using `GlOSP`, and the patchy rod model with $L^* = 0$, $\epsilon_{AA} = \epsilon_{BB} = 5$ and $\alpha = \beta = 85°$, the cubic tetrastack structure was extracted. Then `spglib` was used to find the primitive and conventional unit cell parameters and the fractional coordinates of the particles in order to set up the band structure calculations using `MPB`. The diameter of the particles were set to:

$$\sigma = \left(\frac{\rho^* \cdot \mathrm{a}^3}{16} \right)^{1/3} \tag{D.2}$$

where, a is the edge length of the conventional unit cell and ρ^* is the reduced density of the system. In order to match the calculations for Ref. [63] we set $\rho^* = 0.87$ for the direct structure, and $\rho^* = 2.52$ for the inverse structure. The frequency is given in the reduced units of $\omega \mathrm{a}/2\pi c$, and again the band structures calculated using the output for `GlOSP` and `spglib` match up well with those previously reported in the literature.

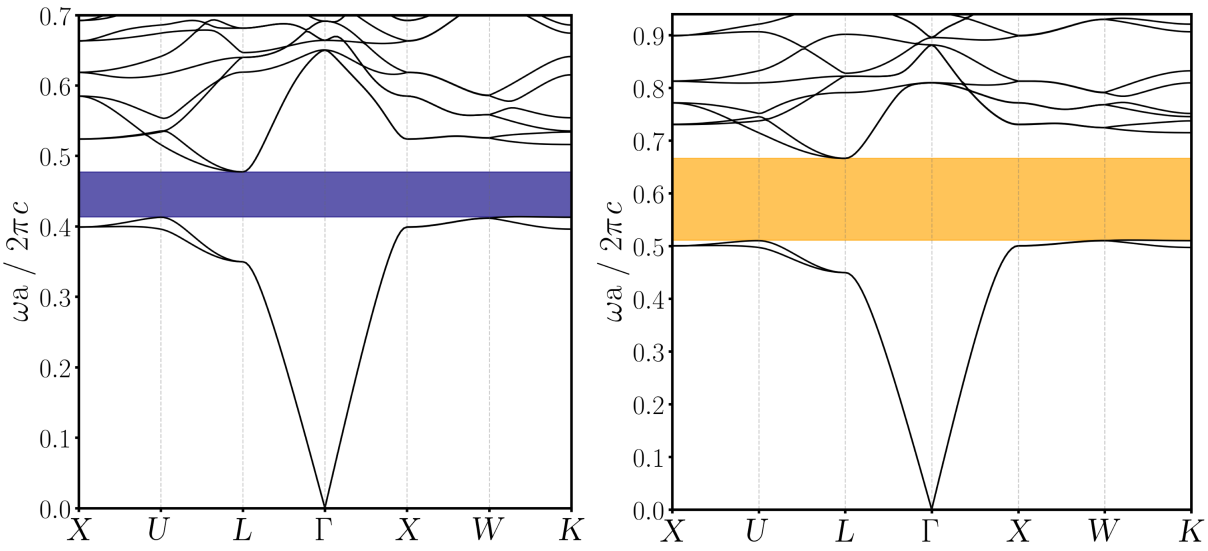

Figure D.3: (**left**) The photonic band structure of the direct cubic tetrastack structure with $\varepsilon = 12$. (**right**) The photonic band structure of the inverse cubic tetrastack structure with $\varepsilon = 12$.

Bibliography

[1] E. Yablonovitch and T. J. Gmitter, "Photonic band structure: The face-centered-cubic case," *Phys. Rev. Lett.*, vol. 63, pp. 1950–1953, 1989. DOI: 10.1103/PhysRevLett.63.1950.

[2] K. M. Leung and Y. F. Liu, "Full vector wave calculation of photonic band structures in face-centered-cubic dielectric media," *Phys. Rev. Lett.*, vol. 65, pp. 2646–2649, 1990. DOI: 10.1103/PhysRevLett.65.2646.

[3] Z. Zhang and S. Satpathy, "Electromagnetic wave propagation in periodic structures: Bloch wave solution of maxwell's equations," *Phys. Rev. Lett.*, vol. 65, pp. 2650–2653, 1990. DOI: 10.1103/PhysRevLett.65.2650.

[4] L. Rayleigh, "On the maintenance of vibrations by forces of double frequency, and on the propagation of waves through a medium endowed with a periodic structure," *Philosophical Magazine*, vol. 24, pp. 145–159, 1887.

[5] E. Yablonovitch, "Inhibited spontaneous emission in solid-state physics and electronics," *Phys. Rev. Lett.*, vol. 58, pp. 2059–2062, 1987. DOI: 10.1103/PhysRevLett.58.2059.

[6] S. John, "Strong localization of photons in certain disordered dielectric superlattices," *Phys. Rev. Lett.*, vol. 58, pp. 2486–2489, 1987. DOI: 10.1103/PhysRevLett.58.2486.

[7] E. Yablonovitch, T. J. Gmitter, and K. M. Leung, "Photonic band structure: The face-centered-cubic case employing nonspherical atoms," *Phys. Rev. Lett.*, vol. 67, p. 2295, 1991. DOI: 10.1103/PhysRevLett.67.2295.

[8] S. Noda, K. Tomoda, N. Yamamoto, and A. Chutinan, "Full three-dimensional photonic bandgap crystals at near-infrared wavelengths," *Science*, vol. 289, pp. 604–606, 2000. DOI: 10.1126/science.289.5479.604.

[9] H. Han, S. Vijayalakshmi, A. Lan, *et al.*, "Linear and nonlinear optical properties of single-walled carbon nanotubes within an ordered array of nanosized silica spheres," *App. Phys. Lett.*, vol. 82, pp. 1458–1460, 2003. DOI: 10.1063/1.1557322.

[10] I. S. Nefedov, V. N. Gusyatnikov, and Y. A. Morozov, "Optical switching in semiconductor photonic band gap structures," *ICTON 2001*, pp. 275–278, 2001. DOI: 10.1109/ICTON.2001.934769.

[11] T. G. Euser, H. Wei, J. Kalkman, *et al.*, "Ultrafast all-optical switching of 3d photonic band gap crystals," *Proc. SPIE*, vol. 6640, pp. 6640–6644, 2007. DOI: 10.1117/12.737495.

[12] K. Lee and S. A. Asher, "Photonic crystal chemical sensors: Ph and ionic strength," *J. Am. Chem. Soc.*, vol. 122, pp. 9534–9537, 2000. DOI: 10.1021/ja002017n.

[13] S. A. Asher, A. C. Sharma, A. V. Goponenko, and M. M. Ward, "Photonic crystal aqueous metal cation sensing materials," *Anal. Chem.*, vol. 75, pp. 1676–1683, 2003. DOI: 10.1021/ac026328n.

[14] V. L. Alexeev, A. C. Sharma, A. V. Goponenko, *et al.*, "High ionic strength glucose-sensing photonic crystal," *Anal. Chem.*, vol. 75, pp. 2316–2323, 2003. DOI: 10.1021/ac030021m.

[15] V. L. Alexeev, S. Das, D. N. Finegold, and S. A. Asher, "Photonic crystal glucose-sensing material for noninvasive monitoring of glucose in tear fluid," *Clin. Chem.*, vol. 50, pp. 2353–2360, 2004. DOI: 10.1373/clinchem.2004.039701.

[16] J. D. Joannopoulos, S. G. Johnson, J. N. Winn, and R. D. Meade, *Photonic Crystals: Molding the Flow of Light. second edition*, P. U. Press, Ed. 2008.

[17] K. M. Ho, C. T. Chan, and C. M. Soukoulis, "Existence of a photonic gap in periodic dielectric structures," *Phys. Rev. Lett.*, vol. 65, pp. 3152–3155, 1990. DOI: 10.1103/PhysRevLett.65.3152.

[18] H. S. Sözüer, J. W. Haus, and R. Inguva, "Photonic bands: Convergence problems with the plane-wave method," *Phys. Rev. B*, vol. 45, p. 13 962, 1992. DOI: 10.1103/PhysRevB.45.13962.

[19] H. Men, K. Y. K. Lee, R. M. Freund, J. Peraire, and S. G. Johnson, "Robust topology optimization of three-dimensional photonic-crystal band-gap structures," *Opt. Express*, vol. 22, pp. 22 632–22 648, 2014. DOI: 10.1364/OE.22.022632.

[20] M. Maldovan and E. L. Thomas, "Diamond-structured photonic crystals," *Nat. Mater.*, vol. 3, p. 593, 2004.

[21] K. Edagawa, S. Kanoko, and M. Notomi, "Photonic amorphous diamond structure with a 3d photonic band gap," *Phys. Rev. Lett.*, vol. 100, p. 013 901, 2008. DOI: 10.1103/PhysRevLett.100.013901.

[22] S. F. Liew, J.-K. Yang, H. Noh, *et al.*, "Photonic band gaps in three-dimensional network structures with short-range order," *Phys. Rev. A*, vol. 84, p. 063 818, 2011. DOI: 10.1103/PhysRevA.84.063818.

[23] S. R. Sellers, W. Man, S. Sahba, and M. Florescu, "Local self-uniformity in photonic networks," *Nat. Commun.*, vol. 8, p. 14 439, 2017. DOI: 10.1038/ncomms14439.

[24] M. Maldovan, C. K. Ullal, C. W. Carter, and E. L. Thomas, "Exploring for 3d photonic bandgap structures in the 11 fcc space groups," *Nat. Mater.*, vol. 2, p. 664, 2003. DOI: 10.1038/nmat979.

[25] H. Yin, B. Dong, X. Liu, *et al.*, "Amorphous diamond-structured photonic crystal in the feather barbs of the scarlet macaw," *Proc. Natl. Acad. Sci. U.S.A.*, vol. 109, pp. 10 798–10 801, 2012. DOI: 10.1073/pnas.1204383109.

[26] G. M. Whitesides and B. Grzybowski, "Self-assembly at all scales," *Science*, vol. 295, p. 2418, 2002. DOI: 10.1126/science.1070821.

[27] A. van Blaaderen, "From the de broglie to visible wavelengths: Manipulating electrons and photons with colloids," *MRS Bulletin*, vol. 23, pp. 39–43, 1998. DOI: 10.1557/S0883769400029584.

[28] R. A. L. Jones, *Soft condensed matter*. Oxford University Press, 2002, vol. 6.

[29] R. Brown, "On the particles contained in the pollen of plants; and on the general existence of active molecules in organic and inorganic bodies," *The Philosophical Magazine*, vol. 4, pp. 161–173, 1828.

[30] A. Einstein, "Über die von der molekularkinetischen theorie der wärme geforderte bewegung von in ruhenden flüssigkeiten suspendierten teilchen," *Ann. Phys.*, vol. 322, pp. 549–560, 1905.

[31] M. J. Perrin, *Brownian Movement and Molecular Reality: Translated from the Annales de Chimie Et de Physique, 8 Series, September 1909, by F. Soddy*. Taylor & Francis, 1910.

[32] V. L. Colvin, "From opals to optics: Colloidal photonic crystals," *MRS Bulletin*, vol. 26, pp. 637–641, 2001. DOI: 10.1557/mrs2001.159.

[33] R. Biswas, M. M. Sigalas, G. Subramania, C. M. Soukoulis, and K.-M. Ho, "Photonic band gaps of porous solids," *Phys. Rev. B*, vol. 61, p. 4549, 2000. DOI: 10.1103/PhysRevB.61.4549.

[34] L. V. Woodcock, "Entropy difference between the face-centred cubic and hexagonal close-packed crystal structures," *Nature*, vol. 385, pp. 141–143, 1997. DOI: 10.1038/385141a0.

[35] P. G. Bolhuis, D. Frenkel, S.-C. Mau, and D. A. Huse, "Entropy difference between crystal phases," *Nature*, vol. 388, pp. 235–236, 1997. DOI: 10.1038/40779.

[36] P. Vukusic, J. R. Sambles, C. R. Lawrence, and R. J. Wootton, "Quantified interference and diffraction in single morpho butterfly scales," *Proc. Royal Soc. Lond. B*, vol. 266, pp. 1403–1411, 1999. DOI: 10.1098/rspb.1999.0794.

[37] G. M. Whitesides and M. Boncheva, "Beyond molecules: Self-assembly of mesoscopic and macroscopic components," *Proc. Natl. Acad. Sci. USA*, vol. 99, p. 4769, 2002. DOI: 10.1073/pnas.082065899.

[38] S. C. Glotzer and M. J. Solomon, "Anisotropy of building blocks and their assembly into complex structures," *Nat. Mater.*, vol. 6, pp. 557–562, 2007. DOI: 10.1038/nmat1949.

[39] L. Cademartiri and K. J. M. Bishop, "Programmable self-assembly," *Nat. Mater.*, vol. 14, pp. 2–9, 2015.

[40] S. Ravaine and E. Duguet, "Synthesis and assembly of patchy particles: Recent progress and future prospects," *Curr. Opin. Colloid Interface Sci.*, vol. 30, pp. 45–53, 2017. DOI: 10.1016/j.cocis.2017.05.002.

[41] E. Bianchi, R. Blaak, and C. N. Likos, "Patchy colloids: State of the art and perspectives," *Phys. Chem. Chem. Phys.*, vol. 13, pp. 6397–6410, 2011. DOI: 10.1039/C0CP02296A.

[42] Y. Wang, Y. Wang, D. R. Breed, *et al.*, "Colloids with valence and specific directional bonding," *Nature*, vol. 490, 2012. DOI: 10.1038/nature11564.

[43] Z. Zhang, A. S. Keys, T. Chen, and S. C. Glotzer, "Self-assembly of patchy particles into diamond structures through molecular mimicry," *Langmuir*, vol. 21, pp. 11 547–11 551, 2005. DOI: 10.1021/la0513611.

[44] F. Romano, E. Sanz, and F. Sciortino, "Phase diagram of a tetrahedral patchy particle model for different interaction ranges," *J. Chem. Phys*, vol. 132, p. 184 501, 2010. DOI: 10.1063/1.3393777.

[45] E. G. Noya, C. Vega, J. P. K. Doye, and A. A. Louis, "The stability of a crystal with diamond structure for patchy particles with tetrahedral symmetry," *J. Chem. Phys*, vol. 132, p. 234 511, 2010. DOI: 10.1063/1.3454907.

[46] F. Romano, E. Sanz, and F. Sciortino, "Crystallization of tetrahedral patchy particles in silico," *J. Chem. Phys*, vol. 134, p. 174 502, 2011. DOI: 10.1063/1.3578182.

[47] F. Romano, J. Russo, and H. Tanaka, "Influence of patch-size variability on the crystallization of tetrahedral patchy particles," *Phys. Rev. Lett.*, vol. 113, p. 138 303, 2014. DOI: 10.1103/PhysRevLett.113.138303.

[48] Z. Gong, T. Hueckel, G.-R. Yi, and S. Sacanna, "Patchy particles made by colloidal fusion," *Nature*, vol. 550, p. 234, 2017.

[49] A. B. Pawar and I. Kretzschmar, "Patchy particles by glancing angle deposition," *Langmuir*, vol. 24, pp. 355–358, 2008. DOI: 10.1021/la703005z.

[50] Q. Chen, S. C. Bae, and S. Granick, "Directed self-assembly of a colloidal kagome lattice," *Nature*, vol. 469, pp. 381–384, 2011. DOI: 10.1038/nature09713.

[51] N. Kern and D. Frenkel, "Fluid–fluid coexistence in colloidal systems with short-ranged strongly directional attraction," *J.Chem. Phys.*, vol. 118, pp. 9882–9889, 2003. DOI: 10.1063/1.1569473.

[52] F. Romano and F. Sciortino, "Two dimensional assembly of triblock Janus particles into crystal phases in the two bond per patch limit," *Soft Matter*, vol. 7, p. 5799, 2011. DOI: 10.1039/c0sm01494j.

[53] A. Giacometti, F. Romano, and F. Sciortino, "Theoretical calculations of phase diagrams and self-assembly in patchy colloids," *arXiv preprint*, 2012.

[54] J. C. Maxwell, "On the calculation of the equilibrium and stiffness of frames," *Lond. Edinb. Dubl. Phil. Mag.*, vol. 27, pp. 294–299, 1864. DOI: 10.1080/14786446408643668.

[55] X. Mao, Q. Chen, and S. Granick, "Entropy favours open colloidal lattices," *Nat. Mater.*, vol. 12, pp. 217–222, 2013. DOI: 10.1038/nmat3496.

[56] M. E. Cates, "Patchy colloids: Entropy stabilizes open crystals," *Nat. Mater.*, vol. 12, pp. 179–180, 2013. DOI: 10.1038/nmat3573.

[57] X. Mao, "Entropic effects in the self-assembly of open lattices from patchy particles," *Phys. Rev. E*, vol. 8732, p. 062 319, 2013. DOI: 10.1103/PhysRevE.87.062319.

[58] D. Z. Rocklin and X. Mao, "Self-assembly of three-dimensional open structures using patchy colloidal particles," *Soft Matter*, vol. 10, pp. 7569–7576, 2014. DOI: 10.1039/C4SM00587B.

[59] W. F. Reinhart and A. Z. Panagiotopoulos, "Equilibrium crystal phases of triblock Janus colloids," *J. Chem. Phys.*, vol. 145, 2016. DOI: 10.1063/1.4961869.

[60] T. T. Ngo, C. M. Liddell, M. Ghebrebrhan, and J. D. Joannopoulos, "Tetrastack: Colloidal diamond-inspired structure with omnidirectional photonic band gap for low refractive index contrast," *Appl. Phys. Lett.*, vol. 88, p. 241 920, 2006. DOI: 10.1063/1.2206111.

[61] A. J. Garcia-Adeva, "Band gap atlas for photonic crystals having the symmetry of the kagome and pyrochlore lattices," *New J. Phys.*, vol. 8, p. 86, 2006. DOI: 10.1088/1367-2630/8/6/086.

[62] ——, "Band structure of photonic crystals with the symmetry of a pyrochlore lattice," *Phys. Rev. B*, vol. 73, p. 073 107, 2006. DOI: 10.1103/PhysRevB.73.073107.

[63] H. Pattabhiraman, G. Avvisati, and M. Dijkstra, "Novel pyrochlorelike crystal with a photonic band gap self-assembled using colloids with a simple interaction potential," *Phys. Rev. Lett.*, vol. 119, p. 157 401, 2017. DOI: 10.1103/PhysRevLett.119.157401.

[64] F. Romano and F. Sciortino, "Patterning symmetry in the rational design of colloidal crystals," *Nat. Commun.*, vol. 3, pp. 975–976, 2012. DOI: 10.1038/ncomms1968.

[65] N. A. Mahynski, L. Rovigatti, C. N. Likos, and A. Z. Panagiotopoulos, "Bottom-Up Colloidal Crystal Assembly with a Twist," *ACS Nano*, vol. 10, pp. 5459–5467, 2016. DOI: 10.1021/acsnano.6b01854.

[66] D. Morphew, J. Shaw, C. Avins, and D. Chakrabarti, "Programming Hierarchical Self-Assembly of Patchy Particles into Colloidal Crystals via Colloidal Molecules," *ACS Nano*, pp. 2355–2364, 2018. DOI: 10.1021/acsnano.7b07633.

[67] Q. Chen, S. C. Bae, and S. Granick, "Staged self-assembly of colloidal metastructures," *JACS*, vol. 134, pp. 11 080–11 083, 2012. DOI: 10.1021/ja303434d.

[68] S. N. Fejer and D. J. Wales, "Design of a Kagome lattice from soft anisotropic particles," *Soft Matter*, vol. 11, pp. 6663–6668, 2015. DOI: 10.1039/C5SM01191D.

[69] K. Chaudhary, Q. Chen, J. J. Juárez, S. Granick, and J. A. Lewis, "Janus Colloidal Matchsticks," *J. Am. Chem. Soc.*, vol. 134, pp. 12 901–12 903, 2012. DOI: 10.1021/ja305067g.

[70] C.-Y. Zhang, X.-L. Jian, and W. Lu, "Structure and percolation of one-patch spherocylinders," *Soft Matter*, vol. 11, pp. 1362–1368, 2015. DOI: 10.1039/C4SM02402H.

[71] C. T. Chan, K. M. Ho, and C. M. Soukoulis, "Photonic band gaps in experimentally realizable periodic dielectric structures," *EPL*, vol. 16, p. 563, 1991. DOI: 10.1209/0295-5075/16/6/009.

[72] C. Kittel, *Introduction to Solid State Physics*, 7th. New York: John Wiley & Sons, Inc., 1996.

[73] N. W. Ashcroft and N. D. Mermin, *Solid State Physics*. Philadelphia: Saunders College, 1976.

[74] K. D. Gibson and H. A. Scheraga, "Crystal packing without symmetry constraints. 1. tests of a new algorithm for determining crystal structures by energy minimization," *J. Phys. Chem.*, vol. 99, pp. 3752–3764, 1995. DOI: 10.1021/j100011a051.

[75] Libretexts, *General Chemistry (Petrucci et. al.)* Libretexts, Dec. 2015, ch. 12.6. [Online]. Available: https://chem.libretexts.org/Bookshelves/General_Chemistry.

[76] M. Goano, F. Bertazzi, M. Penna, and E. Bellotti, "Electronic structure of wurtzite zno: Nonlocal pseudopotential and ab initio calculations," *J. Appl. Phys*, vol. 102, p. 083 709, 2007. DOI: 10.1063/1.2794380.

[77] P. Y. Yu and M. Cardona, *Fundamentals of Semiconductors: Physics and Materials Properties*. Berlin: Springer, 2005, ISBN: 3540254706.

[78] S. L. Price, "The computational prediction of pharmaceutical crystal structures and polymorphism," *Adv. Drug Deliv. Rev.*, vol. 56, pp. 301–319, 2004, Pharmaceutical solid polymorphism in drug development and regulation. DOI: 10.1016/j.addr.2003.10.006.

[79] D. J. Wales, "Decoding the energy landscape: extracting structure, dynamics and thermodynamics.," vol. 370, pp. 2877–2899, 2012. DOI: 10.1098/rsta.2011.0208.

[80] J. de Graaf, L. Filion, M. Marechal, R. van Roij, and M. Dijkstra, "Crystal-structure prediction via the floppy-box monte carlo algorithm: Method and application to hard (non)convex particles," *J. Chem. Phys*, vol. 137, p. 214 101, 2012. DOI: 10.1063/1.4767529.

[81] D. Chakrabarti and D. J. Wales, "Simulations of rigid bodies in an angle-axis framework," *Phys. Chem. Chem. Phys.*, vol. 11, no. 12, pp. 1970–1976, 2009.

[82] J. B. Kuipers, *Quaternions and rotation sequences : a primer with applications to orbits, aerospace, and virtual reality*. Princeton University Press, 1999. [Online]. Available: https://press.princeton.edu/titles/6429.html.

[83] J. Voight, "The arithmetic of quaternion algebras," *preprint*, 2014.

[84] W. R. Hamilton, *Elements of quaternions*. Longmans, Green, & Company, 1866.

[85] W. W. Hager and H. Zhang, "A survey of nonlinear conjugate gradient methods," *Pac. J. Optim*, vol. 2, pp. 35–58, 2006.

[86] J. Nocedal and S. J. Wright, *Numerical optimization*. Springer, 2006.

[87] D. Wales, *Energy landscapes: Applications to clusters, biomolecules and glasses*. Cambridge University Press, 2003.

[88] D. J. Wales and J. P. K. Doye, "Global Optimization by Basin-Hopping and the Lowest Energy Structures of Lennard-Jones Clusters Containing up to 110 Atoms," 1997. DOI: 10.1021/JP970984N.

[89] S. G. Johnson and J. D. Joannopoulos, "Block-iterative frequency-domain methods for maxwell's equations in a planewave basis," *Opt. Express*, vol. 8, pp. 173–190, 2001. DOI: 10.1364/OE.8.000173.

[90] ——, *Introduction to photonic crystals: Bloch's theorem, band diagrams, and gaps (but no defects)*, Feb. 2003. [Online]. Available: http://ab-initio.mit.edu/photons/tutorial/photonic-intro.pdf.

[91] E. N. Economou, *The Physics of Solids: Essentials and Beyond*. Springer Science & Business Media, 2010.

[92] G. Mie, "Articles on the optical characteristics of turbid tubes, especially colloidal metal solutions," *Ann. Phys.*, vol. 25, pp. 377–445, 1908.

[93] C. Bohren and D. R. Huffman, *Absorption and Scattering of Light by Small Particles*. Wiley Science Paperback Series, 1998.

[94] A. I. Kuznetsov, A. E. Miroshnichenko, M. L. Brongersma, Y. S. Kivshar, and B. Luk'yanchuk, "Optically resonant dielectric nanostructures," *Science*, vol. 354, aag2472, 2016.

[95] K. Inoue and K. Ohtaka, *Photonic crystals: physics, fabrication and applications*. Springer Science & Business Media, 2004, vol. 94.

[96] E. Lidorikis, M. M. Sigalas, E. N. Economou, and C. M. Soukoulis, "Tight-binding parametrization for photonic band gap materials," *Phys. Rev. Lett.*, vol. 81, pp. 1405–1408, 1998. DOI: 10.1103/PhysRevLett.81.1405.

[97] R.-L. Chern and S. D. Chao, "Optimal higher-lying band gaps for photonic crystals with large dielectric contrast," *Opt. Express*, vol. 16, pp. 16 600–16 608, 2008. DOI: 10.1364/OE.16.016600.

[98] C. Vandenbem and J. P. Vigneron, "Mie resonances of dielectric spheres in face-centered cubic photonic crystals," *J. Opt. Soc. Am. A*, vol. 22, pp. 1042–1047, 2005. DOI: 10.1364/JOSAA.22.001042.

[99] L. Shi, X. Jiang, and C. Li, "Effects induced by mie resonance in two-dimensional photonic crystals," *J. Phys. Condens. Matter*, vol. 19, p. 176 214, 2007. DOI: 10.1088/0953-8984/19/17/176214.

[100] C. M. Soukoulis, *Photonic band gaps and localization*. Springer Science & Business Media, 2013, vol. 308.

[101] M. Florescu, S. Torquato, and P. J. Steinhardt, "Complete band gaps in two-dimensional photonic quasicrystals," *Phys. Rev. B*, vol. 80, p. 155 112, 2009. DOI: 10.1103/PhysRevB.80.155112.

[102] S. John and J. Wang, "Quantum optics of localized light in a photonic band gap," *Physical Review B*, vol. 43, p. 12 772, 1991.

[103] T. K. Amoah, "Designer disordered complex media: Hyperuniform photonic and phononic band gap materials," PhD thesis, University of Surrey, 2016. [Online]. Available: http://epubs.surrey.ac.uk/812500/.

[104] R. D. Meade, A. M. Rappe, K. D. Brommer, and J. D. Joannopoulos, "Nature of the photonic band gap: Some insights from a field analysis," *J. Opt. Soc. Am. B*, vol. 10, pp. 328–332, 1993. DOI: 10.1364/JOSAB.10.000328.

[105] A. Cuetos, B. Martínez-Haya, L. F. Rull, and S. Lago, "Monte Carlo study of liquid crystal phases of hard and soft spherocylinders," *J. Chem. Phys*, vol. 117, pp. 2934–2946, 2002. DOI: 10.1063/1.1491872.

[106] A. Cuetos and B. Martínez-Haya, "Liquid crystal phase diagram of soft repulsive rods and its mapping on the hard repulsive reference fluid," *Mol. Phys.*, vol. 113, pp. 1137–1144, 2015. DOI: 10.1080/00268976.2014.996191.

[107] D. J. Earl, J. Ilnytskyi, and M. R. Wilson, "Computer simulations of soft repulsive spherocylinders," *Mol. Phys.*, vol. 99, pp. 1719–1726, 2001. DOI: 10.1080/002689701.

[108] C. Vega and S. Lago, "A fast algorithm to evaluate the shortest distance between rods," *Computers & Chemistry*, vol. 18, pp. 55–59, 1994. DOI: 10.1016/0097-8485(94)80023-5.

[109] J. W. R. Morgan, D. Chakrabarti, N. Dorsaz, and D. J. Wales, "Designing a bernal spiral from patchy colloids," *ACS Nano*, vol. 7, pp. 1246–1256, 2013. DOI: 10.1021/nn304677t. [Online]. Available: www.acsnano.org.

[110] J. H. Conway and S. Torquato, "Packing, tiling, and covering with tetrahedra," *Proc. Natl. Acad. Sci. U.S.A.*, vol. 103, pp. 10 612–10 617, 2006. DOI: 10.1073/pnas.0601389103.

[111] A. Togo and I. Tanaka, "`Spglib`: a software library for crystal symmetry search," *ArXiv e-prints*, 2018. arXiv: 1808.01590.

[112] W. Setyawan and S. Curtarolo, "High-throughput electronic band structure calculations: Challenges and tools," *Comput. Mater. Sci.*, vol. 49, pp. 299–312, 2010. DOI: 10.1016/j.commatsci.2010.05.010.

[113] M. Maldovan, W. C. Carter, and E. L. Thomas, "Three-dimensional dielectric network structures with large photonic band gaps," *Appl. Phys. Lett.*, vol. 83, pp. 5172–5174, 2003. DOI: 10.1063/1.1635664.

[114] I. D. Hosein, M. Ghebrebrhan, J. D. Joannopoulos, and C. M. Liddell, "Dimer shape anisotropy: A nonspherical colloidal approach to omnidirectonal photonic band gaps," *Langmuir*, vol. 26, pp. 2151–2159, 2010. DOI: 10.1021/la902609s.

[115] M. S. Dresselhaus, G. Dresselhaus, and A. Jorio, *Group theory: application to the physics of condensed matter*. Springer-Verlag, 2010.

[116] A. De and C. E. Pryor, "Electronic structure and optical properties of Si, Ge and diamond in the lonsdaleite phase," *J. Phys. Condens. Matter*, vol. 26, p. 045 801, 2014. DOI: 10.1088/0953-8984/26/4/045801.

[117] K. Edagawa, "Photonic crystals, amorphous materials, and quasicrystals," *Sci. Technol. Adv. Mater.*, vol. 15, p. 034 805, 2014. DOI: 10.1088/1468-6996/15/3/034805.

[118] D. Morphew and D. Chakrabarti, "Programming hierarchical self-assembly of colloids: Matching stability and accessibility," *Nanoscale*, vol. 10, pp. 13 875–13 882, 2018. DOI: 10.1039/C7NR09258J.

[119] S. Whitelam and P. L. Geissler, "Avoiding unphysical kinetic traps in monte carlo simulations of strongly attractive particles," *J. Chem. Phys*, vol. 127, p. 154 101, 2007. DOI: 10.1063/1.2790421.

[120] Š. Růžička and M. P. Allen, "Collective translational and rotational monte carlo moves for attractive particles," *Phys. Rev. E*, vol. 89, p. 033 307, 2014. DOI: 10.1103/PhysRevE.89.033307.

[121] E. Maras, O. Trushin, A. Stukowski, T. Ala-Nissila, and H. Jónsson, "Global transition path search for dislocation formation in ge on si(001)," *Comput. Phys. Commun.*, vol. 205, pp. 13–21, 2016. DOI: 10.1016/j.cpc.2016.04.001.

[122] A. Stukowski, "Visualization and analysis of atomistic simulation data with ovito - the open visualization tool," *Model. Simul. Mater. Sci. Eng.*, vol. 18, p. 015 012, 2010. [Online]. Available: http://stacks.iop.org/0965-0393/18/i=1/a=015012.

[123] W. Park, "Optical interactions in plasmonic nanostructures," *Nano Converg.*, vol. 1, 2014. DOI: 10.1186/s40580-014-0002-x.

[124] E. Prodan, C. Radloff, N. J. Halas, and P. Nordlander, "A hybridization model for the plasmon response of complex nanostructures," *Science*, vol. 302, pp. 419–422, 2003. DOI: 10.1126/science.1089171.

[125] Y. Chen, L. Xu, G. Cai, and H. Chen, "Chemical bonds and edge states in a metamolecular crystal," *Phys. Rev. B*, vol. 98, p. 125 430, 2018. DOI: 10.1103/PhysRevB.98.125430.

[126] B. R. A. Nijboer and F. W. De Wette, "On the calculation of lattice sums," *Physica*, vol. 23, pp. 309–321, 1957. DOI: 10.1016/S0031-8914(57)92124-9.

[127] C. M. Fortuin, "Note on the calculation of electrostatic lattice potentials," *Physica*, vol. 86, pp. 574–586, 1977. DOI: 10.1016/0378-4371(77)90095-4.

[128] D. E. Williams, "Accelerated convergence of crystal-lattice potential sums," *Acta Crystallogr. A*, vol. 27, pp. 452–455, 1971. DOI: 10.1107/S0567739471000998.

[129] B. A. Wells and A. L. Chaffee, "Ewald summation for molecular simulations," *J. Chem. Theory Comput.*, vol. 11, pp. 3684–3695, 2015. DOI: 10.1021/acs.jctc.5b00093.

[130] D. E. Williams and T. L. Starr, "Calculation of the crystal structures of hydrocarbons by molecular packing analysis," *Computers & Chemistry*, vol. 1, pp. 173–177, 1977. DOI: 10.1016/0097-8485(77)85007-9.

[131] B. P. van Eijck, A. L. Spek, W. T. M. Mooij, and J. Kroon, "Hypothetical Crystal Structures of Benzene at 0 and 30 kbar," *Acta Crystallogr. B*, vol. 54, pp. 291–299, 1998. DOI: 10.1107/S0108768197013384.

[132] C. R. A. Catlow, *Computer modeling in inorganic crystallography*. Elsevier, 1997.

[133] S. John and K. Busch, "Photonic bandgap formation and tunability in certain self-organizing systems," *J. Light. Technol.*, vol. 17, pp. 1931–1943, 1999. DOI: 10.1109/50.802976.

[134] F. H. Stillinger, "Lattice sums and their phase diagram implications for the classical lennard-jones model," *J. Chem. Phys*, vol. 115, pp. 5208–5212, 2001. DOI: 10.1063/1.1394922.